Study of an integrated on-chip interferometer. Application for the characterization of innovative transducers.

Walid Adel Merzouk

NNT : 2019SACLV014

Thèse de doctorat

Study of an integrated on-chip interferometer. Application for the characterization of innovative transducers

Thèse de doctorat de l'Université Paris-Saclay
préparée à l 'UVSQ

École doctorale n°580 STIC
Spécialité de doctorat : Optoélectronique

Thèse présentée et soutenue à Vélizy, le 25 janvier 2019, par

M. Walid Adel MERZOUK

Composition du Jury :

M. Jorge LINARES Professeur, UVSQ (GEMaC)	Président
M. Patrick JUNCAR Professeur, CNAM (LCM)	Rapporteur
M. Ju-Yi LEE Professeur, NCU (Taïwan)	Rapporteur
Mme Aude BOLOPION Chargée de recherche, CNRS (FEMTO-ST)	Examinatrice
M. Barthélemy CAGNEAU Maître de Conférences / HDR, UVSQ (LISV)	Co-encadrant de thèse
M. Luc CHASSAGNE Professeur, UVSQ (LISV)	Directeur de thèse

Université Paris-Saclay
Espace Technologique / Immeuble Discovery
Route de l'Orme aux Merisiers RD 128 / 91190 Saint-Aubin, France

Contents

Introduction

Following the introduction of nanoscience in 1959 by the Nobel price laureate Richard P. Feynman, many inventions and discoveries in the fabrication, characterization and analysis of nanoscale objects and structures have emerged. The developments in nanotechnologies led to the birth of new research fields, technologies and technical applications. Nowadays, nanotechnology has already begun to appear in various applications and products to enhance the functionalities and performances of instruments and devices for electronics, magnetics, optoelectronics, biomedical, pharmaceutical, cosmetics, energy, catalytics, telecommunications, optics, mechanics, chemistry, biology, health, environment, transport and material applications.

The emergence of nanoscience and nanotechnology is linked to the need for better accuracy and precision. Applications dedicated to nanoscales can relate to the manipulation of nano-objects and structures or the positioning at the nanometer scale of tools and samples. For instance, the conception and assembly of nanoscaled devices and systems require precise techniques for positioning, sensing and assembly with nanometer resolutions. One of the key elements to success in those nanotechnology processes are the sensing systems.

In recent years, positioning systems with enhanced accuracy, precision, stroke, velocity were developed. Those systems associate a stage capable of high performances with a high resolution sensor. Most of them rely on interferometric devices, especially if both high resolution and stroke is a concern. Moreover, interferometers allow accuracy and traceability for displacement measurements. However, they usually suffer of a non-negligible sensitivity to the medium index.

For micro/nanomanipulation, it is often based on micro-grippers, that enable flexible maneuvering and precise positioning of nanostructures of different natures, extending from bio-medicinal cells to Micro-Electro-Mechanical Systems (MEMS). Alike nanopositioning systems, micromanipulators also require a sensing system feedback of the targeted micro-object position and/or the tool status. Nowadays, microgrippers are often based on piezoelectric, NEMS/MEMS or polymers. They can include capacitive, optical

encoders, strain gauges and NEMS/MEMS or polymer based position sensors.

The LISV has been working on the design and development of a sub-nanometric resolution, compact and easy-to-use interferometer. This work was made possible with the collaboration between the LISV and our industrial partner Teemphotonics. This PhD work aims at the investigation of the characteristics, particularities and potential of an interferometer with a fully embedded optical chip. The interferometer is compact and highly integrable. It demonstrates that low sensitivity to external disturbances and ease of use can be achieved. It exhibits high stability, robustness against parasite rotations and picometric performances. This interferometer is used to characterize a bending electro-active transducer made with polymers and capable to be in actuator or sensor mode. The capabilities of this transducer for micrometric displacements are investigated. This material is provided by our partner Physicochemistry of Polymers and Interfaces Laboratory (LPPI, University of Cergy Pontoise) through the project MicroTIP (ANR 2015, generic call). The main advantage of this polymer, compared to piezoelectrics cells, is its low voltage actuation ($< 2\,V$) for high bending performances. Moreover, it is flexible, low weight and exhibits high power to mass ratio. This makes it very suitable for artificial muscle emulation and micro grippers conception.

In this manuscript, chapter one introduces some of the existing nanometrological instruments and the improvement realized in metrological microscopy through positioning systems and sensors. Different solutions for position sensing are listed with a focus about metrological aspects of the interferometric system. Finally, conducting ionic electro-active trilayers polymer functioning principle and structure is recalled. The realized advancements in this polymer synthesis and performances is discussed.

Chapter two presents the studied interferometer architecture, functioning principle and performances. The aim of this chapter is mainly to evaluate the interferometer in quasi-static conditions or with very small displacements in order to analyze the noise level at high acquisition frequency and estimate the long term performances. Dynamic measurements are also presented to demonstrate the subnanometric capabilities of the sensor.

Chapter three deals with the metrological interferometric measurement specificities and sources of errors. The system maximum displacement velocity is demonstrated and its compensation using a parallel coarse position sensing system is highlighted. Moreover, the sensor robustness to temperature and humidity variations, under controlled environment is investigated and discussed.

Chapter four is dedicated to the study of a Ionical Electro-Active Polymer (IEAP) in cantilevered beam configuration. In order to evaluate the performances with the

interferometer, a model of electro-active polymer based on bibliography is proposed. Experimental results are provided to measure the stiffness and the first fundamental frequency of the material. A transfer function is identified to model the system behavior in sensor mode. Moreover, the micrometric capabilities of the IEAP are demonstrated in both actuating and sensing modes using experimental setups based on the previously presented interferometer. Moreover, the robustness of the interferometer against power fluctuation is highlighted while actuating the polymer.

Finally, a conclusion highlights the main results of this thesis and proposes some enhancements for the next future.

Chapter 1

Focus on specific nanopositioning systems

Contents

1.1 Introduction

Nowadays, micro/nanomaterials and metrologic instruments appear in several industrial applications and research fields. Advances in micro/nanoscience are driven by the improvements in two essential sub-fields. The first one concerns nanometrology and the study, characterization and analysis of very small specimens. The second one is the micro/nanorobotics for the interaction with very small components or the integration/-conception of micro/nanostructures. Since a few decades, a high number of nanopositioning systems and position sensors have been developed with success. They are often developed to provide users with better accuracy, resolution, higher stroke length, velocity and bandwidth. And the same goes, for micro/nanorobotics manipulator and grippers based on micro/nanostructures or piezoelectrics and polymers.

The fields of nanotechnology are too numerous, this first chapter is only focusing on specific aspects of the nano world with the applications that concern microscopy. This chapter introduces the existing nanometrologic instruments and the improvement realized in metrologic microscopy through positioning systems and sensors. We briefly discuss the different solutions for position sensing and introduce the metrology based on interferometers as well as its specificity. Since we are interested in experiments with conducting ionic electro-active trilayer polymer, this chapter provides the reader with some background about them.

1.2 Metrologic instruments at nanoscale

The nanotechnology was first introduced by the Nobel price laureate Richard P. Feynman in 1959 [1]. It was the first time that a technological vision of extreme miniaturization was presented. Based on this observation, researchers and industrials have worked on the birth of several research fields related to the nanoscale. Nowadays, nanotechnology extends from micro/nanofabrication and nanostructures synthesis to bionanomechanics and bionanotribology, and it encompasses nanometrology, and MEMS/NEMS or bioMEMS/NEMS conceptions and integration. For example, we choose to focus in this chapter on the microscopy world.

1.2.1 Scanning Probe Microscopy (SPM)

Nanoscale science and technology is strongly driven by nanometrology, which is a sub-field of metrology. Nanometrology refers to the study of the dimensions, position, orientation, topography and shape of samples at this scale. One of the most powerful

tool for surface imaging is the Scanning Tunneling Microscope (STM) developed by Gerd Binning *et al.* in 1981 [2]. It was the first 3D solid surface with very high resolution for imaging. Binning and Rohrer received a Nobel prize in 1986 for this instrument. In 1985, Binning *et al.* developed an Atomic Force Microscope (AFM) for submicrometric force measurement [3]. AFMs and STMs have in common that the measurements are performed with a sharp probe, scanning over the surface while maintaining a very close spacing to the latter. The AFM is basically composed of:

- a scanning system: the scanner can move the sample (with a translation stage) or the probe (fixed sample holder) depending on its design and application.
- a probe: it is composed of a very sharp tip integrated into the end of a cantilever.
- a motion sensor: it senses the strain between the probe and the sample. Its most common design is an optical beam deflection. A laser beam is reflected by the cantilever onto a segmented photodiode to measure the probe deformation as illustrated in fig.1.1.

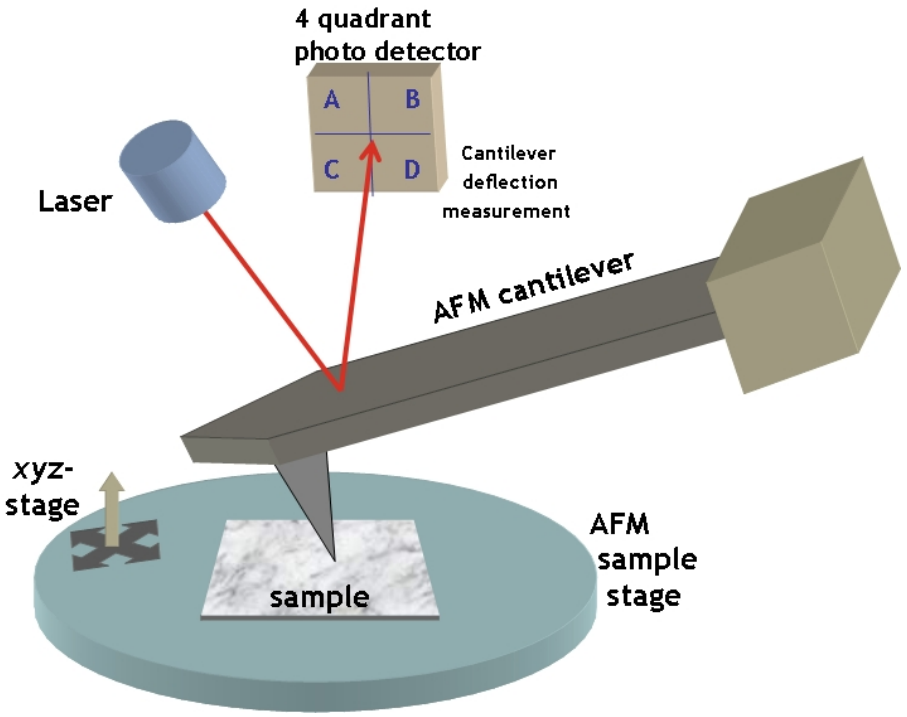

Figure 1.1 Atomic Force Microscope setup.

The design of a STM is similar to the one of AFM. Its working principle is based on quantum tunneling of electrons between the surface and the STM tip. Unlike AFM, where no limitation is imposed, the STM tip and the sample surface must be conducting.

As the tip is moved across the surface, a bias voltage is applied between the tip and the surface. It causes electrons to tunnel through the vacuum from the surface to the tip with a tunneling current effect. Changes in the surface height or density are thus measured with respect to the tunneling current.

This instrument, based on the use of a probe, refers in the literature as a Scanning Probe Microscope (SPM). The development of the technologies at nanoscale was strongly influenced by the improvement of the SPM techniques. Nowadays, the SPM is used in the analysis and study of several kind of samples [4, 5, 6, 7, 8, 9, 10] like electronics and magnetics surfaces or even biological and chemical ones [11].

The SPM family consists of several instruments based on STMs and AFMs. It includes: the lateral force microscopy (LFM) [12], the scanning electrostatic force microscopy (SEFM) [13], scanning force acoustic microscopy (SFAM) [14], scanning magnetic microscopy (SMM) [15], scanning near field optical microscopy (SNOM) [16, 17], scanning thermal microscopy (SThM) [18], scanning electrochemical microscopy (SEcM) [19], scanning Kelvin Probe microscopy (SKPM) [20], scanning chemical potential microscopy (SCPM) [21], scanning ion conductance microscopy (SICM) [22] and scanning capacitance microscopy (SCM) [23].

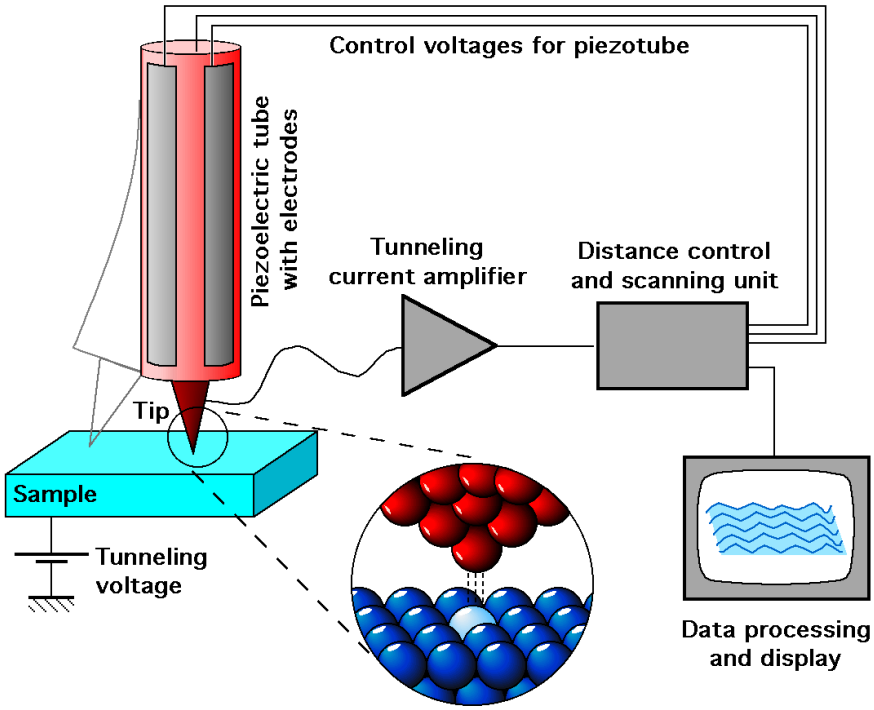

Figure 1.2 Scanning Tunneling Microscope schematic [24].

1.2.2 Electron Microscopy

Another family of nanometrologic instruments is the electron microscopy that includes the Scanning Electron Microscope (SEM) [25, 26, 27] and Transmission Electron Microscope (TEM) [28, 29, 30]. Electron microscopy (EM) has been a revolutionary imaging technology for scientists and engineers far before SPMs emergence. EM generate highly focused beam of electrons which impact the sample inside a vacuum chamber. They generate an emission of signals from the sample. These signals can be detected and used to form a structural and chemical image of the sample realizing both nanoscale imaging and spectroscopy [31].

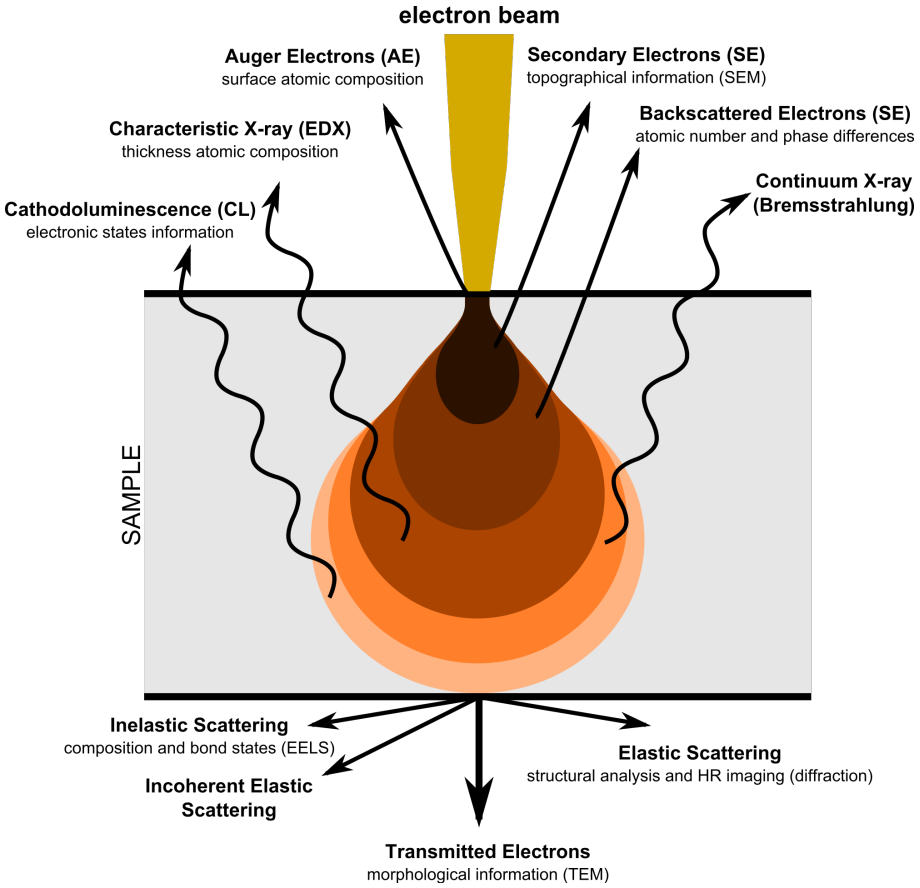

Figure 1.3 Electron Microscope (Electron interaction with matter) [32].

An EM provides fast imaging with nanometer resolution. This enables the development of solutions based on robotics for nanomanipulation systems inside the vacuum chamber. Both imaging and direct interactions with nanoscaled samples can be performed [33, 34, 35]. In fact, nanometrology and micro/nanorobotics have always been closely correlated in several systems and applications. For example with piezoelectric active AFM probes in tapping mode [36], or nanomanipulation of nanoscaled devices for precise positioning of nanostructures for nanodevice assembly [37], like NEMs/MEMs

systems conception/integration. Nowadays, micro/nanorobotics is extended from the micropositioning and interaction with biological and chemical specimens to automated devices microassembly. They can even be used in robotized surgery [38].

1.3 Nanopositioning systems

Nanometrologic instruments are usually built around a nanopositioning system. It is even not exaggerated to say that the nanopositioning systems are the hearts of conventional scanning probe microscopes. The need for high precision positioning systems is in still development because of required stroke length to achieve, for example, larger surfaces characterization in SPMs. Moreover, long stroke and accurate positioning systems are also required for applications like lithography, wafers and mask printing, new material positioning and analysis, the manipulation and the assembly of micro/nanostructures [39]. All those characterizations and design techniques highly depend on the precision and stroke. Moreover, the development of these applications is based on the improvement of the positioning systems performances and specifications.

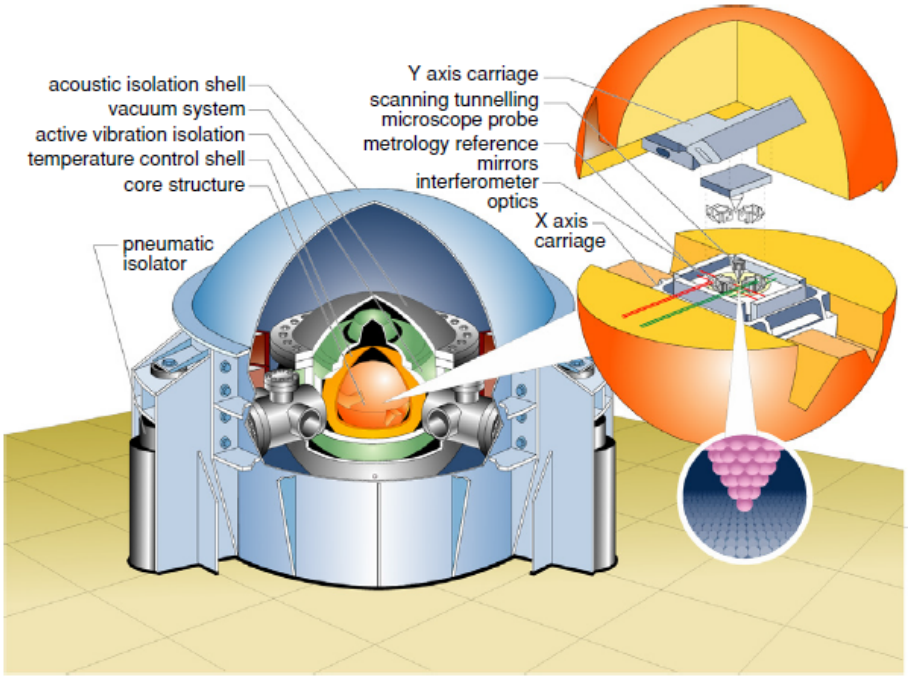

Figure 1.4 Cut-away view of the Molecular Measuring Machine [40].

With the need for the characterization and the analysis of larger micro/nanostructures, multiple long stroke with high resolution positioning systems were developed [10]. A first example is the Molecular Measuring Machine (M^3) developed by the National

Institute of Standards and Technology (NIST). It was developed to perform measurements with 1 nanometer of standard deviation. The positions of patterns located on a surface of 50 mmx50 mm. The M^3 is designed for SEM applications and works in high-vacuum environment. It includes sub-nanometric resolution scanning probes, nanometric accuracy interferometers, nanometric linear actuators, mechanical and acoustic noise isolation and thermal stabilization. This machine has a double translation stages configuration, combining a long stroke coarse stage with high resolution fine stage [40].

Another example is the High-Precision Micro-Coordinating Measuring Machine (CMM) developed by the University of Tokyo and the National Institute of Advanced Industrial Science and Technology (AIST). It achieves 50 nm measurement uncertainty within a moving volume of 160 mmx160 mmx100 mm [41]. The ultra-precision CMM Isara 400 (IBS Precision Engineering) that achieve 11 nm measurement uncertainty within a moving volume of 160 mmx160 mmx100 mm [41]. The small-sized CMM developed by the National Physical Laboratory (NPL), this instrument has a working volume of 50x50x50 mm^3 and an uncertainty in the range of $50-150\,nm$ [42]. The Abbe Error Free Micro CMM developed by the School of Instrument Science and Opto-electric Engineering of Hefei University of Technology, which measurement volume is of 50x50x50 mm^3 for measuring accuracy of about 100 nm [43]. The TriNano ultra precision CMM from Xpress Precision Engineering; the machine is able to reach uncertainties below 100 nm over its measurement range of 64 cubic centimeters [44].

1.3.1 Micro-CMM of METAS

In 2007, the micro-CMM was developed by the Swiss Federal Office of Metrology (METAS). It was a great success due to its innovative design of the touch probe. This is based on a parallel kinematic structure of flexure hinges to ensure an isotropic low stiffness. Moreover, this head features very weak probing forces to prevent any potential deterioration of the studied sample [45].

The METAS micro-CMM includes an air bearing stage with interferometric position measurement with no Abbe offset and achieves a repeatability of about 5 nm over a 90 mmx90 mmx38 mm moving volume. The accuracy is less than 80 nm. Moreover, its user interface integrates all measurement and scanning techniques making it a flexible and accurate instrument for microtechnology research and industry.

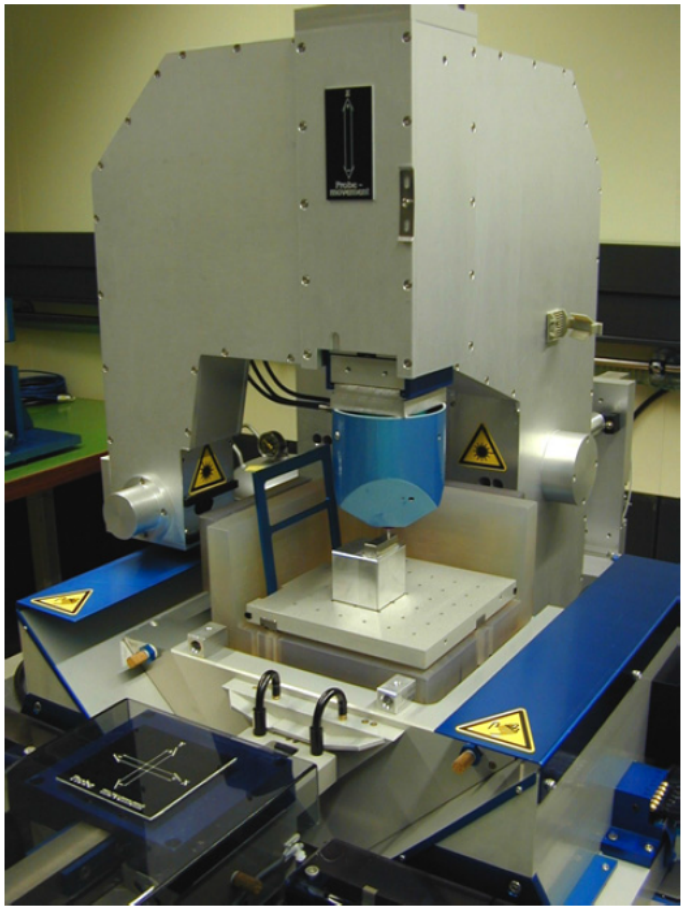

Figure 1.5 The micro-CMM of METAS [45].

1.3.2 Nanopositioning and nanomesuring machine (NNM)

The nanopositioning and nanomesuring machine (NNM), developed by the German company SIOS, is one of the most well-known precision positioning machines. This machine was developed by the Institute of Process Measurement and Sensor Technology from Ilmenau University of Technology in Germany in 2001 [46]. Recently, the NNM has been upgraded regarding its mirror corner, interferometers and angle sensors. Researchers also improved its weight compensation, its electronic controller, its vibration damping stage and its instrument chamber [47]. This upgraded version can reach a dynamic range of $200\,mm$x$200\,mm$x$25\,mm$ for $25\,mm$x$25\,mm$x$5\,mm$ previously. The resolution of each interferometer has been improved from $0.1\,nm$ to $0.02\,nm$.

The machine represents the great improvement of the extended three dimensional Abbe comparator principle to achieve nanometer accuracy. The NNM was designed for metrologic purposes and more specifically to eliminate any Abbe error. This is done by minimizing the distance between the point of intersection of the measurement axis of the combined interferometers and the measurement point to be made. Laser interferometers

are used to measure the target displacements. Additionally, to reduce the first-order deviations (despite remaining Abbe offsets), the angular deviations around the X, Y and Z axes are measured using laser interferometry. They are then controlled using voice coil rotation actuators.

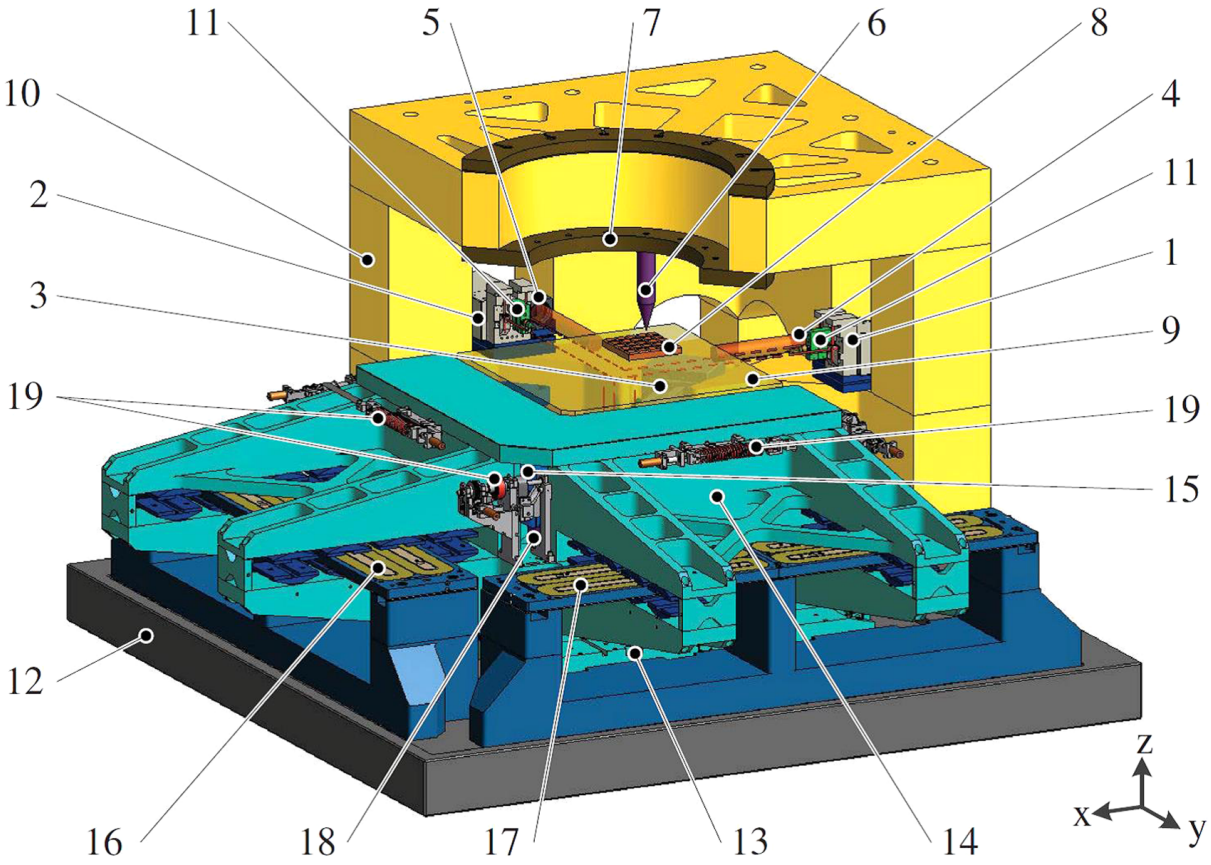

Figure 1.6 Mechanical and optical basic structure of NPMM-200: 1. x-, 2. y- and 3. z-interferometer, 4. pitch and yaw angle sensor (jy and jz), 5. roll and yaw angle sensor (jx and jz), 6. probe system (fixed in space), 7. mounting points for the probe system, 8. measuring object, 9. mirror plate, 10. metrology frame, 11. reference sensors, 12. base plate, guides system of the 13. x-, 14. y-, and 15. z-axis, drive systems of the 16. x-, 17. y-, and 18. z-axis, and 19. weight force compensation [48].

The stability as well as the repeatability for positioning is less than $2\,nm$ over the whole measuring range of the NNM . The NNM is used to position, measure, scan, process and manipulate objects with nanometric accuracy and on spatially extensive surfaces, due to its ease of integration into a wide variety of systems and applications.

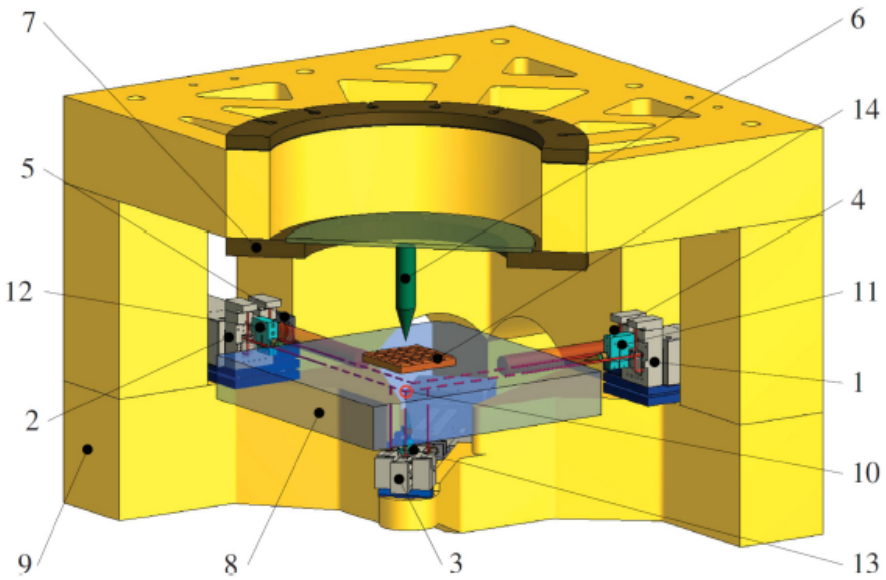

Figure 1.7 Metrological concept of the NPMM-200: 1. interferometer x-axis, 2. interferometer y-axis, 3. interferometer z-axis, 4. angle sensor jy and jz, 5. angle sensor jx and jz, 6. probe system with vertical Abbe offset (fixed in space), 7. mounting points for the probe system, 8. mirror plate, 9. metrology frame, 10. Abbe point, 11. reference sensor x-axis, 12. reference sensor y-axis, 13. reference sensor z-axis, and 14. measurement object [48].

1.4 Nanoscale position sensors

Every high positioning system requires sensors with high resolution. Position sensors with nanometer resolution are a key component of many precision imaging and fabrication machines. The development of sensors dedicated to nanotechnology is a full topic since several years and is still challenging. Sensing systems can still be the key elements to success in a nanotechnology process.

1.4.1 Performances of usual nanoposition sensors

Several sensors with different technologies allow for sub-nanometric performances. Strain sensors, piezoelectric sensors, capacitive sensors, inductive sensors, encoders and interferometers are the most common examples.

Position sensors based on deformations

The resistive strain gauge is the most common position sensor. It has the advantage to be compact, low-cost, precise and highly stable. The resistive strain gauge can

be integrated or bonded to the translating surface and is widely used in the position control loop of the piezoelectric actuators [49]. However, resistive strain gauge are not competitive for nanoscale applications. The Omega SGD-3/350-LY13 gauges exhibit, for instance, a poor $23\,nm$ resolution for a $100\,\mu m$ full scale range and a $5\,V$ bridge excitation [50]. This is far from competitive in both resolution and measurement range.

Alike resistive gauge, the piezoresistive gauge acts as a deformation transducer. The piezoresistive sensors have the advantage to be compact and low-cost, alike resistive strain sensors while their sensitivity is higher. However, since the piezoresistive sensors are semi-conductors, their sensitivity to temperature is very high. They also exhibit non-linearity and poor long term stability [51]. The piezoresistive sensors are primarily used in microfabricated devices [52], and allow for good performances. For example, the Micron Instruments SS-095- 060-350PU piezoresistive sensor achieves a $0.49\,nm$ resolution when used on $100\,\mu m$ full scale range and coupled with a bridge circuit excited with $2\,V$.

Nowadays, piezoelectric transducers are widely used in both actuation and sensing. They have the specificity to transform an applied voltage into a proportional strain. On the other hand, an applied strain will be converted into a proportional voltage. It makes them very easy and convenient to use. In general, multi-stage positioning systems dedicated to SPM applications combine a long stroke coarse stage with a piezoelectric actuated fine stage. This is mainly due to the high resolution and velocity that it confers. Moreover, due to the high sensitivity of piezoelectric strain sensors, they are used as position sensor in high resolution positioning applications [53, 54]. In addition, the high mechanical stiffness of piezoelectric sensors makes them stable against thermal noise. However, although this sensor exhibits very low noise at high frequencies, it suffers of dielectric leakages at low frequencies. Moreover, their hysteresis and low measurement range make piezoelectric strain sensors complex to use.

Capacitive and inductive sensors

Capacitive sensors are one of the best solution when nanometer applications are concerned. They are low cost, quasi-immune to noise and combine high linearity with excellent resolution. Moreover, capacitive sensors demonstrate a few kilohertz bandwidth, which is suitable for low velocity nanometer applications. The main drawback of capacitive sensors is their limited measurement range, of few hundreds of micrometers in general. However, some solutions to compensate from this issue exist. For instance in [55], an encoder like array capacitive sensor system is proposed to increase the measurement range. Capacitive sensors have a capacitance proportional to the inverse of

the realized displacement. Thereofore, it is essential to measure the sensor capacitance value to evaluate the measured position. This procedure can be very complex when high resolution and low noise are required. The main techniques for proper capacitance measurement are described in [56]. Conventional capacitive sensor with a $100\mu m$ range can achieve a $0.55\,nm$ if the bandwidth is reduced to $10\,Hz$ [57].

The resolution achieved by inductive sensors is also competitive for applications at nanoscale. The coil inductance of inductive sensors is proportional to the realized displacement, which induces to the same requirement as capacitive sensors in terms of instrumental electronics [56]. Moreover, these sensors are highly sensitive to temperature and exhibit magnetic hysteresis, which affects critically their accuracy [50]. Conventional inductive sensor with a $500\mu m$ range can achieve a $5\,nm$ resolution for $1\,kHz$ bandwidth [50].

Linear encoders

In [58], encoders with nanometric resolution are presented. Moreover, they can be used to measure displacements over a few centimeters with very low and periodic non-linearities. In fact, the highest resolution optical encoders operate on the principle of interferences like in [59]. Resolutions up to $0.2\,nm$ are reached over a displacement range of $50\,\mu m$. One of the most efficient linear encoder is the LIP 382 series from Heidenhain. It reaches a resolution of $0.01\,nm$ over a measuring range up to $270\,mm$[60].

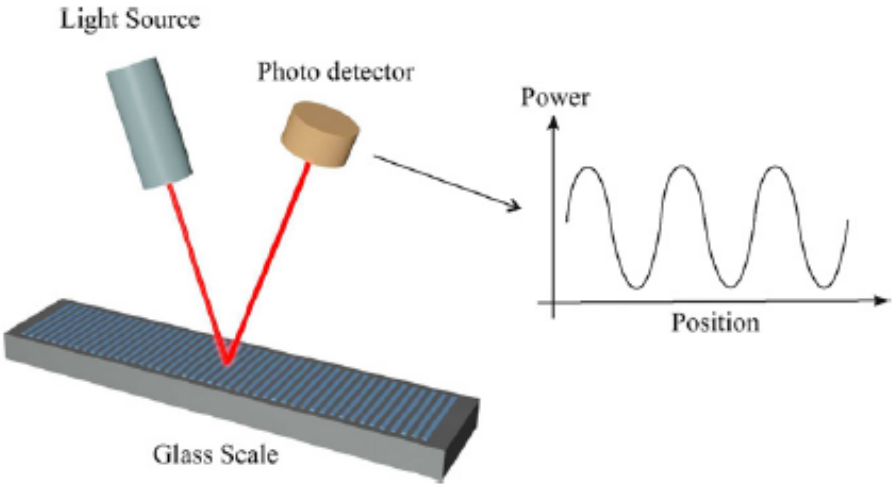

Figure 1.8 The linear encoders operating principle.

A linear encoder consists of a reference scale acting as an encoded pattern. It also includes a moving read-head with a light source and a photodetector. The functioning principle is based on a the reflection of the light stemming from a laser diode by the

reference scale onto a photodetector. As the head is moved, the peaks of power correspond to the distance between the reflective bars on the scale and between the peaks. The position can be estimated with the received power. The received power, for a constant velocity, has a periodic shape [61]. Of course, a single detection signal does not allow a proper position measurement: even if the displacement is properly computed, the direction can not be detected with a single signal. In general, two measurements in quadrature are realized and the circular Lissajous figure is used to compute the signed displacement.

Unlike other position sensors, linear encoders are able to combine high resolution with long stroke. In fact, the range of the measured voltage is proportional to the distance between two consecutive reflective bars. That makes the resolution only dependent on the encoded scale shape and the instrumented electronics. The range of measurement is only limited by the encode scale size.

Linear encoders are usual in industrial systems for nanopositioning [62][63]. The main drawback of linear encoders is their high price and sensitivity to dust and contamination. In general, several parallel detectors are used in linear encoders to compute average measurement and compensate from potential contamination of the sensor. However, the complexity of the linear encoders design and conception makes their price very high which is a main drawback for applications at nanoscale.

1.4.2 Particularities of interferometers

Laser interferometers functioning principle is often based on the Michelson interferometer, which is the most common configuration for optical interferometry. A Michelson interferometer consists of a static mirror, a moving mirror and a beam splitter. A laser source emits light that hits the partially reflective beam splitter surface, such that part of the light is transmitted in the direction of the moving mirror (for instance). Meanwhile, some of it is reflected in the direction of the static mirror. Both beams are reflected back and recombined at the beam splitter to produce the so-called interference pattern incident on a detector. This interference pattern is actually a fringe pattern and its spatial distribution depends on the laser source wavelength. If the distance between both interferometer arms is an integer number of wavelengths, constructive interferences occur. The displacement of the moving mirror, in wavelengths, is measured by counting the number of interference events that occur. In general, alike linear encoders, interferometers have two detectors positioned in quadrature on the interference pattern and the position computation is based on the circular Lissajous figure.

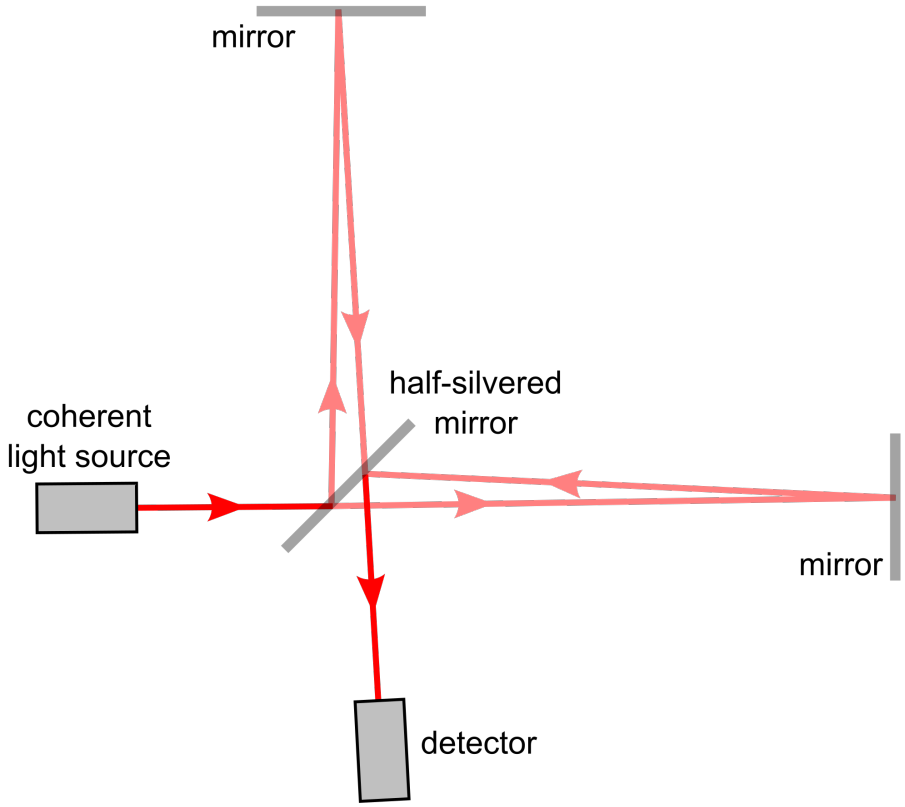

Figure 1.9 Architecture of a common Michelson interferometer.

Laser interferometers have an unlimited range even though the resolution is affected by the length of arms. Moreover, the accuracy, stability and linearity of interferometers exceed all other sensors. The main drawbacks of interferometers is their sensitivity against environmental variations and the risks to see laser beam to be broken. It results on the loose of the position. The noise of laser interferometers mainly depends on the electronics that also imposes a maximum measurement velocity.

Interferometers are widely used in nanopositioning applications that require metrologic precision like microscopy [64][65][17].

In interferometric metrology, several sources of errors must be taken into consideration in order to define the position measurement accuracy. These errors sources result from the specification of interferometric measurement, the positioning system design, the configuration, the environmental conditions and the electronics used for acquisition.

Geometrical and misalignment errors in interferometric metrology

The geometrical sources of measurement errors usually relate to a misalignment between the interferometric optical laser measurement axis and the motion axis. It

could be also because of the lack of orthogonality between the mobile mirror and the moving platform translation axis. This error is called the misalignment error.

In addition to the misalignment error, the interferometric measurement may be greatly influenced by the mechanical guidance. All the positioning system guidance technologies suffer from some parasite rotations occurring over motions, which leads to misalignment and interferometric metrology errors. These misalignments and parasite rotations lead to the well known cosine and Abbe errors. Several works and researches were realized over years of study to minimize the misalignment interferometric metrology errors. Some alignment techniques and architectures that minimize those errors have been proposed by the community [66, 45, 47, 43].

The cosine error is the most common geometric error in interferometry. It is the result of a tilt misalignment angle between the mirror axis and the optical axis (interferometer axis) or the translation axis and the optical axis. If the misalignment angle between the measurement axis and the translation axis is not constant, the error does not only affect the measured displacement but also the whole optical path length and becomes a second order Abbe error (if Abbe principle is respected).

The Abbe error is a geometric error in interferometric metrology that results from the combination of a parasite rotation and a distance between the respective intersection points of the measurement axis and the translation axis. This error results in a lever arm effect. It was described for the first time by Abbe in 1890. The classical definition of Abbe principle [67] is:

- In displacement measurement the reference should be in line with the displacement to be measured or on its extension.
- In the case when the reference is not in line with the displacement to be measured but parallel to it the distance between these parallel lines is called Abbe offset r.
- In the case of complying with the Abbe principle the angular motion error of the measuring device will cause only a second order error in measurements, which is usually negligible small. On the opposite, when it does not comply with the Abbe principle, in which the Abbe offset $r \neq 0$, a first order error $\delta = r \cdot \Delta\varphi$ will be caused. This error is called Abbe error.

In theory, one can comply to the Abbe principle by ensuring a superposition of the translation stage axis with the cubic mirror and optical axis. However, although it is possible to reduce the Abbe error effects, it is still necessary to correct this error when nanometer accuracy positioning is required for practical cases. Several techniques to

compensate for the Abbe error exist. For example, with the specific geometry of the system developed by Ducourtieux and Poyet [66]. However, the most classical technique is to measure the realized rotation while knowing the Abbe offset. Abbe principle considers the second order Abbe error negligible. However, this is not necessarily the case, particularly when nanometer accuracy is required.

Optical sources of errors in interferometric metrology

The main optical sources of errors in interferometric metrology are:

- The non-linearity between the interferometric phase shift and the realized displacement;

This error results from optical mixing, that can be due to the imperfection in the polarization mixing in the case of homodyne interferometers, or imperfection in the frequency mixing in the case of heterodyne interferometers [68]. For instance, in the case of homodyne interferometers, if the beamsplitter role is to transmit the transverse magnetic (TM) polarized component to the measurement arm, while reflecting the transverse electric (TE) polarized component into the reference arm, the beamsplitter imperfection makes a slight portion of the TE component pass to the measurement arm, and similarly a slight portion of the TM component goes to the reference arm. This contamination of the signals stemming from both interferometer arms induces a periodical error of one fringe period.

- The wavefront aberration and apodization

Wavefront aberration is the deviation of a wavefront from planarity, and apodization is the variation in intensity across a wavefront [69].

Environmental sources of errors in interferometric metrology

The main drawback of interferometers is their sensitivity to the environmental conditions. Interferometry is indeed based on the counts of fractions of wavelength, corresponding to the successive phase shifts between the measurement arm and the reference arm. Given that the wavelength directly depends on the wave propagation environment and more particularly on the refractive index, the position measurement is influenced by these parameters.

The index of refraction is a linear function of the ambient temperature, pressure, relative humidity and CO_2 concentration over moderate variation from the initial conditions. The computation of the refractive index and measurements are key points in interferometric metrology. The refractive index fluctuation may indeed introduce a 10^{-6} of optical path length error. This is not negligible when nanometer performances are aimed [70].

In addition to the medium index, interferometric metrology is also affected by dust contamination or air turbulence causing scattering effects that influence the measurement.

Laser and wavelength stability in interferometric metrology

The laser wavelength stability is also crucial in interferometry. The interferometric displacement measurement accuracy is directly correlated to the laser wavelength accuracy. The wavelength fluctuations may introduce long term errors while converting the phase into displacement. The wavelength unstability introduces an error which is directly proportional to the optical path length. This is similar to what happens with the change in refractive index.

Electronics sources of errors in interferometric metrology

Metrologic interferometers are affected by electronics resolution and noise like most position sensors. Furthermore, the main concern in metrologic interferometry is the sampling frequency. The measurement signals in interferometry are two signals in quadrature. When a constant velocity motion is performed, both signals become sine waves with the same frequency. This frequency is proportional to the displacement velocity. To ensure a proper measurement of these signals, one needs to respect the Nyquist-Shannon criterion and define a maximum measurement velocity motion with respect to the acquisition sampling frequency.

1.5 Conducting ionic electroactive trilayer polymer actuator and sensor

Since a few decades, research teams in chemistry and physics are working on the creation and integration of an ”artificial muscle” based on electro-active polymers. Compared to existing conventional technologies, these materials have a number of advantages, such as flexibility, low weight, high power/weight ratio, large deformations,

miniaturization possibility and low cost. Since electroactive polymers are based on a transducer principle, they seem to be suitable for microrobotics applications. Moreover, both sensing and actuating modes can be performed to propose innovative systems.

1.5.1 Electronically Conductive Polymer

Electronically Conductive Polymers (ECP) has a specific structure. This polymer has alternating single and double atomic bonds along its main chain. This specific conjugation makes possible the relocation of a positive charge along the chain when an electron is snatched (oxidation) chemically or electro-chemically. It results in the insertion/expulsion of solvated ions in order to maintain the global electro-neutrality of the polymer. This process induces then a change in the polymer volume. This transformation of electrical energy into mechanical one by oxydo-reduction is commonly called an electro-chemo-mechanical process [71].

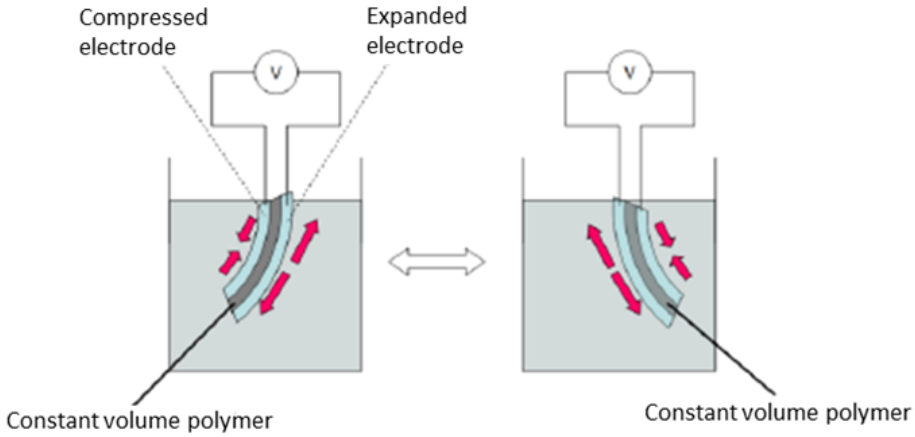

Figure 1.10 Operating principle of the PCE actuator in a three-layer configuration [72].

Based on the particularity of these polymers, several kind of actuators were developed. The most common are the volume actuators, the linear actuators and the flexion actuators. The first generation of actuators was immersed in an electrolyte solution to complete the oxydo-reduction process using the ions present in the electrolyte solution. The first study of the use of conductive polymers in actuators development was realized by Baughman *et al.* in 1991 [73]. This study of the electro-chemical to mechanical transduction applied to actuator performances highlights the highest power to mass ratio of any actuators technology as investigated by Hunter and Lafontaine in 1992 [74].

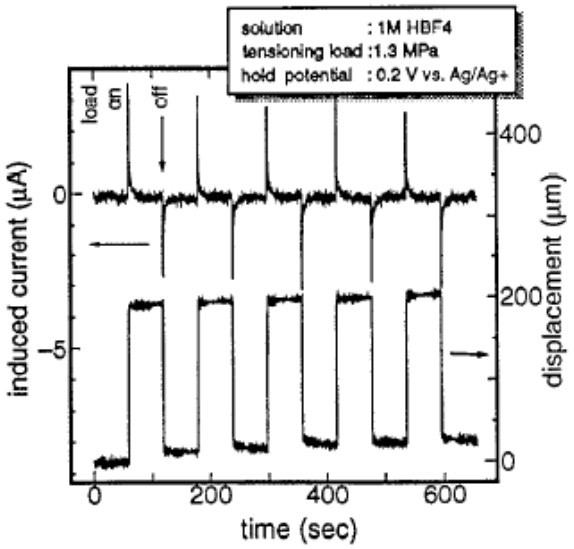

Figure 1.11 The typical response of current and displacement with several strain cycles [75].

Moreover, the ECP can also be used as flexion sensor. The use of conducting polymers as deformation sensors was first highlighted by Takashima *et al.* in 1997. They observed a measurable $3\,\mu A$ peak of current when a $200\,\mu m$ deformation was imposed to a polyaniline film emerged in an electrolyte [75] (see fig.1.11). Takashima *et al.* have attributed this effect to a ionic charge diffusion between the film and the electrolyte.

1.5.2 The ionic Electro-Active Polymers flexion actuators

The ionic Electro-Active Polymer (IEAP) flexion actuator is the most studied ionic ECP based actuator in recent years. It's flexibility, lightness and miniaturization characteristics open up new prospects for applications. In the literature, the capabilities of the flexion IEAP actuator to reproduce the functions and performances of biological muscles was widely studied and highlighted. This allowed it to be qualified as the precursor of artificial muscle [76, 77].

Several different IEAP technologies were developed over the last thirty years. One can distinguish [78]:

- The simple IECP is immersed in an electrolyte solution and actuated with respect to a metallic electrode.
- The bilayer IEAP is composed of an ECP stuck to a constant volume component. Its principle is similar to the simple ECP electroactive polymer requiring a metallic electrode.

- The trilayer IEAP is composed of two ECP stuck on each side of a constant volume component. It does not require the metallic counter-electrode and the two ECP simply act as anode and cathode.

The first IEAP working in free air appeared at the end of the 90's [79, 80]. These devices are trilayers IEAP that use a polymer electrolyte support (PES) separator between the two ECP. This separator is inflated by an electrolyte solution. The required ions diffusion for the IEAP operation process are no more provided by the immersion in the electrolyte solution but by the inflated PES between the two ECP. In the case of the trilayer IEAP, the actuation is obtained with the compression of an ECP and the expansion of the other. Moreover, considering the sensing capabilities of the ECP, this device can be synthesized either for actuation or sensing applications.

In his PhD, Festin has widely investigated the effects of the used electrodes [72], the PES nature, and the inflation ratio of a trilayer IEAP on its actuating and sensing performances. He has demonstrated that the observed potential difference (in sensor mode) as well as the deformation ratio (in actuator mode) was dependent of the quantity of electrolyte inflated in the PES and not the electrodes nature [72]. Moreover, he demonstrated that the inflation ratio has a peak value from which the performances are no more affected by the increase in electrolyte concentration. Finally, he confirmed that the electroactive propriety of this kind of polymers is due to a ionic diffusion between the two electrodes of the polymer through its PES. Moreover, this was also demonstrated by Shoa *et al.* [81] while coupling an actuator polypyrrole with a sensor polypyrrole. Both were immersed in the same electrolyte solution.

1.5.3 A trilayer polymer designed by the LPPI

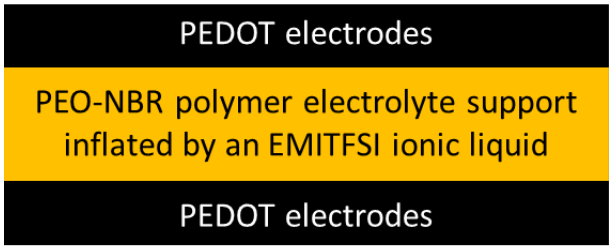

Figure 1.12 Structure of the PEO-NBR-PEDOT electro-active polymer [71].

The conducting trilayer polymer used in this work is composed of two PEDOT (poly(3,4-éthylènedioxythiophène)) electrodes separated by a PEO-NBR (poly(oxyde d\textquoteright éthylène)-nitrile butadiène rubber) polymer electrolyte support (PES)

inflated by an EMITFSI (Bis-(trifluoromethylsulfonyl) imide de 1-ethyl-3- methylimidazolium) ionic liquid. This IEAP was synthesized by our partners from the Physicochemistry of Polymers and Interfaces Laboratory (LPPI - Cergy Pontoise University) [71].

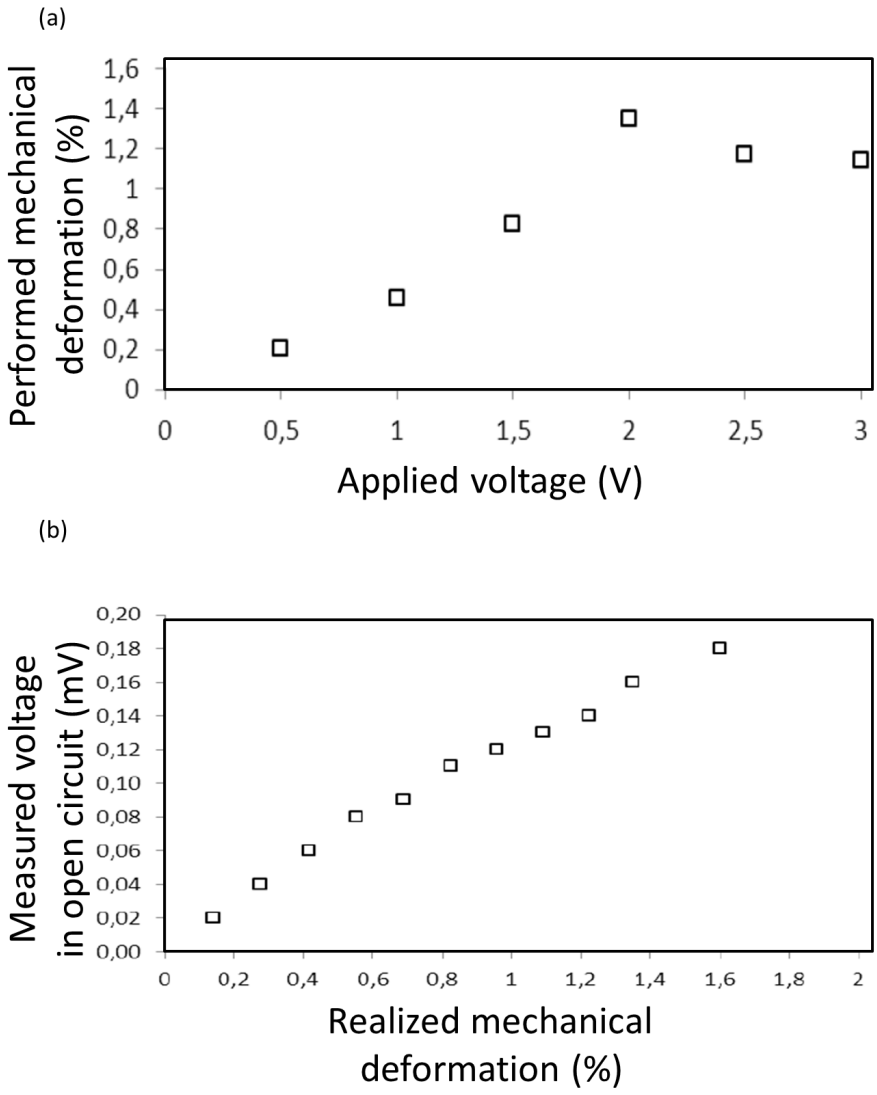

Figure 1.13 Linearity characterization (a) in actuation mode, and (b) in sensing mode [72].

The originality of this material is the use of a PEO network. It gives the PES an enhanced ionic conductivity and a NBR network that improves the mechanical properties of the polymer. This enhancement opens up new applications perspectives, like the integration on biomimetic devices [82]. Moreover, this IEAP has the particularity to use ECP interpenetrated in the PES. This specificity of the device resolves all the classically encountered delamination problems associated to multi-layers devices. As a consequence, more than $7 \cdot 10^6$ expansion/compression cycles can be performed before

it deteriorates. Nowadays, this is the best result obtained with this kind of technology. In the literature, no more than hundreds of thousands cycles were achieved with IEAP based on other than NBR IPN. In most actual cases, the deterioration of the device occurs because of the delamination of the multi-layer configuration. Thanks to the introduction of PEO, this device exhibits a high electronic conductivity. Therefore, it can be used in both actuation and sensing modes.

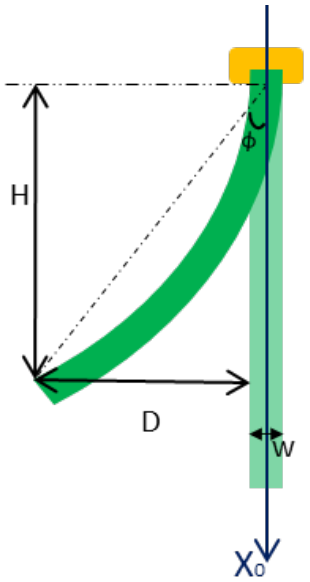

Figure 1.14 Demonstration of the parameters used in the computation of the percent of deformation. D the realized displacement of the free end perpendicularly to the axis X_0 defined by the device in it's rest position, H the distance between the free and the fixed ends of the device with respect X_0 of the axis, ϕ is the angle between the polymer free end and its rest position and w is its thickness.

Another characteristic of IEAP is the linearity both in actuation and sensing modes. Festin has designed this IEAP with the objective to achieve linearity when used both as actuator or sensor. Fig.1.13 represents the results obtained when the device was characterized on both actuation and sensing modes. The actuation characterization demonstrates a maximum deformation threshold value of 1.35 %. The percent of deformation is computed using an equation extracted from the theory of the free end cantilever beam, as demonstrated by Sugino *et al.* [83]:

$$\Delta\varepsilon = \frac{2 \cdot D \cdot w}{(H^2 + D^2)} \cdot 100 \tag{1.1}$$

with $\Delta\varepsilon$ the percent of deformation, D the realized displacement of the free end perpendicularly to the axis X_0 defined by the device in it's rest position, H the distance between the free and the fixed ends of the device with respect of the X_0 axis, such that

$\phi = arctan(\frac{D}{H})$ is the angle between the polymer free end and its rest position (see fig.1.14), and w is the device thickness.

Finally, from user's point of view, the deformation of the polymer generates a current and a voltage between the bounds. On the other hand, a current circulating between the bounds generates a deformation of the polymer. In addition, the input for actuation is in the voltage range of $0 - 5\,V$, while the output for sensing is in the voltage range $0 - 0.3\,mV$. It makes possible to realize both sensing and actuation within the same device [84].

1.5.4 Ionic Electro-Active Polymer (IEAP) characterizations

The analytical impedance model for the IEAP was proposed by Shoa *et al.* in 2010 [85]. In this work, a single ECP IEAP was studied and modeled. This classical IEAP consists in an ECP and a metallic electrode immersed in an electrolyte solution. As explained previously, this kind of IEAP principle is based on the voltage difference between the ECP and the classical electrode. A potential difference can be imposed to actuate the ECP and leads to a deformation. In sensing mode, this potential difference can be measured to estimate the ECP deformation. Nevertheless, in both cases, the deformation of the ECP is caused by ions exchange inside the electrolyte solution. In the work of Shoa *et al.* [85], they proposed to model the electrolyte solution as a simple resistor. The ECP has a two dimensional RC transmission lines. Based on this model, the actual analytical impedance model of a trilayer IEAP was constructed by duplicating the ECP analytical impedance model on the second ECP electrode [86, 87].

Apart from analytical impedance model, some frequency response study was also realized on both actuator and sensor mode of this kind of devices [81, 88]. Actually, a close look at the obtained frequency response of these IEAP validate the previously presented analytical model. The frequency response has the behavior of a RC transmission line system [89].

Mechanical characterization was also performed on this kind of devices to identify the forces when it is used in actuation mode. The study of the elastic modulus (Young's modulus) of the ECP was also realized. In fact, the elastic modulus of some conducting polymers changes during operation as a function of oxidation state, like the polypyrrole ECP studied in [90]. However, for polymers made by LPPI, for a small strain ($< 10\,\%$) oxidation state, the Young modulus of the IPN PES remains quite constant [91]. The mechanical characterization of the PEDOT ECP electrode (see [86]) demonstrates a 16% drop of it's Young modulus when a voltage in the range $[-1, 1]\,V$ is applied between the

ECP and a reference electrode. Authors claim that the modulus drops to a plasticization of the PEDOT layer. It is due to the incorporation of anions during oxidation [86]. The different mechanical characterization, realized on this kind of devices, show that the IPN IEAP can generate a force of at most $30\,mN$ when it is used as actuator [78, 92]. However, to overcome this constraint and to increase the generated force, Farajollahi *et al.* have proposed stacking trilayers to increase force generation with some success [93].

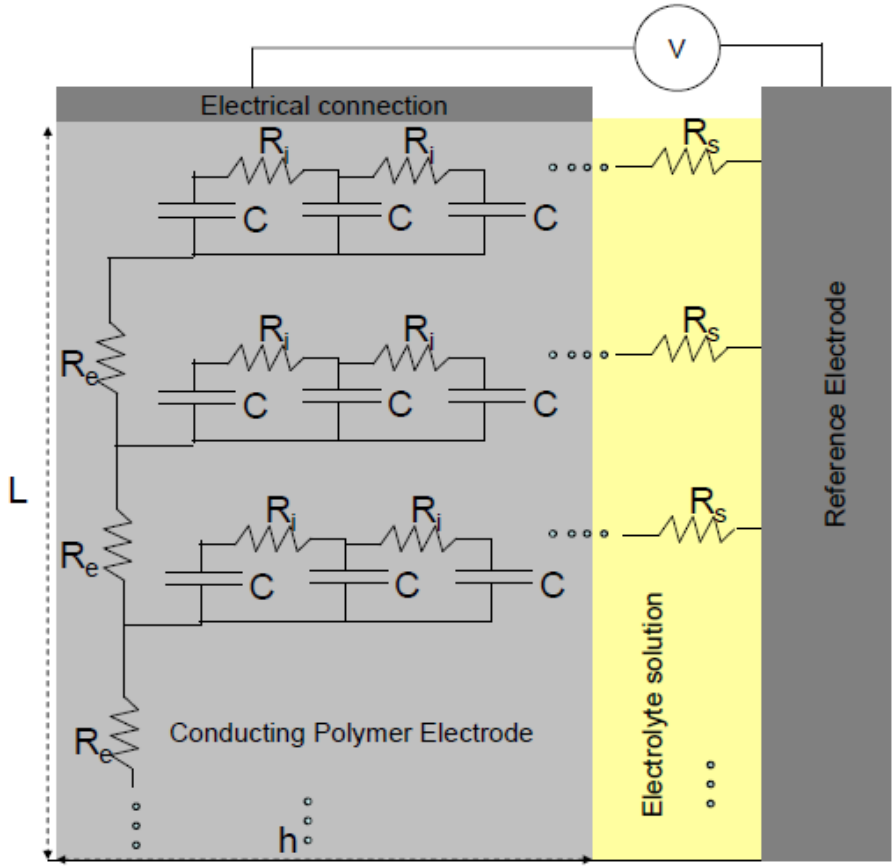

Figure 1.15 The analytical impedance mode proposed by Shoa *et al.* [85].

In addition, John *et al.* [94] have studied the effect of the IEAP dimension on its performances. They have reported that the IEAP bandwidth increases when the device length and the ECP thickness decrease and when the PES thickness increases. Also, the sensitivity increases while the width of the device and the thickness of PES increase.

Finally, in her PhD works Fannir [92] widely studied the effect of the environment on the IPN IEAP. It was demonstrated that this device is able to operate with high environmental temperatures(up to 285°C).

Chapter 2

The PicoMove interferometer characterization

Contents

2.1 Introduction

Since a few years, the LISV closely participated with our partner Teemphotonics in the development of an original sensor which has been used for specific applications like multi-scale positioning. Applications dedicated to nanoscales can relate to the manipulation of nano-objects [17] but also to the positioning at nanometer level of macro-objects (sample-holder or macro-tools). In that case, the required performances are slightly different as multi-scale capability is a concern. The stroke may be indeed in a centimetric range while the accuracy should be sub-nanometric. Nowadays, multi-scale is still a challenge. In the literature, high resolution and high accuracy lead generally to a limited stroke lower than 1 mm.

This chapter presents an interferometer with a fully embedded optical chip. In that way, the end-user should expect to set up his system without thinking of possible complex optical paths. In addition to its very good performances, this sensor demonstrates that low sensitivity to external disturbances and ease of use can be achieved. The PicoMove interferometer uses an external telecom source, and integrated optical waveguides are inside the package. It partially explains why this sensor may be inexpensive compared to other interferometers. The aim of this chapter is mainly to evaluate the interferometer in quasi-static conditions or with very small displacements in order to analyze the noise level at high acquisition frequency and estimate the long term performances. Dynamic measurements are also presented to demonstrate the subnanometric performances of the sensor.

In section 2, the design of the different prototypes that led to the Picomove interferometer are described. In section 3, the functioning principle and the equations that govern the system are presented. And in section 4, the experimental setup is described and the results are presented and discussed.

2.2 The PicoMove interferometer design and prototypes

The PicoMove interferometer is the result of the collaboration of the CEA/DASE, the TeemPhotonics company and the LISV. Different prototypes have been developed through several years of work and collaboration, the first one was a seismological dedicated interferometer developed at the CEA/DASE in order to evaluate the potential of this technology for seismological applications [95]. The second one was an integrated optical waveguide interferometer based on the previous prototype and developed by TeemPhotonics, to estimate the influence of the change of technology. The capabilities were characterized at the LISV in close collaboration with the CEA/DASE [96].

And finally, the first commercial version was recently released by TeemPhotonics, which capabilities are studied in this chapter [97].

2.2.1 The first prototypes of the interferometer

The first prototype of this interferometer was a macroscopic modified Michelson interferometer dedicated to seismological application [95]. This prototype has been developed from a coaxial Michelson interferometer using bulk optics (Fig.2.1). A linearly polarized beam issued from a frequency stabilized He-Ne laser ($\lambda = 632.8\,nm$, horizontal polarization orientation) is injected into polarized beam splitter PBS1. The beam is transmitted to a Quarter-Wave Retarder oriented with an angle of 45° from the horizontal plane, as a consequence, the injected beam is divided out into two linearly polarized beams, one per neutral axes of the retarder. Then, a beam splitter (BS) split the beam into two parts: one is transmitted into the interferometer, and the second one is transmitted to a photo-diode (PD1) in order to measure the intensity of the input beam.

The beam injected into the interferometer is then transmitted through a Half-Wave Retarder in order to rotate the polarization directions of an angle equal to 45°. As a result, one polarization direction is horizontal and the other one is vertical. Then, a polarized beam splitter (PBS2) transmits the horizontally polarized beam into one arm of the interferometer, and the vertically polarized beam in the other arm.

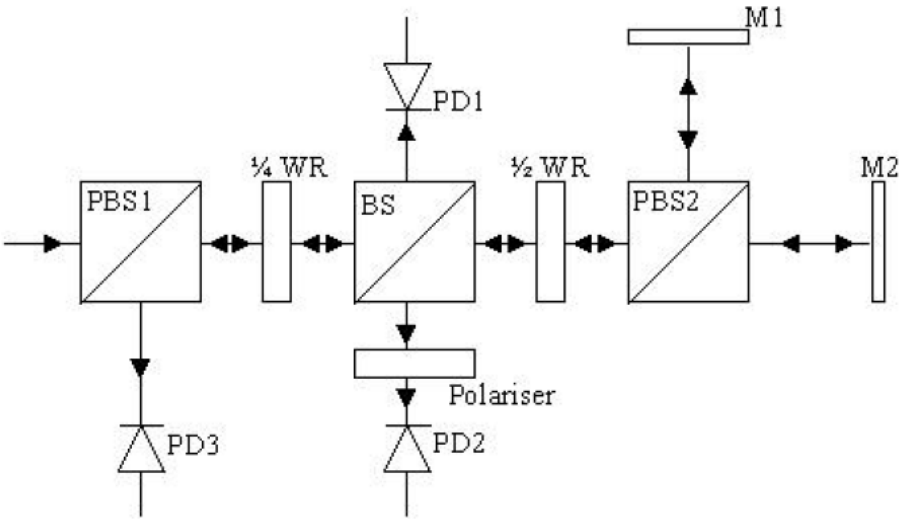

Figure 2.1 Schematic view of the prototype Michelson interferometer [95]

Both returning beams are transmitted back to the ½WR. The 2 polarization directions are rotated by an angle equal to 45°. BS split the beam into two parts. One

part is transmitted to a photo-diode (PD2) through a polarizer (first interferometric signal). The second part is transmitted to 1/4 WR, so a phase shift equal to $\pi/2$ is applied and the polarized beam splitter transmits the second interferometric signal to the last photo-diode (PD3) in order to detect and record it with a $\pi/2$ phase shift.

Tests were carried out to validate the operation of this transducer and to estimate its main characteristics for seismological applications, focusing on transducer motion range and intrinsic noise. The prototype intrinsic noise reaches levels as small as $100\,fm/\sqrt{Hz}$ around $8\,Hz$ [95].

Also, based on this work two prototypes were developed in collaboration with the TeemPhotonics company. Two modified Michelson interferometers were designed with integrated optics component to enhance the robustness to environmental disturbances, the first one in visible ($632\,nm$) and the other in infrared range ($1550\,nm$) [98]. Also, the experiments showed that the length of the reference arm path is highly correlated to the noise level, and reducing the reference arm path length improved the performances.

2.2.2 The integrated waveguide prototype

The prototype working in infrared range ($1550\,nm$) was fully integrated in an optical chip with an optical waveguide structure. The technology used for the chip is described in [99]. It was made by the TeemPhotonics company based on their knowledge of integrated optics process developed in telecom fields. All the inputs and the outputs of the chip are fibered and this one is inserted in a package made of steel for vibration isolation and thermal homogeneity (Fig.2.2).

At the output, a collimating Grin lens ensures a useful range of several centimeters. It focuses the beam toward a mobile mirror and makes the system very easy-to-use because there is no need for other lenses. Coming back from the mobile mirror, the light is re-injected in the chip. Unlike the first prototypes, this one has four outputs signal, two references signals (parts of the source and retro-injected signals) and two measurement signals (previously two measurement signals and one reference signal, part of the laser source signal). The four outputs are sent to a photo-detector modules to obtain voltages with trans-impedance structures.

The two references signals are used to enhance the contrast by suppressing the offsets of the two measurement signals. It enhances then the signal to noise ratio by suppressing the amplitude noise of the laser source or amplitude fluctuations due to the retro-injection perturbations caused by vibrations. The role of each signal will be described in next section. The tuning of the system (interferometer-mobile mirror) relies on the optimization of the retro-injected signal level in the chip.

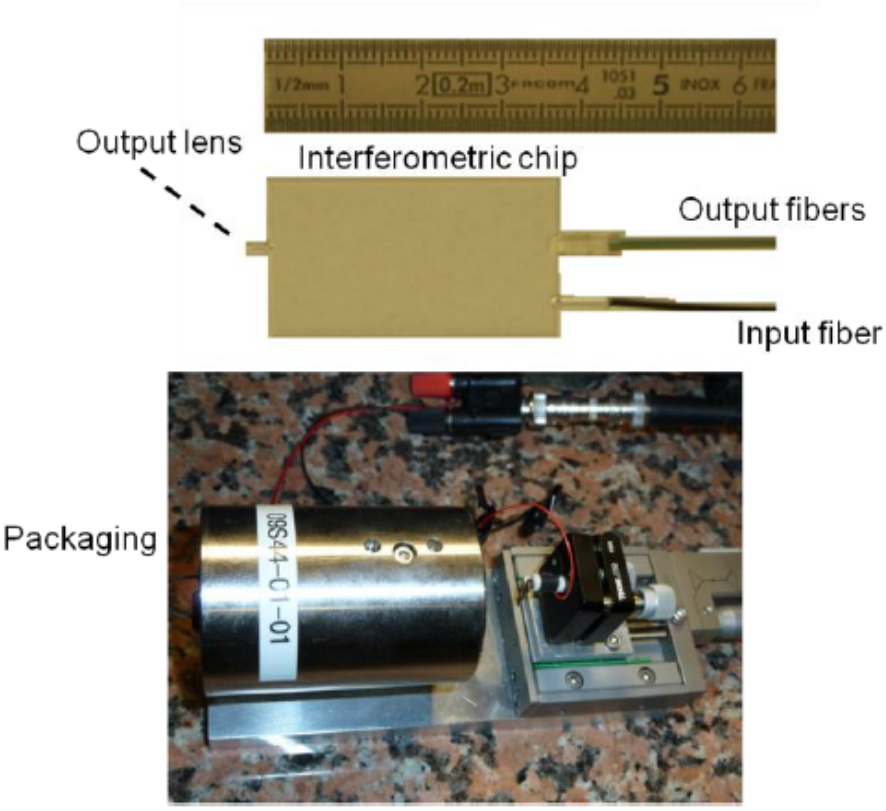

Figure 2.2 Photography of the interferometer: a) Chip with an integrated waveguide; b) The interferometer inside its packaging and an external mobile mirror moved by a piezoelectric actuator.

This interferometer was tested and characterized at the LISV [96]. The metrological study was focused on the resolution and the noise level of the sensor. A standard Allan deviation lower than $50\,pm$ has been observed in standard environment for integration times in the range $[5.10^{-5}, 10^{-3}]\,s$. Power spectral densities up to $150\,fm/\sqrt{Hz}$ at $10\,kHz$ was achieved.

2.2.3 The PicoMove interferometer

The main evolutions in this final product are:

- It's higher compactness making it usable in highly integrated systems (from a cylinder of $40\,mm$ length and $10\,mm$ radius to a parallelepiped of $59x27x8.5\,mm^3$)
- The suppression of the reference arm path, a part of the input signal is directly redirected to the interference area.
- The change of the initial modified Michelson design of the interferometer in the beam combination part to avoid integrated optical component (use of young's double slit experiments).

The optical beam combination

Like classified by [100] the different types of beam combinations (Fig.2.3) are:

- The co-axial combination, when the beams seems to propagate from the same direction as in the Michelson laboratory experiment.

- The multi-axial combination, when the beams seems to propagate from different directions as in the Young's double slit experiment.

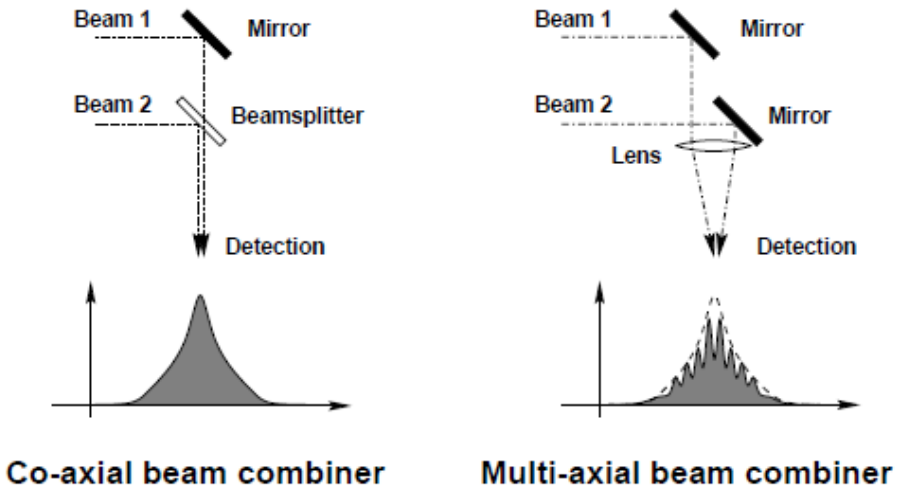

Figure 2.3 The different types of beam combinations in classical optics with the profiles of the output intensities [99]

In bulk optics, the co-axial combination is performed with a beam splitter whereas the multi-axial combination is done by focusing the different beams on the same spot. But in the case of multi-axial combination, the differential tilt between the beams produces fringes on the point spread function. The co-axial combination can be regarded as a particular case of the multi-axial mode where all the beams are superposed without tilts.

Unlike the previous versions of this interferometer where co-axial combination was performed, an Interference Free Propagation Zone based on the Young's double slit experiment was introduced to realize the multi-axial combination between the source signal and the retro-injected signal (Fig.2.4).

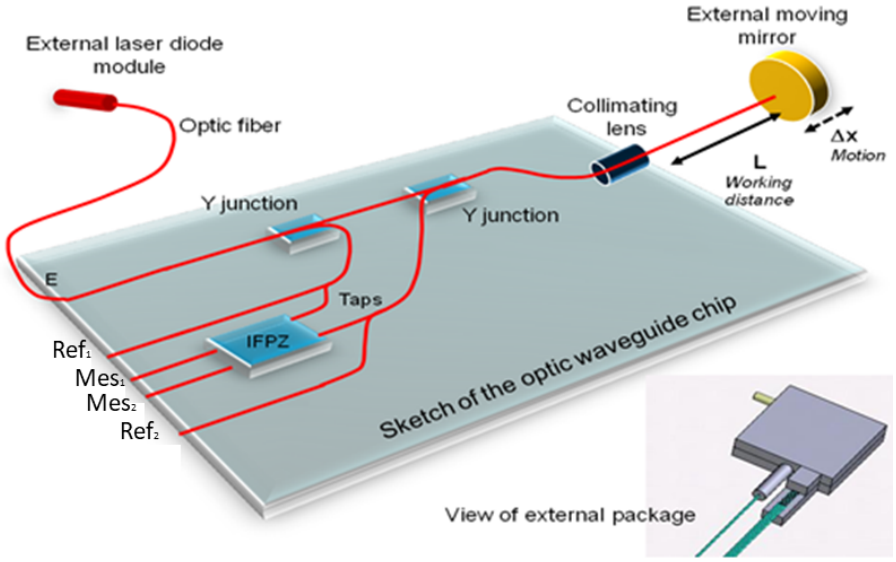

Figure 2.4 Optical representation with simplified optical paths of the beam in the chip.

Design of the Interference Free Propagation Zone (IFPZ)

The optical design of the PicoMove is then a mix between a Michelson interferometer and a Young interferometer. Indeed, the general architecture of the design is based on a Michelson interferometer since we use a reference arm with a fixed length and an arm with a varying length for measurement. Nevertheless, in order to get two outputs in quadrature, the interference between the two arms is implemented through a Young interferometer. The quadrature between Mes_1 and Mes_2 is assured when designing the chip.

Fig.2.5 (a) represents the interference between two rays, which beams are misaligned by an angle θ and separated by a distance d_{in}, while (b) is a zoom of the interference area that represents two interference points separated by a distance x. The optical path-length difference Δs between the two paths to reach the points A and B (demonstrated by [101]) is expressed:

$$\Delta s = \frac{n \cdot d_{in}}{L} \cdot x \tag{2.1}$$

if $L \gg d_{in}$ ($tg(\theta) = \frac{d_{in}}{L} \simeq sin(\theta)$), and while:

- n is the effective index of the planar waveguide in the IFPZ area,
- L is the distance between the input and the output of the IFPZ,

- d_{in} is the distance between the waveguides at the input of the IFPZ area.

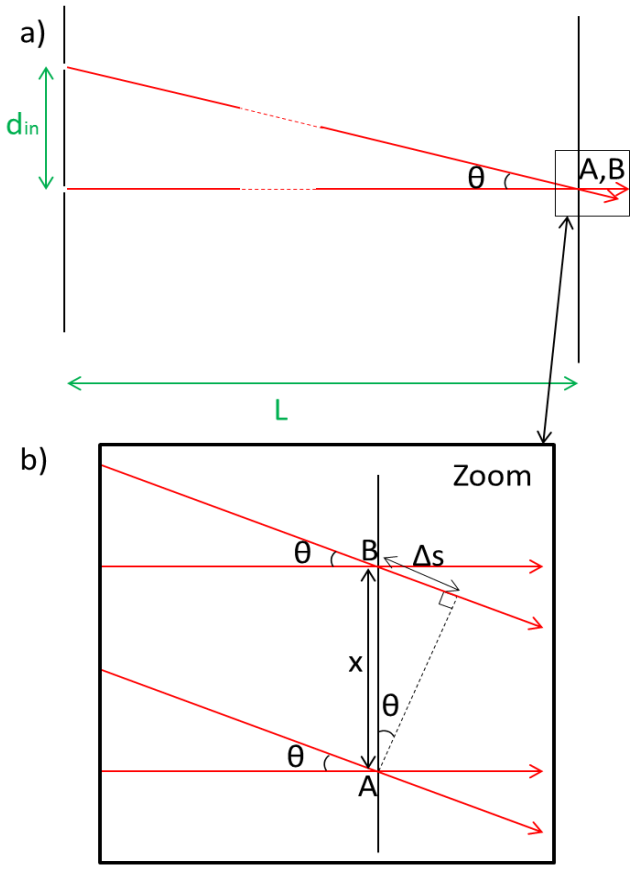

Figure 2.5 Schematic of the path-length difference of two interfering rays.

And the spatial period of the sinusoidal interference pattern at the output of the IFPZ D is:

$$D = \frac{L \cdot \lambda_0}{n \cdot d_{in}} \qquad (D = x \; if \; \Delta s = \lambda_0), \tag{2.2}$$

where λ_0 is the operating wavelength in vacuum.

In the conception phase, the distance d_{out} between the waveguides at the output of the IFPZ is directly transferred from the photomask to the glass wafer through a photo-lithography step with a resolution better than $0.1\,\mu m$. d_{out} is such that the two output signals are in quadrature (fig.2.6):

$$d_{out} = \frac{D}{4} = \frac{\lambda_0 \cdot L}{4 \cdot n \cdot d_{in}}. \tag{2.3}$$

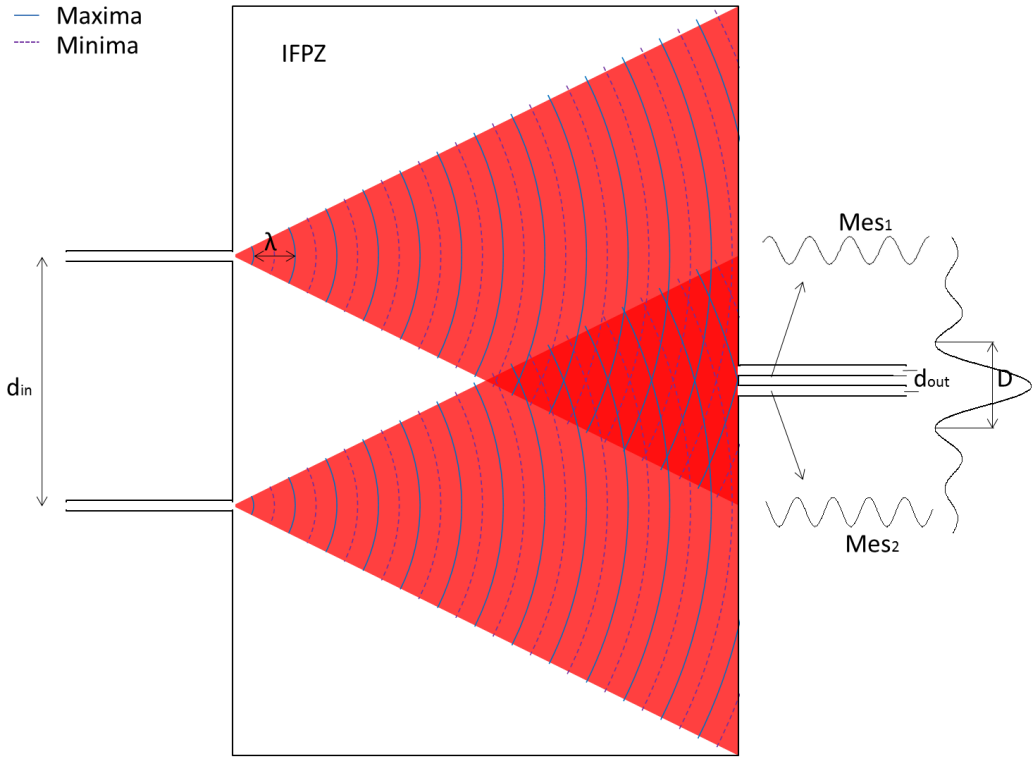

Figure 2.6 Schematic of the IFPZ

TeemPhotonics announces an optical loss in the IFPZ function in the 12-14 dB range. Comparing to other solutions with lower optical loss, the implementation of an IFPZ allows a very low sensitivity to technological fluctuations of the manufacturing process. Two Y junctions separate the beam along the measurements path and two taps provide the two reference arms (Ref_1 and Ref_2) with a small amount of power (junction with 1 % to 5 % of coupling). At the output of the interference area, two measurements signals are available (sine-cosine outputs, Mes_1 and Mes_2). The four outputs are converted into voltages with the photo-detector modules (made with classical trans-impedance structures). Finally the optical interference between the reference path and the mobile path is made in the IFPZ (Interference Free-Propagation Zone) which is a double-slit structure.

2.3 The position computation

The PicoMove interferometer has a calibration phase before use. Once calibrated, real time measurements with high resolution can be achieved.

2.3.1 The interferometer equations

The two references signals Ref_1 and Ref_2 are parts of the two injected signals (laser source and retro-injected signals), such as:

$$\begin{cases} Ref_1 = k_1 \cdot S_1 \\ Ref_2 = k_2 \cdot S_2 \end{cases} . \tag{2.4}$$

Where:

- S_i is the injected signal in the arm i of the chip (1 for the laser source and 2 for retro-injected signals) after the Y junctions, and before the taps.

- k_i is the transmitting coefficient of the tap that the injected signal provides from to the reference signal Ref_i. It includes the optical fiber insertions, the Y junctions and the taps.

It means that the light intensities I_i at the inputs of the IFPZ can be expressed as:

$$\begin{cases} I_1 = \frac{1-k_1}{k_1} \cdot Ref_1 \\ I_2 = \frac{1-k_2}{k_2} \cdot Ref_2 \end{cases} . \tag{2.5}$$

Then the measurement signals at the output of the IFPZ can be expressed by the interference formula:

$$\begin{cases} Mes_1 = I_1^1 + I_2^1 + 2 \cdot \sqrt{I_1^1 \cdot I_2^1} \cdot cos(\alpha^1) \\ Mes_2 = I_1^2 + I_2^2 + 2 \cdot \sqrt{I_1^2 \cdot I_2^2} \cdot cos(\alpha^2) \end{cases} . \tag{2.6}$$

Where:

- α^i is the phase shift between I_1 and I_2 seen by the output Mes_i.

- I_i^j is the light intensity stemming from the arm i and seen by the output Mes_j.

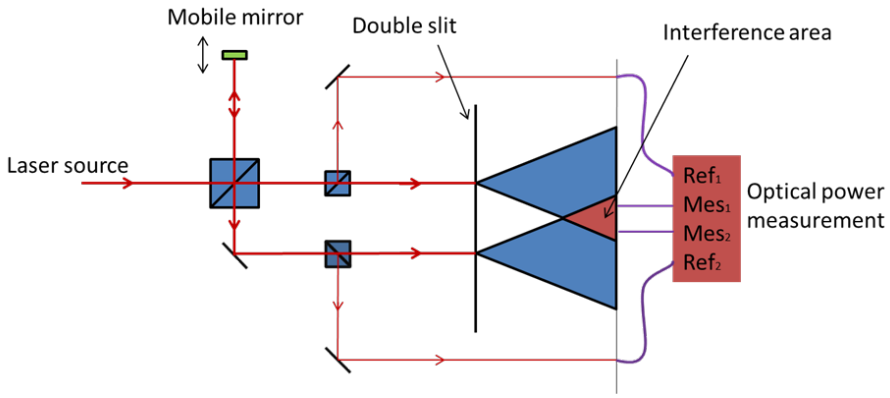

Figure 2.7 Principle of the PicoMove interferometer.

Finally, from the point of view of the user, one can consider the interferometer chip as a non linear quadruple with Ref_1 and Ref_2 as inputs and Mes_1 and Mes_2 as outputs. such as:

$$\begin{cases} Mes_1 = Ks_{11} \cdot Ref_1 + Ks_{21} \cdot Ref_2 + 2 \cdot \sqrt{Ks_{11} \cdot Ref_1 \cdot Ks_{21} \cdot Ref_2} \cdot cos(\alpha^1) \\ Mes_2 = Ks_{12} \cdot Ref_1 + Ks_{22} \cdot Ref_2 + 2 \cdot \sqrt{Ks_{12} \cdot Ref_1 \cdot Ks_{22} \cdot Ref_2} \cdot cos(\alpha^2) \end{cases} \tag{2.7}$$

Eq.2.7 represents an ellipse (well known in interferometry) of abscissa and ordinates Mes_1 and Mes_2 respectively.

2.3.2 The PicoMove calibration

First, each chip is calibrated before use. The Y junctions may be indeed slightly unbalanced and the insertion loss can also be different from one chip to another. The calibration aims to measure the Ks_{ij} parameters that characterize the chip and coupling between the four outputs. The calibration can be made once or every time that the chip is manipulated because the parameters are dependent also on the insertion loss in the fibers that can be very sensitive.

The Ks_{1i} computation

The first calibration step, is the measurement of Mes_1 and Mes_2 while the retro-injected signal is blanked ($Ref_2 = 0$) thanks to a shutter, then based on eq.2.7 one can see that:

$$\begin{cases} Ks_{11} = \frac{Mes_1}{Ref_1} \\ Ks_{12} = \frac{Mes_2}{Ref_1} \end{cases} . \tag{2.8}$$

The Ks_{2i} computation

For the second calibration step a displacement is imposed to obtain the sinusoidal response on Mes_1 and Mes_2, then Mes_i^{max} and Mes_i^{min}, the maximum and minimum values of the sinusoidal waveform i, are determined.

Based on the eq.2.7 again, one can see that:

$$\begin{cases} Mes_i^{max} = Ks_{1i} \cdot Ref_1 + Ks_{2i} \cdot Ref_2 + 2 \cdot \sqrt{Ks_{1i} \cdot Ref_1 \cdot Ks_{2i} \cdot Ref_2} \\ Mes_i^{min} = Ks_{1i} \cdot Ref_1 + Ks_{2i} \cdot Ref_2 - 2 \cdot \sqrt{Ks_{1i} \cdot Ref_1 \cdot Ks_{2i} \cdot Ref_2} \end{cases} . \tag{2.9}$$

Finally based on the eq.2.9 and using the previously determined Ks_{1i}; the Ks_{2i} parameters are calculated:

$$Ks_{2i} = \frac{\frac{Mes_i^{max}+Mes_i^{min}}{2} - Ks_{1i} \cdot Ref_1}{Ref_2}. \tag{2.10}$$

Typical values for the Ks_{ij} parameters are around 0.6 to 0.75.

The output signals Mes_1 and Mes_2 are in quadrature but because of the IFPZ imperfection combined to the insertion loss in the fibers, an additional phase shift must be considered between the two measurement signals such that:

$$\alpha^2 = \alpha^1 + \pi/2 + \alpha_0. \tag{2.11}$$

And using the calculated Ks_{ij} parameters and the two reference signals (Ref_1 and Ref_2), the outputs signals Mes_1 and Mes_2 can be normalized from eq.2.7 such that:

$$\begin{cases} Mes_{1,norm} = \frac{Mes_1 - (Ks_{11} \cdot Ref_1 + Ks_{21} \cdot Ref_2)}{2 \cdot \sqrt{Ks_{11} \cdot Ref_1 \cdot Ks_{21} \cdot Ref_2}} = cos(\alpha^1) \\ Mes_{2,norm} = \frac{Mes_2 - (Ks_{12} \cdot Ref_1 + Ks_{22} \cdot Ref_2)}{2 \cdot \sqrt{Ks_{12} \cdot Ref_1 \cdot Ks_{22} \cdot Ref_2}} = cos(\alpha^2) \end{cases} \tag{2.12}$$

In interferometry the quadrature between the two measurement signals is actually imposed. To be able to achieve the previously presented normalization, and simplify the computation of the phase shift between the two signals, the interference formula (eq.2.6) describes an ellipse when the measurement signals are defined as abscissa and ordinate axis. This ellipse is commonly called the Lissajous ellipse and it's estimation is essential for the interferometric position computation.

The Lissajous ellipse estimation

The normalization allows to be more robust to power fluctuations of the source (thanks to Ref_1) and of the retro-injected signal (thanks to Ref_2). But, the experiment

showed that the $Mes_{i,norm}$ don't describe a perfect centered and normalized ellipse, such that the following assumption was done:

$$\begin{cases} Mes_{1,norm} = X_0 + a * cos(\alpha^1) \\ Mes_{2,norm} = Y_0 + b * sin(\alpha^1 + \alpha_0) \end{cases} \tag{2.13}$$

with:

- $X_0 = \frac{Mes^{max}_{1,norm} + Mes^{min}_{1,norm}}{2}$
- $a = Mes^{max}_{1,norm} - X_0$
- $Y_0 = \frac{Mes^{max}_{2,norm} + Mes^{min}_{2,norm}}{2}$
- $b = Y_0 - Mes^{max}_{2,norm}$

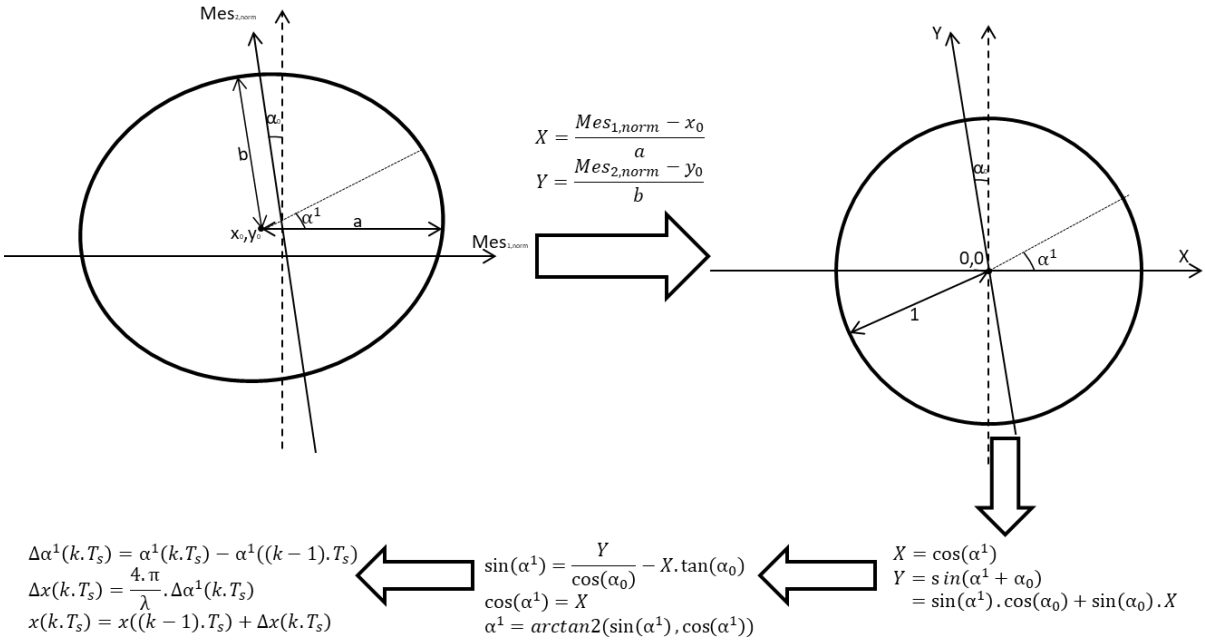

Figure 2.8 The Lissajous ellipse and the position computation

Fig.2.8 show an example of the estimated Lissajous ellipse. Once the ellipse is estimated, one can define a couple (X,Y) that describe a centered normalized ellipse while:

$$\begin{cases} X = \frac{Mes_{1,norm} - X_0}{a} = cos(\alpha^1) \\ Y = \frac{Mes_{2,norm} - Y_0}{b} = sin(\alpha^1 + \alpha_0) \end{cases} \tag{2.14}$$

The α_0 computation

Finally, α_0 can be calculated by 4 different ways:

- $\alpha_0 = arcsin(-Mes_{2,norm})$ when $Mes_1 = Mes_1^{max}$
- $\alpha_0 = arcsin(Mes_{2,norm})$ when $Mes_1 = Mes_1^{min}$
- $\alpha_0 = arcsin(-Mes_{1,norm})$ when $Mes_2 = Mes_2^{max}$
- $\alpha_0 = arcsin(Mes_{1,norm})$ when $Mes_2 = Mes_2^{min}$

In our experiments we choose to compute the mean value of the α_0 calculated with the 4 different ways.

2.3.3 The position computation

The position computation is done based on the method described in [102]. Once the chip is calibrated, the first step of the position computation is the signal normalization with eq.2.12. Then using eq.2.14 the couple (X,Y) is calculated and the output phase α^1 of the interferometer is determined with:

$$\begin{cases} cos(\alpha^1) = X \\ sin(\alpha^1) = \frac{Y}{cos(\alpha_0)} - X \cdot tan(\alpha_0) \end{cases} \tag{2.15}$$

Then:

$$\alpha^1 = arctan2(sin(\alpha^1), cos(\alpha^1)) \tag{2.16}$$

And finally the output expression of the displacement of the mobile mirror over one sampling period is:

$$\Delta x(k \cdot T_s) = \frac{\Delta\alpha^1(k \cdot T_s) \cdot \lambda}{4 \cdot \pi} \tag{2.17}$$

Where:

- T_s is the sampling period.
- k is the sample index.
- $\Delta\alpha^1(k \cdot T_s) = \alpha^1(k \cdot T_s) - \alpha^1((k-1) \cdot T_s)$ is the phase variation over one sampling period.
- $\lambda = \frac{\lambda_0}{n}$ is the wavelength in the experiment environment of effective index n.

The computation of the phase is made in real-time and the bandwidth of the interferometer output is actually only limited by the sample frequency of the data acquisition board. The only limitation on the experiment is the maximum displacement speed. Indeed, the maximum phase shift between two acquisitions should be π because of the indeterminate forms and Shannon criteria. If the phase variation is higher than π it is impossible to determine the displacement direction. If the speed is too high that a displacement of over $\frac{\lambda}{4}$ is realized during one sampling period? Or if a displacement of less $\frac{\lambda}{4}$ than was realized in the other direction?

Then to avoid this indetermination situation, we choosed to define the maximum phase variation over one sampling period to π, which induce to a maximum displacement speed of:

$$V_{max} = \frac{\lambda}{4 \cdot T_s} \tag{2.18}$$

Finally, from eq.2.17 we can define the relative mobile mirror position at the time $N \cdot T_s$ as:

$$x(N \cdot T_s) = \sum_{k=0}^{N} \Delta x(k \cdot T_s) \tag{2.19}$$

2.4 The sensor characterization and capabilities

The aim of this section is mainly to evaluate the interferometer in quasi-static conditions or with very small displacements in order to evaluate the noise level at high acquisition frequency and then to estimate the long term performances at lower acquisition frequency. A dynamic condition evaluation using an excited piezoelectric actuator is also presented to demonstrate the sensor subnanometric capabilities.

2.4.1 The experiment setup in static configuration

The interferometer is hardly fixed on a breadboard in front of a mobile mirror which can be tuned for retro-injection. The breadboard is placed on an active table (active piezoelectric system $TS140$ from Table Stable) that isolates from building vibrations with a relatively low bandwidth. The table is placed on a marble which is fixed on a second optical breadboard with four passive feet. The experiment is protected from air flow disturbances with a Plexiglas box covered with a dark sheet to eliminate the light perturbations. There is no active temperature regulation but this parameter is monitored. Fig.2.9 represents a photography of the whole setup.

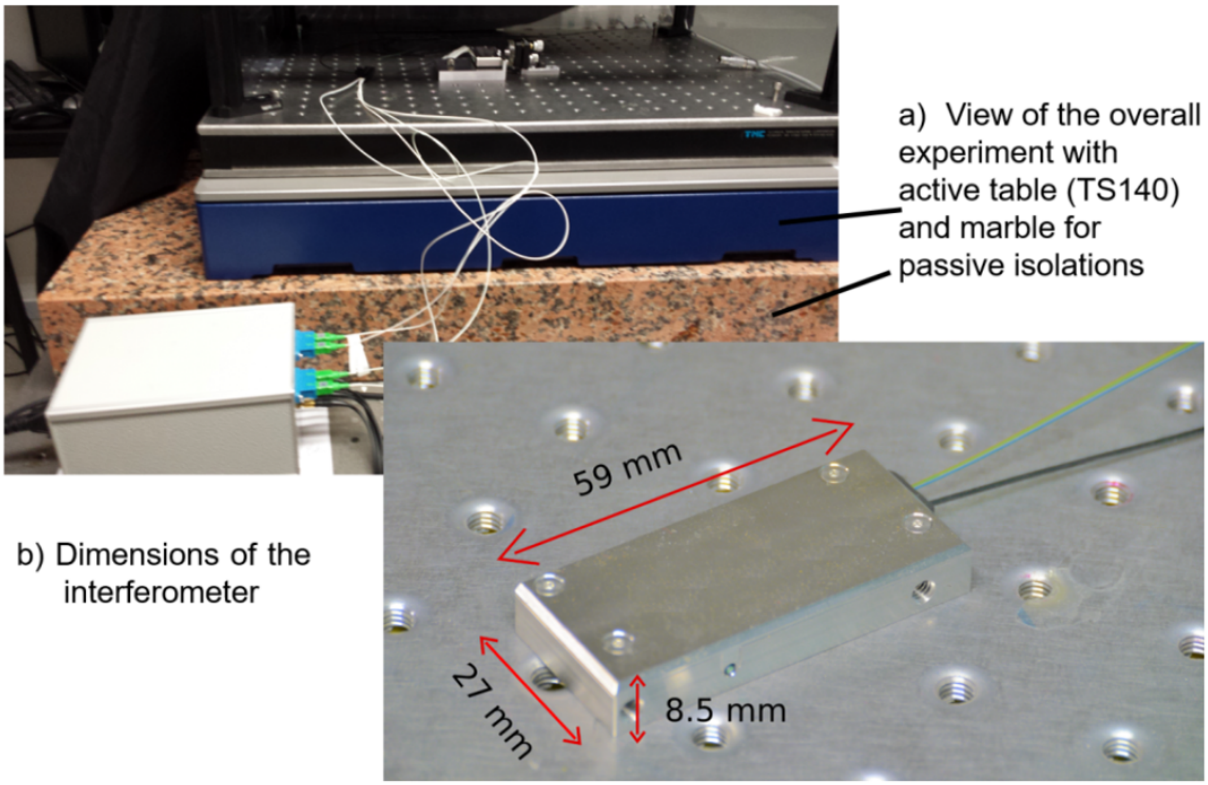

Figure 2.9 Photography of the experiment.

The laser source is a telecom laser module (ORION $Rio0085-1-00-1$) with a wavelength value of $1542,135\,nm$. The source is connected to the interferometer module with an optical fiber and the power can be controlled with a LabVIEW software. The mean power at the output of the optical chip for the useful moving arm is around $140\,\mu W$. The four output signals can be sampled by different systems of Analog-to-Digital Converter boards (ADC). The first system used in our experiment is a 4 channel—fully synchronized—with 24 bits resolution (NI $PCI-4472$) which is a very low noise sample system dedicated to noise sound analysis (with a maximal sampling frequency of $102,4\,kHz$). The second one is a 4 channel—fully synchronized—16 bits resolution (NI $PXI-6143$) with a higher sampling frequency ($250\,kHz$). The four signals are acquired and the position is computed with a LabVIEW software and saved on a computer for a posterior calculus. The calculus includes low-pass filtering, statistical analysis, calibration, and estimation of the ellipse. The sample frequency and parameters of the filters are programmable. The external mobile mirror can be either a simple mirror mounted on tilt mechanical stages for tuning or a mirror mounted on a specific mechanical system. The mechanical stage can be driven with a piezoelectric actuator along the measurement axis.

2.4.2 Static evaluation

Once the experiment is fully operational, the interferometer is tuned by optimizing the retro-injected signal. When the interferometer is correctly tuned, the box is closed and the measurement recorded during a calm period (in general during the night or the week-end in order to minimize the human activity perturbations). The first curves have been made with the 24 bits ADC system. Several distances between the output collimating lens and mobile mirror have been tested. Nominal conditions are $1\,cm$ and $4\,cm$ but several sets of distance have been tested (up to $6\,cm$) and results are very similar. Hereafter, we present results for nominal conditions.

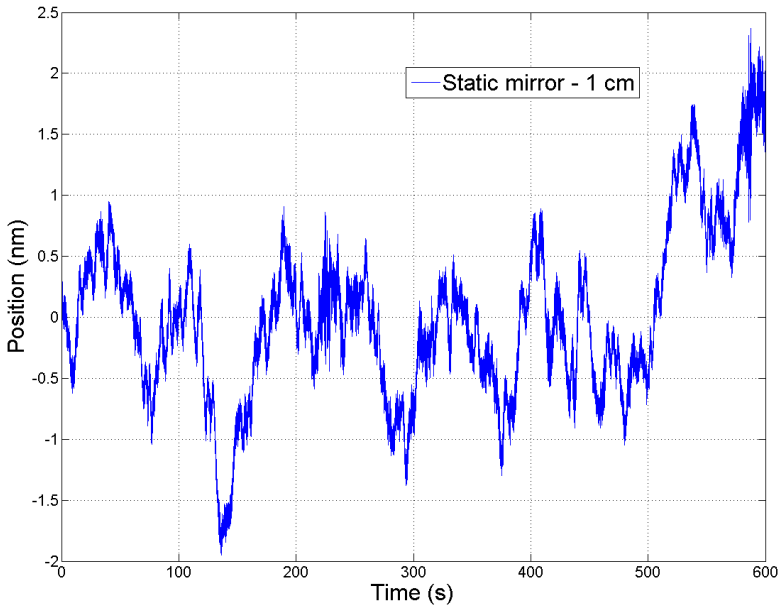

Figure 2.10 Measurements of the relative position of the mirror in a static configuration.

Fig.2.10 shows measurements as a function of time over $10\,min$. The sampling frequency is $30\,kHz$ but a mean is calculated over 10 points to make the figure clearer. Therefore, the plotting frequency is $3\,kHz$. Of course, over $10\,min$, a remaining drift appears and small perturbations of a few nanometers are visible.

It is quite impossible to be fully insensitive to the environment. In order to estimate the potential of the instrument, a differential measurement has been plotted in fig.2.11 The part (a) presents the data with respect to the time. Two working distances have been used and separated on the plot for clarity. The position is updated at a frequency $f_s = 3\,kHz$ (the period $T_s = 1/f_s$ can be modified). After this step, a difference is computed. Each point of the plot is the result of the difference between the mean

position at time t and $t + T_s$. The aim of this differential measurement is to avoid all environmental perturbations and to only measure the limits of the optical chip associated with the instrumentation chain. The bottom curves represent the respective histograms with Gaussian fits.

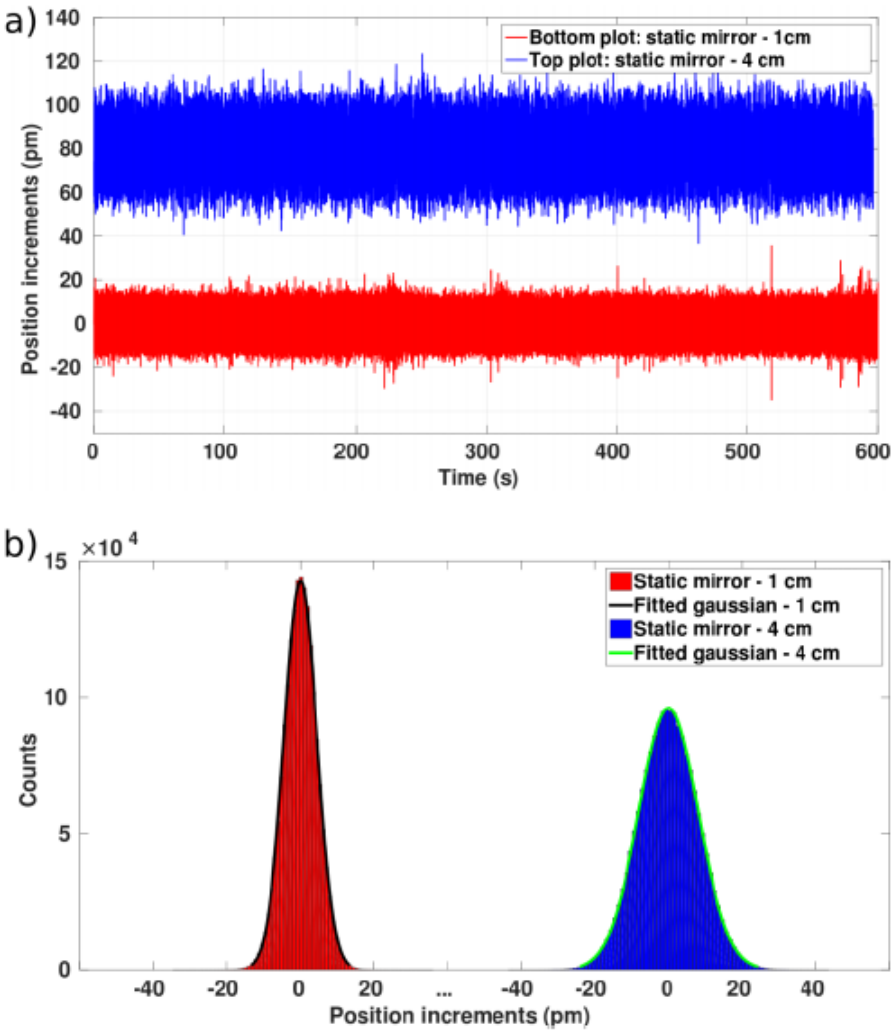

Figure 2.11 Plot of differential measurements. The experiment has been made for two distances (1 cm and 4 cm) and plots have been separated for clarity. (a) is time dependent (b) is the distribution with a Gaussian profile.

One can see that the remaining noise is Gaussian with a standard deviation of 4.5 pm and 8 pm, respectively, for 1 cm and 4 cm working distances. The performances for the working distance of 4 cm are degraded because of the output lens. The beam is collimated for a few centimeters and is slightly diverging for higher distances. Consequently, the retro-injected signal is lower for longer distance as well as the signal to noise ratio. However, the performances are below the nanometer level which makes the interferometer competitive compared to the commercial apparatus. Taking into account the present

output lens, we have made some tests up to 6 cm stroke but it could be enhanced by changing the lens.

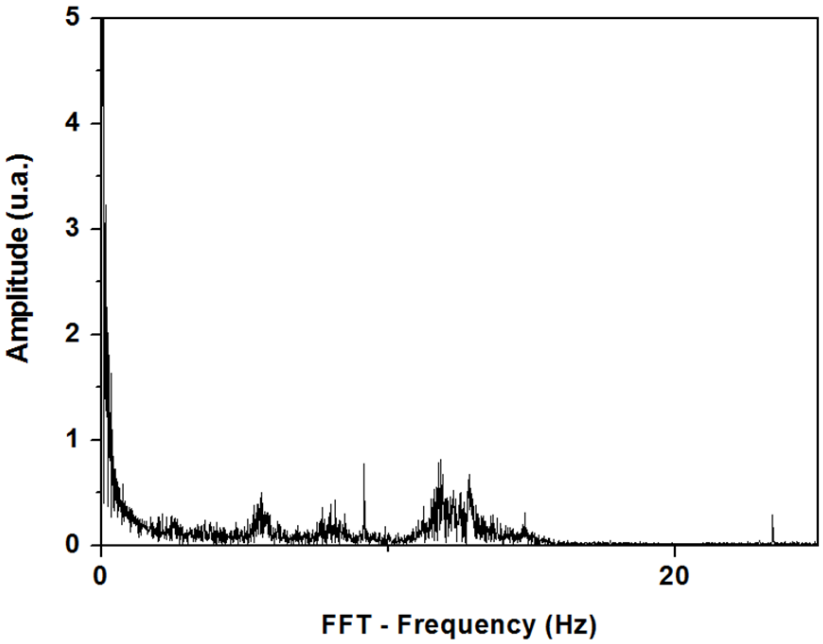

Figure 2.12 Fast Fourier Transform (FFT) of the vibration measurement on the mirror in static configuration.

Fig.2.12 and fig.2.13 represent respectively the Fast Fourier Transform (FFT) and the Power Spectral Density (PSD) of the measurements. The FFT is used as a tool to check that the remaining noise is mainly in the low frequency spectrum range. It is due to the vibrations of the building which are very hard to cancel. The remaining free oscillating frequencies appear around 5 Hz, 9 Hz, and 12 Hz and of course some noise in a very low frequency.

On the PSD plot, the frequency range covered by the measurements is quite large, from 0.01 Hz to 15 kHz. We can see also the noise due to oscillating frequencies of the building around 10 Hz. The PSD noise level is around 400 $fm/\sqrt{Hz}$ @ 100 Hz and converges to the level of $10^{-26}\, m^2/Hz$ @ 10 kHz, which corresponds to 100 $fm/\sqrt{Hz}$ @ 10 kHz.

In complement to the results obtained with an analysis for high frequencies, a long-time estimation has been performed. Several sets of measurements have been recorded, either over short time with 30 kHz sampling frequency or with mid and long term range with 1 kHz and 100 Hz sampling frequencies. The Allan standard deviation σ_y has been estimated for different integration times τ [103]. Note that the residual oscillation noise due to the building environment has not been compensated because it would

have required band-pass filtering and we did not want to suppress the useful information. Fig.2.14 represents the plots of the Allan standard deviation depending on the integration time τ from $3 \cdot 10^{-4}\,s$ to $20\,000\,s$ (one night-long and more).

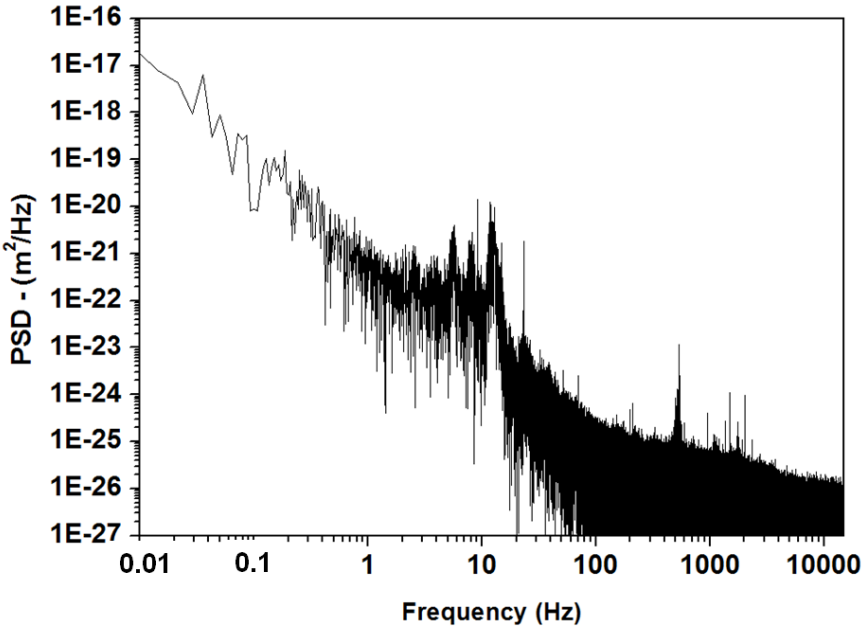

Figure 2.13 Power Spectral Density (PSD) of the vibration measurements on the mirror in static configuration.

For the working distance of $1\,cm$, the very short time estimation of the Allan standard deviation remains mainly below $10\,pm$ and below $1\,nm$ for integration time up to tens of seconds (black square, green triangle, and blue triangle curves). We can see again that the signal to noise ratio is lower and that the measurements can be degraded for a higher working distance. The bump between $10^{-2}\,s$ and $10^{-1}\,s$ corresponds to the remaining noise of the building at a few hertz and the level may depend on the moment when the records are performed. The experiments made for a long duration ($1\,h$-long or more) lead to a drift of several nanometers. This is mainly due to the environmental conditions like the temperature and the mechanical deformations.

In order to estimate the potential of the apparatus, the techniques described in fig.2.11 are used. The differential measurements are calculated to avoid drifts and the Allan standard deviation is plotted. It corresponds to the two bottom curves (blue diamonds and purple triangles). Acquisition has been made either with the 24 bits ADC system or the 16 bits ADC system. The long time estimation ($>1\,h$) seems to converge toward the level of $20\,fm$. It is then likely that the performances could be better for long time integration time with better environmental conditions: vacuum condition

or air conditioning, a better active anti-vibration table, and no residual mechanical oscillations.

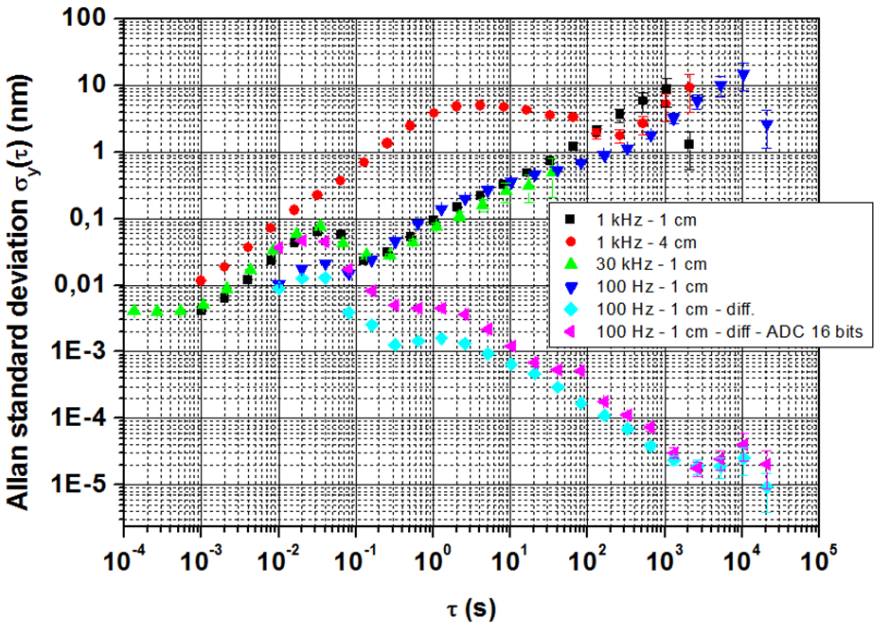

Figure 2.14 Allan standard deviations depending on the integration time.

This system reaches very good performances when noise level is concerned. It is difficult to compare exactly the noise performances between all the systems presented in the literature because, at very low level, the environment is overriding. Nevertheless, power spectral density level reaches typically $20\,pm/\sqrt{Hz}$ @ $100\,Hz$ for strain sensors [50], $1\,pm/\sqrt{Hz}$ @ $100\,Hz$ for capacitive sensors for $10\,\mu m$ stroke or mostly $40\,pm/\sqrt{Hz}$ @ $100\,Hz$ for capacitive sensors for $100\,\mu m$ stroke,1950 $fm/\sqrt{Hz}$ @ $100\,Hz$ for piezoelectric strain sensors for few μm stroke,6 and $10\,pm/\sqrt{Hz}$ @ $100\,Hz$ for integrated thermal position sensors for $100\,\mu m$ stroke [104]. Our sensor, with $400\,fm/\sqrt{Hz}$ @ $100\,Hz$, is thus highly competitive compared to other sensors in terms of noise. Furthermore, these sensors are always dedicated to applications that require a stroke of a few micrometers. They have also a low bandwidth compared to the potential of systems based on the interferometry. For these sensors, the performances can be better for lower frequencies when the interferometry is very sensitive to the environment. It is very difficult to compare the PSD between commercial interferometers but, as far as we know, the noise level is very good. A recent example of closed-loop phase-locked prototype [105] shows noise level around $100\,pm/\sqrt{Hz}$ @ $100\,Hz$ and $100\,fm/\sqrt{Hz}$ @ $10\,kHz$.

In the domain of compact and integrated interferometer, many scientists have

prospected for ultra-high performances. Optical fiber interferometers are highly sensitive to the environment because of the sensitivity of the optical fiber. Fabry-Perot fibered interferometers usually reach few $pm/\sqrt{Hz}$ [106]. The Atomic Force Microscopy (AFM) community has also developed several dedicated interferometers to sense the cantilever and obtained outstanding performances near of the shot noise, few $fm/\sqrt{Hz}$ [107, 108, 109, 110, 111, 112, 113, 114]. Nevertheless, these systems are usually not suitable for applications that require a long stroke [115, 116, 117, 118, 119, 120, 121, 122, 123, 124].

The environmental conditions are also critical for the system behavior and the performances. The interferometer that we have presented was first designed for a seismometer. Experiments were performed in a dedicated deep underground station and $100\,fm/\sqrt{Hz}@8\,Hz$ was reached. However, we did not succeed to reproduce these ideal conditions in our laboratory.

2.4.3 Experiment setup and evaluation in nanometer scale dynamic configuration

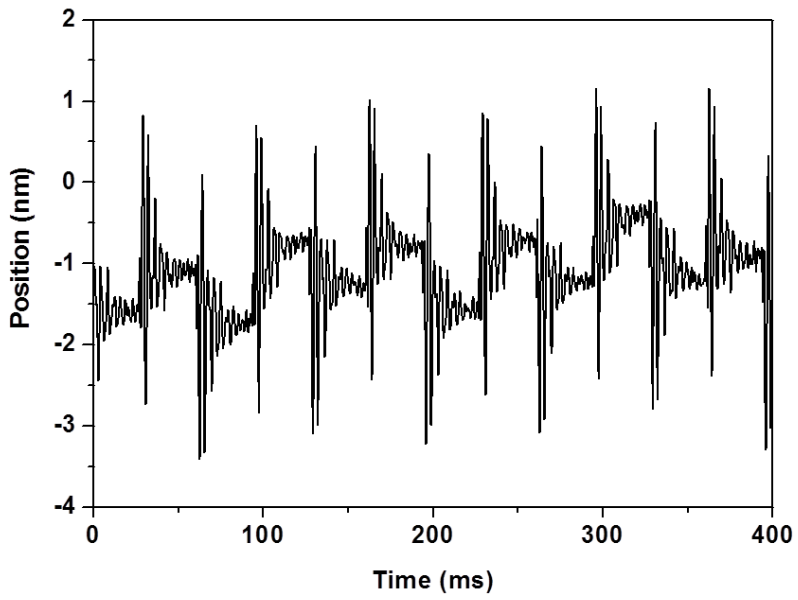

Figure 2.15 Steps of $0,5\,nm$ @ $15\,Hz$ (sample frequency of $30\,kHz$).

The mobile mirror is now driven by a piezoelectric actuator along the axis of the interferometer. The aim of this part is to evaluate the dynamic performances of the whole system. To avoid the natural residual vibration detected before (5, 12, and $9\,Hz$ mainly), the piezoelectric actuator is driven with a square waveform (a frequency of $15\,Hz$ and a magnitude of a few millivolts).

Fig.2.15 shows the results of time measurements with a sampling frequency of $30\,kHz$. We clearly see the steps with an amplitude of $0.5\,nm$. However, the piezoelectric actuator is in an open-loop control mode and the steps are thus very disturbed, with second order oscillations on the front edges.

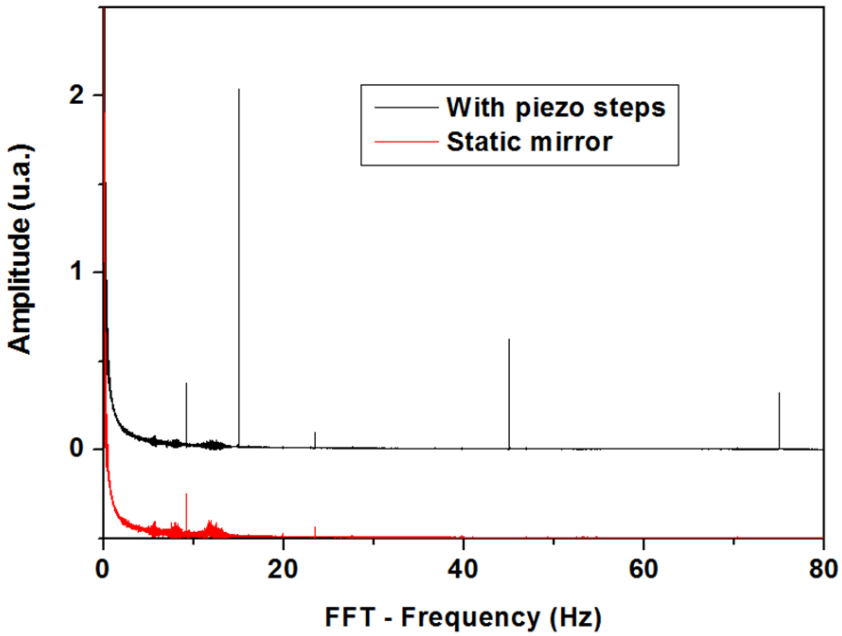

Figure 2.16 FFT without steps (red curve downside) and with the steps (black curve upside).

Fig.2.16 is the FFT view. Two curves have been plotted (separated for clarity). The top one (black) is obtained when the piezoelectric actuator is driven with the waveform. The bottom one is obtained when no signal is applied to the actuator. The free oscillation around $9\,Hz$ is due to the building in both cases. On the top curve, the signal excitation frequency of $15\,Hz$ is present as well as the odd harmonics (45 and $75\,Hz$).

2.4.4 Integration to a positioning system and millimeter range evaluation

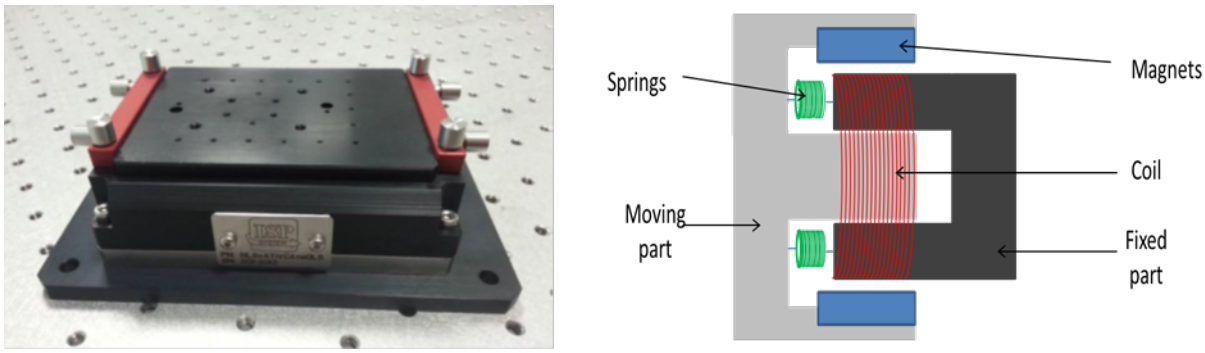

Figure 2.17 The NLS translation stage and the VCM schematic.

The sensor is now combined to a nanopositioning translation stage, NLS series from ISP Systems (fig.2.17). The mobile mirror is fixed on the stage. This one axis linear positioning stage allows horizontal travels with nanometric resolution. The stage is based on a voice coil motor and a flexure guidance. Voice Coil Motors (VCMs) have for main assets the quasi-elimination of the frictions on the guide, the high reachable positioning speed and the association of high resolution with long stroke [125]. ISP System announces a $4\,mm$ travel range for $10\,nm$ dynamic resolution and $10\,mm \cdot s^{-1}$ maximum displacement speed capabilities for this product.

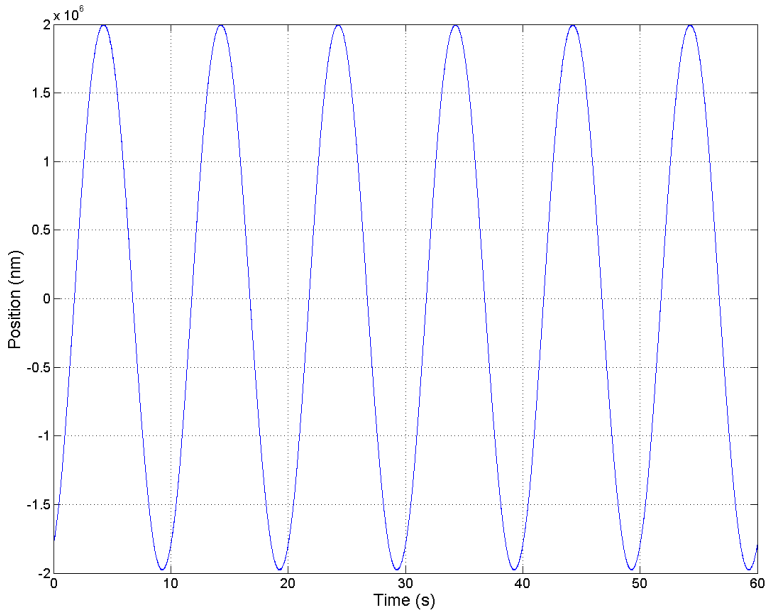

Figure 2.18 Open-loop $2\,mm$ amplitude and $0.1\,Hz$ frequency sinewave displacement realized with the translation stage and measured with the interferometer.

Fig.2.18 demonstrates an open-loop control mode for a sinewave displacement of $2\,mm$ amplitude and $0.1\,Hz$ frequency, realized with the translation stage and measured with the interferometer at a sampling frequency of $50\,kHz$. The full range displacement of the translation stage is properly measured by the interferometer. This demonstrates the long stroke capabilities of the sensor. We will discuss in next chapter the maximum speed which depends on the sample frequency.

Moreover, a PI controller using the sensor position feedback was realized. Fig.2.19 demonstrates a closed-loop $25\,nm$ amplitude steps at a frequency of $1\,Hz$ performed by the translation stage using the interferometer position measurement feedback. A mean standard deviation of $\pm 4\,nm$ on the steps is reached on the positioning system.

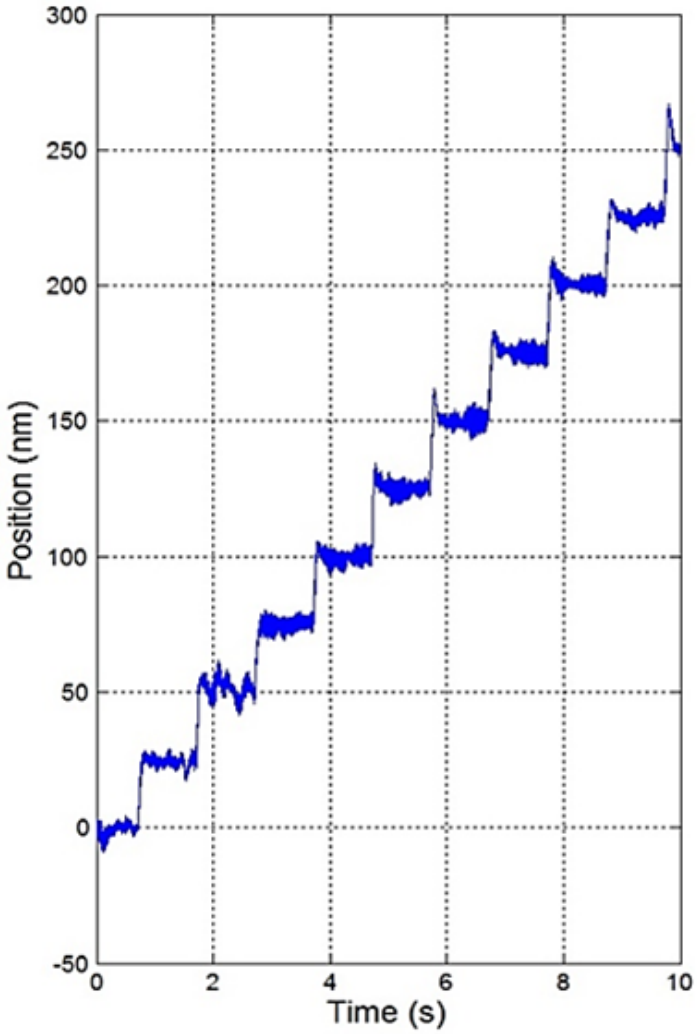

Figure 2.19 Closed-loop 25 nm amplitude steps at 1 Hz performed by the translation stage using the interferometer position measurement feedback.

2.5 Conclusion

In this chapter, the designs of the prototypes that led to a fully embedded optical chip interferometer were described in section 2. Then the functioning principle and the equations that govern the system were presented in section 3. And finally in section 4, the performances and capabilities of this sensor were evaluated in static and dynamic configurations where both low sensitivity to external disturbances and ease of use has been demonstrated.

The presented sensor reaches very good performances when noise level is concerned as demonstrated in the experiments, and is highly competitive compared to other sensors in

terms of noise. Furthermore, combined to a highly stabilized laser source, the PicoMove can achieve long stroke (few cm); its bandwidth is only limited by the acquisition electronics. The main drawback is still the classical one for interferometry, that is likely the high sensitivity to the environment. It will be explored in the next chapter.

Chapter 3

The position computation errors

Contents

3.1 Introduction

This chapter deals with the metrological interferometric measurement specificities and sources of errors, applied to the studied interferometer. The system maximum displacement velocity is demonstrated and its compensation using a parallel coarse position sensing system is highlighted. The sensor robustness to temperature and humidity variations, under controlled environment is shown and discussed.

3.2 The acquisition and position computation

The acquisition system is one of the main concern, when nanometer accuracy interferometry metrological measurement is targeted.

The PicoMove interferometer is associated to a $N\,bits$ acquisition card working at a sample frequency f_s in the range $[0, 5\,V]$. We can define classicaly the resolution acquisition as:

$$\varepsilon = \frac{5}{2^N} \tag{3.1}$$

and then the four acquired outputs signals of the interferometer are expressed:

$$\begin{cases} Ref_1 = r_1 \cdot \varepsilon \pm \varepsilon \\ Mes_1 = m_1 \cdot \varepsilon \pm \varepsilon \\ Mes_2 = m_2 \cdot \varepsilon \pm \varepsilon \\ Ref_2 = r_2 \cdot \varepsilon \pm \varepsilon \end{cases} \tag{3.2}$$

with r_1,m_1,m_2 and r_2 integers, such that an uncertainty of $\pm\varepsilon$ is considered into the four measures (at most $1 - bit$ error).

3.2.1 The position computation resolution

From eq.2.12 and using eq.3.2, the position computation resolution can be defined as the minimum measurable displacement. Simulation was done over all the possible values of $\Delta\alpha^1$ in our experiment conditions. The resolution of the system was defined as the maximum value on $\Delta\alpha^1$ if one bit variation is done on the acquired measurement signals. This value of $\Delta\alpha^1$ appeared when the phase shift between the interferometer arms is around $77.5\,°$, and reach $3.45 \cdot 10^{-7}\,rad$, which corresponds to a displacement resolution of $42.56\,fm$.

With such a low value of resolution, the measurement uncertainty and the environmental condition are of more concern than the acquisition and the computation. Moreover, the computation system is a $64-bits$ system associated to a LabView Real Time $64-bits$ operating system, such that the acquisition and computation system is outperforming, and is no more a concern in the study of the interferometer capabilities.

3.2.2 The calibration influence on the computed position

The calibration parameters uncertainty based on eq.2.8 and eq.2.10 are be expressed as:

$$\begin{cases} \Delta Ks_{1i} = \left|\frac{\delta Ks_{1i}}{\delta Mes_i}\right| \cdot \Delta Mes_i + \left|\frac{\delta Ks_{1i}}{\delta Ref_1}\right| \cdot \Delta Ref_1 = \frac{1+Ks_{1i}}{Ref_1} \cdot \varepsilon = \frac{1+Ks_{1i}}{r_1} \\ \Delta Ks_{2i} = \frac{2+2\cdot Ks_{1i}+Ks_{2i}}{r_2} \end{cases} \tag{3.3}$$

Then the uncertainty on the normalized measurement signals calculated by the same way, and based on eq.2.12 are expressed:

$$\Delta Mes_{i,norm} = \frac{1 + (\frac{1+2\cdot Ks_{1i}}{2\cdot Ks_{1i}\cdot r_1} + \frac{1+Ks_{1i}+Ks_{2i}}{Ks_{2i}\cdot r_2}) \cdot |m_i + Ks_{1i}\cdot r_1 - Ks_{2i}\cdot r_2|}{2\cdot\sqrt{Ks_{1i}\cdot Ks_{2i}\cdot r_1\cdot r_2}} \tag{3.4}$$

First let's assume a perfectly designed interferometer, with two measurement signals perfectly in quadrature ($\alpha_0 = 0$). The phase shift between the interferometer arms and its uncertainty are expressed:

$$\begin{cases} \alpha^1 = arctan2(-Mes_{2,norm}, Mes_{1,norm}) \pm \Delta[\alpha^1] \\ \Delta[\alpha^1] = |Mes_{1,norm}| \cdot \Delta Mes_{2,norm} + |Mes_{2,norm}| \cdot \Delta Mes_{1,norm} \end{cases} \tag{3.5}$$

with $Mes_{2,norm} = -sin(\alpha^1)$ *and* $Mes_{1,norm} = cos(\alpha^1)$,

and using eq.2.17 the uncertainty in the measured displacement, knowing that $\Delta[\Delta\alpha^1] = 2\cdot\Delta[\alpha^1]$ is expressed:

$$\Delta[\Delta X] = \left|\frac{\lambda_0}{2\cdot\pi\cdot n}\right| \cdot \Delta[\alpha^1] + \left|\frac{\Delta\alpha^1}{4\cdot\pi\cdot n}\right| \cdot \Delta\lambda + \left|\frac{\Delta\alpha^1\cdot\lambda_0}{4\cdot\pi\cdot n^2}\right| \cdot \Delta n \tag{3.6}$$

3.2.3 Maximum uncertainty on the measured displacement

This subsection is a numerical application of what was presented before, based on the characteristics of our experiments. Let's assume the nominal Ks_{ij} parameters:

$$\begin{cases} Ks_{11} = 0.74 & Ks_{12} = 0.7 \\ Ks_{21} = 0.7 & Ks_{22} = 0.65 \end{cases}$$

To ensure that the measurement signals stay in the range $[0, 5\,V]$, and taking into account, the fact that the operational amplifiers in the optical transducers at the output of the interferometer, saturate around $4.5\,V$, we chose in our experiments and in this example, to fix the value of the laser source input reference signal to $2\,V$, and we assume $1\,V$ in the retro-injected reference signal, such as:

$$\begin{cases} Mes_1^{min} = 0.14\,V & Mes_1^{max} = 4.22\,V \\ Mes_2^{min} = 0.14\,V & Mes_2^{max} = 3.96\,V \end{cases}.$$

The acquisition system associated to the interferometer is a $24 - bits$ acquisition card $NI\ PCI - 4472$ from National Instruments ($\varepsilon = 2.98 \cdot 10^{-7}\,V$). It is configured in the acquisition range $[0, 5\,V]$ at a sampling frequency of $100\,kHz$. The whole system is controlled by a Labview $64 - bits$ computation system, such that:

$$\begin{cases} \Delta Ks_{11} = 2.59 \cdot 10^{-7} & \Delta Ks_{12} = 2.53 \cdot 10^{-7} \\ \Delta Ks_{21} = 1.25 \cdot 10^{-6} & \Delta Ks_{22} = 1.21 \cdot 10^{-6} \end{cases}$$

Let's say that the mobile mirror is at a position from the chip such that the uncertainty on the phase shift between the interferometer arms is maximal. Then, using ($Mes_{2,norm} = -sin(\alpha^1)$, $Mes_{1,norm} = cos(\alpha^1)$) and eq.3.5 one can write:

$$\Delta[\alpha^1] = \left|cos(\alpha^1)\right| \cdot \Delta Mes_{2,norm} + \left|sin(\alpha^1)\right| \cdot \Delta Mes_{1,norm} \tag{3.7}$$

To find the maximum value of $\Delta[\alpha^1]$ we simulated the whole system in the range $\alpha^1 \epsilon [-\pi, \pi]$ and the uncertainty on this phase shift was computed and ploted in fig.3.1. The observed maximal phase shift uncertainty is for almost $\alpha^1 = -\frac{\pi}{4}$, with an uncertainty in the computation of $\Delta[\alpha^1] = 3.07 \cdot 10^{-6}\,rad$.

Then the contribution of the uncertainty on the phase shift on the measured displacement in static mode, in vacuum condition ($n = 1$) and with a wavelength in the mid-infrared at $1.55\,\mu m$, based on eq.3.6 is:

$$\Delta[\Delta X](\alpha^1) = 757.56\,fm$$

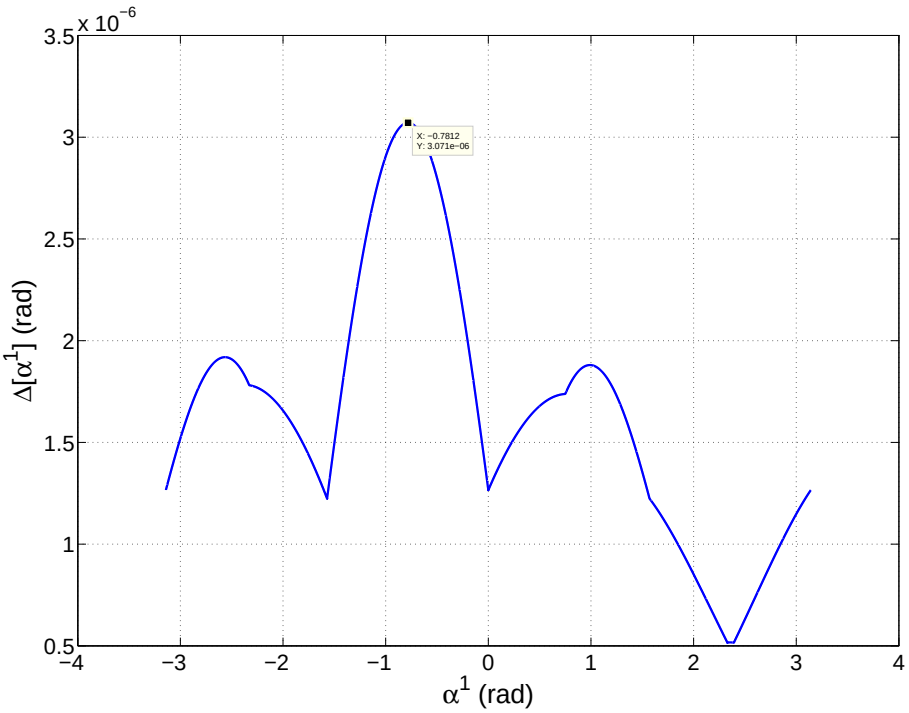

Figure 3.1 Uncertainty on the phase shift between the interferometer arm with respect to the phase shift

3.2.4 Introduction of the count of number of fringes

In the previous subsections a 757.56 fm maximum uncertainty on the displacement was calculated, but if we apply eq.2.19, or even eq.4.2 (with the refractive index correction) to compute the position, we will fall into an uncertainty integration trap. The uncertainty on the computed position will simply be the uncertainty on the displacement multiplied by the number of samples, resulting in long term drift. For example, for a 757.56 fm uncertainty on the whole calculated displacements, 1320 samples are enough to exceed a 1 nm uncertainty on the computed position.

The use of the previously presented computation form of the position is then highly compromised, and the introduction of a new parameter is necessary. The number of turn realized on the ellipse is introduced. The initial phase shift between the arms of the interferometer α_i^1 will be registered, and each time the phase shift α^1 cross this value in a way or the other, the n_t will be incremented/decremented, such that the computed position from eq.2.19 becomes:

$$x(N \cdot T_s) = \frac{\alpha(N \cdot T_s) \cdot \lambda_0}{4 \cdot \pi \cdot n} + n_t \cdot \frac{\lambda_0}{2 \cdot n} \tag{3.8}$$

with N the sample index and T_s the sample period, and combined to the following

algorithm before the computation:

Algorithm 3.1 Phase shift and number of turn computation

$\Delta\alpha^1(N \cdot T_s) = \alpha^1(N \cdot T_s) - \alpha^1((N-1) \cdot T_s)$
while $(|\Delta\alpha^1(N \cdot T_s)| > \pi)$ **do**
  $\Delta\alpha^1(N \cdot T_s) = \Delta\alpha^1(N \cdot T_s) - sign(\Delta\alpha^1(N \cdot T_s)) \cdot 2 \cdot \pi$
end while
$\alpha(N \cdot T_s) = \alpha^1(N \cdot T_s) - \alpha_i^1$
while $(|\alpha(N \cdot T_s)| > \pi)$ **do**
  $\alpha(N \cdot T_s) = \alpha(N \cdot T_s) - sign(\alpha(N \cdot T_s)) \cdot 2 \cdot \pi$
end while
if $(|\alpha(N \cdot T_s) - (\alpha((N-1) \cdot T_s) + \Delta\alpha^1(N \cdot T_s))| > \pi)$ **then**
  $n_t = n_t - sign(\alpha(N \cdot T_s))$
end if

Then with eq.4.2 to correct the refraction index, we just use:

$$x(N \cdot T_s) = \frac{\alpha(k \cdot T_s) \cdot \lambda_0}{4 \cdot \pi \cdot n(k \cdot T_s)} + n_t \cdot \frac{\lambda_0}{2 \cdot n(k \cdot T_s)} \tag{3.9}$$

Such that using eq.3.9, the uncertainty on the computed position becomes:

$$\begin{aligned}\Delta[x(N \cdot T_s)] = &\left|\tfrac{\lambda_0}{4 \cdot \pi \cdot n}\right| \cdot \Delta[\alpha(k \cdot T_s)] + \left|\tfrac{\alpha(k \cdot T_s)}{4 \cdot \pi \cdot n(k \cdot T_s)}\right| \cdot \Delta\lambda + \left|\tfrac{\alpha(k \cdot T_s) \cdot \lambda_0}{4 \cdot \pi \cdot n(k \cdot T_s)^2}\right| \cdot \Delta n(k \cdot T_s) \\ &+ \left|\tfrac{n_t}{2 \cdot n(k \cdot T_s)}\right| \cdot \Delta\lambda + \left|\tfrac{1}{2 \cdot n(k \cdot T_s)^2}\right| \cdot \Delta n(k \cdot T_s)\end{aligned} \tag{3.10}$$

with $\Delta[\alpha(k \cdot T_s)] = 2 \cdot \Delta[\alpha^1]$,

Finally, from this last expression of the uncertainty on the position computation, one can see that we do not use a sum anymore. The uncertainty in the displacement is no more accumulated over time. The contribution of the uncertainty on the phase shift on the position remains then at a maximum value of $757.56\,fm$ over the whole experiment.

3.2.5 The instability of the input-output parameters

Nevertheless, even if the calculated uncertainty on the Ks_{ij} parameters is very low, the experiments showed a sensibility to the environmental conditions (likely the ambient light and temperature among other parameters). From a calibration to an other, the Ks_{ij} seems to vary at the 10^{-3} order over several minutes. In the following, we will consider a worst case uncertainty on these parameters of $\Delta Ks_{ij} = \Delta Ks = 10^{-2}$. The uncertainty on α^1 is calculated again using these new values, assuming that $\Delta Ks_{ij} \gg \varepsilon$ and using:

$$\Delta Mes_{i,norm} = \frac{Ks_{2i} \cdot |m_i + Ks_{1i} \cdot r_1 - Ks_{2i} \cdot r_2| \cdot \Delta Ks_{1i} + Ks_{1i} \cdot |m_i - Ks_{1i} \cdot r_1 + Ks_{2i} \cdot r_2| \cdot \Delta Ks_{2i}}{4 \cdot Ks_{1i} \cdot Ks_{2i} \cdot \sqrt{Ks_{1i} \cdot Ks_{2i} \cdot r_1 \cdot r_2}} \tag{3.11}$$

Fig.3.2 represents the same simulation than realized previously for $\Delta[\alpha^1]$, but using the new assumption on the $Ksij$ parameters uncertainty. The result show that the uncertainty on the phase shift between the interferometer arms is maximal when $\alpha^1 = \pm\frac{\pi}{6}$, with $\Delta[\alpha^1] = 3.95 \cdot 10^{-2}\, rad$.

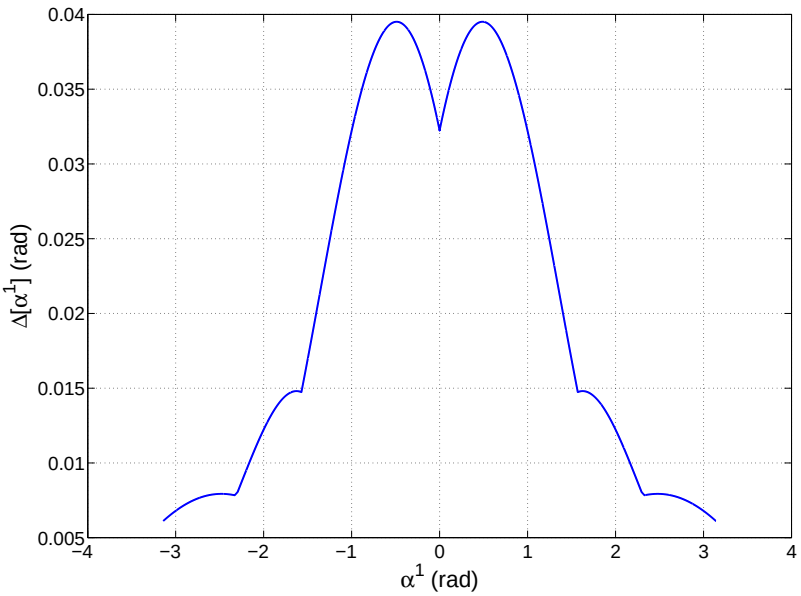

Figure 3.2 Uncertainty on the phase shift between the interferometer arm with respect to the phase shift when $\Delta Ks = 10^{-2}$

Finally, the contribution of the uncertainty on the phase shift on the measured displacement in static mode, in vacuum condition ($n = 1$) and with a wavelength in the mid-infrared at $1.55\,\mu m$, based on eq.3.6 is:

$$\Delta[\Delta X](\alpha^1) = 9.75\, nm$$

3.2.6 The Lissajous ellipse estimation

The previously calculated maximum uncertainty of $9.75\, nm$ is not acceptable when nanometer scale application are targeted. In the purpose to minimize this uncertainty, the Lissajous ellipse was estimated in real time from the normalized measurement signals, and with the assumption $Ks^r_{ij} = Ks_{ij} + \Delta Ks_{ij}$, where Ks_{ij} are the measured input output parameters and Ks^r_{ij} are the real parameters, such as:

$$\begin{cases} cos(\alpha^1) = \frac{2 \cdot Mes_{1,norm} \cdot \sqrt{Ks_{11} \cdot Ks_{21} \cdot r_1 \cdot r_2} - (\Delta Ks_{11} \cdot r_1 + \Delta Ks_{21} \cdot r_2)}{2 \cdot \sqrt{Ks^r_{11} \cdot Ks^r_{21} \cdot r_1 \cdot r_2}} = a \cdot Mes_{1,norm} + x_0 \\ sin(\alpha^1 + \alpha_0) = \frac{-2 \cdot Mes_{2,norm} \cdot \sqrt{Ks_{12} \cdot Ks_{22} \cdot r_1 \cdot r_2} + (\Delta Ks_{12} \cdot r_1 + \Delta Ks_{22} \cdot r_2)}{2 \cdot \sqrt{Ks^r_{12} \cdot Ks^r_{22} \cdot r_1 \cdot r_2}} = b \cdot Mes_{2,norm} + y_0 \end{cases} \tag{3.12}$$

and using eq.2.15 and the propriety $cos(\alpha^1)^2 + sin(\alpha^1)^2 = 1$, we can write with $x = Mes_{1,norm}$ and $y = Mes_{2,norm}$:

$$a_1 \cdot x^2 + a_2 \cdot y^2 + 2 \cdot a_3 \cdot x \cdot y + 2 \cdot a_4 \cdot x + 2 \cdot a_5 \cdot y + a_6 = 0 \tag{3.13}$$

with

- $a_1 = \frac{1}{a^2}$
- $a_2 = \frac{1}{b^2}$
- $a_3 = -\frac{sin(\alpha_0)}{a \cdot b}$
- $a_4 = \frac{1}{a} \cdot (\frac{y_0}{b} \cdot sin(\alpha_0) - \frac{x_0}{a})$
- $a_5 = \frac{1}{b} \cdot (\frac{x_0}{a} \cdot sin(\alpha_0) - \frac{y_0}{b})$
- $a_6 = \frac{x_0^2}{a^2} + \frac{y_0^2}{b^2} - \frac{2 \cdot x_0 \cdot y_0}{a \cdot b} \cdot sin(\alpha_0) - cos^2(\alpha_0)$

and by normalizing eq.3.13 by a_6:

$$c_1 \cdot x^2 + c_2 \cdot y^2 + 2 \cdot c_3 \cdot x \cdot y + 2 \cdot c_4 \cdot x + 2 \cdot c_5 \cdot y = 1 \tag{3.14}$$

This normalization is allowed because a_6 is close to 1 thanks to the calibration realized with the measured Ks_{ij} parameters ($a \simeq 1$,$b \simeq 1$,$x_0 \simeq 0$,$y_0 \simeq 0$,$\alpha_0 \simeq 0$). Eq.3.14 can also be rewrited in its matrix form:

$$V^T \cdot C \cdot V = 0 \tag{3.15}$$

with $C = \begin{pmatrix} c_1 & c_3 & c_4 \\ c_3 & c_2 & c_5 \\ c_4 & c_5 & -1 \end{pmatrix}$ and $V = \begin{pmatrix} x \\ y \\ 1 \end{pmatrix}$.

Eq.3.14 has the form of the general conic section equation. In general, this well known system is resolved with a least-squares fitting, however, a simple conic residual method may render a hyperbola or other non-ellipse conics if the elliptical data are only partially known. The results of these kind of algorithms depend on the constraint imposed on the equation parameters coefficients. For example, the constraints used to fit ellipses in quadrature laser interferometers are often linear, such as $a_1 = 1$ [102] and $a_6 = -1$ [126], or quadratic $\|r\| = 1$ (radius) [127]. A more enhanced method is presented in [128]. This method is based on the work of Harker *et al.* [129] on the fitting

of the conic section equation. The constraints in this method are based on the studies of Fitzgibbon *et al.* [130], Fitzgibbon *et al.* proposed the constraints:

$$\begin{cases} det(A) \neq 0 \\ det\,(A_2) > 0 \\ (a_1 + a_2) \cdot det(A) < 0 \end{cases} \tag{3.16}$$

with $A = \begin{pmatrix} a_1 & a_3 & a_4 \\ a_3 & a_2 & a_5 \\ a_4 & a_5 & a_6 \end{pmatrix}$ and $A_2 = \begin{pmatrix} a_1 & a_3 \\ a_3 & a_2 \end{pmatrix}$.

Actually, eq.3.16 are the conditions that makes the conic section equation describe a real ellipse.

Several fitting methods are used to resolve, and determine the Lissajous ellipse parameters. However, the algorithm described in [131] remains the more robust one, it simply consists on reading the extremes of both axis at each crossing ($\alpha^1 = \frac{N \cdot \pi}{2}$), then compute and correct the ellipse parameters, and lack of quadrature α_0. In our experiment, we chose to use this algorithm to avoid the high number of operations due to the least-square methods that may reduce our sampling frequency. We define (a, b) the amplitudes of the sinusoids described by the normalized measurement signals and (x_0, y_0) the center of the Lissajous ellipse, then we compute the quadrature imperfection as described in subsection 2.3.2.

The main force of this algorithm is the graphical aspect. But it has a non negligible drawback that is the necessity of displacement, because if we are in static mode the data will stay only in slight portion of the ellipse, and the algorithm will never read the new extremes of the normalized measurement signals. Nevertheless, the other algorithms are also not able to fit the ellipse parameters with data that describe a slight arc. Actually, the most capable algorithm is the one presented by Harker *et al.*, and they clearly specify that at least a quarter of the ellipse must be described by the data. Indeed, Pozar *et al.* tested some algorithms to fit an ellipse using a quarter arc of it, and Harker algorithm was the closest with a fitting uncertainty of 10^{-2}.

Note that the estimated parameters with this algorithm (a,b,x_0,y_0), remains very close to a circle parameters (1,1,0,0). The point is just to slightly adjust the normalized measurement signals to overcome the Ks_{ij} parameters lack of stability.

3.2.7 Maximum measurable velocity

Another parameter to consider is the maximum acceptable velocity for the mobile mirror. This parameter is highly correlated to the sample frequency f_s. The measured displacement between two samples is expressed with eq.2.17. This displacement is directly proportional to the measured phase shift $\Delta\alpha^1$, and the mobile mirror velocity can be expressed with respect to the phase shift as:

$$V = \frac{\Delta\alpha^1 \cdot \lambda_0 \cdot f_s}{4 \cdot \pi \cdot n} \tag{3.17}$$

However, in the case where the mobile mirror move at a constant speed V, the measurement signals describe sinewaves of f frequency proportional to the mirror velocity, also proportional to the phase shift, with:

$$f = \frac{\Delta\alpha^1 \cdot f_s}{2 \cdot \pi} = \frac{2 \cdot n}{\lambda_0} \cdot V \tag{3.18}$$

To respect Nyquist–Shannon sampling theorem ($f < \frac{f_s}{2}$), we have to impose a constraint on the phase shift, such that $\Delta\alpha^1 < \pi$, and on the mobile mirror displacement speed in the control part:

$$V < \frac{\lambda_0 \cdot f_s}{4 \cdot n} \tag{3.19}$$

Anyway, in our experiment, the maximum velocity of the translation stage that we use is of $10\,mm/s$. To be able to compute correctly the position of the mobile mirror at maximum displacement speed, the theoretical sampling frequency should be at least at $26.67\,kHz$, in vacuum condition ($n = 1$). Then to ensure the respect of the Nyquist–Shannon criterion, we chose to work at a sampling frequency of $50\,kHz$.

Achieving high velocity measurement by correction of the interferometer measured position

Although interferometer measurements are velocity limited by the acquisition system sampling frequency, it is still possible for the system to operate in high velocity conditions, if a second sensing system with coarse resolution but high dynamic capabilities is combined with the interferometer. This second sensor is used to compensate the interferometer missed fringes due to the high displacement velocity of the mobile mirror.

This technique evident and used in the case of the experiment presented in subsection 4.4.2. The interferometer is combined to a poor resolution but high dynamic

optical encoder, to measure the displacement of a mobile mirror.

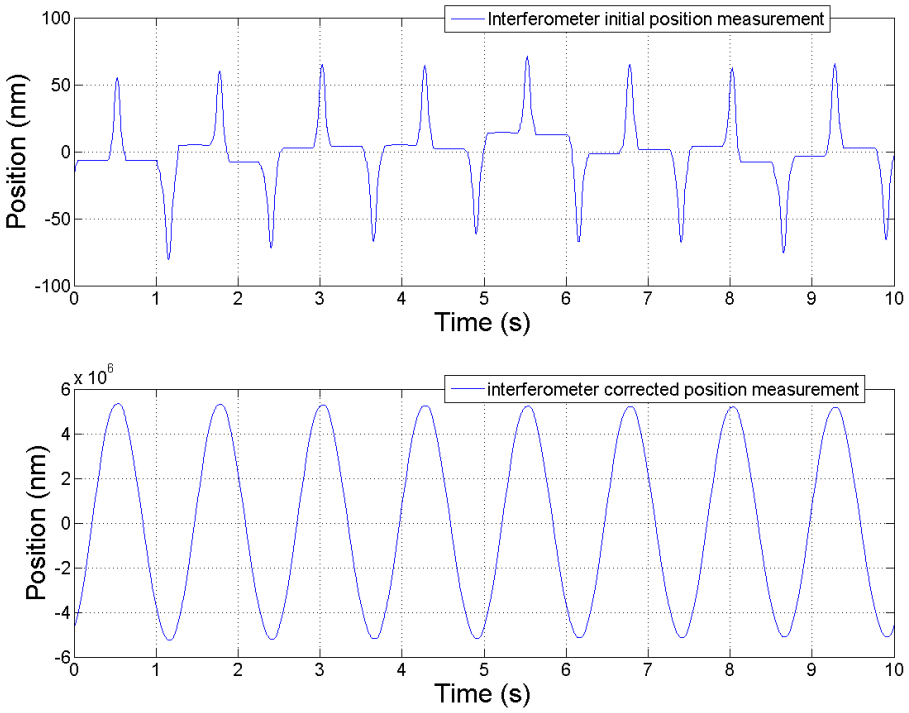

Figure 3.3 Demonstration of the interferometer position measurement correction for the sinusoidal excitation at $0.8\,Hz$.

To correct the interferometer position measurement using the optical encoder, one needs to know the measured velocity or the instantaneous measured displacement. Indeed, when the displacement velocity is too high the interferometer position computation algorithm may miss one or several elliptical rounds (one elliptical round is equivalent to a half-wavelength displacement), then to correct the interferometer measured position, the instantaneous displacement seen by both sensors must be compared. First the instantaneous displacement seen by the optical encoder is computed ($\triangle P_e(i) = P_e(i) - P_e(i-1)$), then it is compared to the interferometer measured displacement. The interferometer measured position is corrected with the following algorithm:

Algorithm 3.2 The interferometer position measurement correction toward high velocity displacement

1: **for** $(i = 2 : max(size(P_i)))$ **do**
2: **while** $(abs(\triangle P_e(i) - \triangle P_i(i)) > \frac{\lambda}{4})$ **do**
3: $\triangle P_i(i) = \triangle P_i(i) + sign(\triangle P_e(i) - \triangle P_i(i)) \cdot \frac{\lambda}{2}$
4: **end while**
5:
6: **end for**

In this algorithm, we choose to take as condition a difference between the two displacement of more than a quarter of wavelength, to add a half wavelength in the direction of the displacement (missed fringe).

The fig.3.3 demonstrates the measured position by the interferometer before and after correction for an example velocity up to $25\,mm/s$.

3.3 The misalignment errors

The misalignment is one of the most important error source in interferometry. Several works and research were realized over years of study, to minimize the misalignment errors on the interferometric measurements. The studied interferometer is meant to be integrated in a X-Y double-axis system, using a polished zerodur cubic mirror of $2\,cm$ side, where the angles of $90\,^\circ$ were ensured after polishing with a tolerance of $1\,arcsec$ ($4.8\,\mu rad$), to reflect laser beams from two interferometers (an interferometer for each axis). Two tilt stages are associated to the cubic mirror, as well as a rotation stage to ensure the alignment of the mirror axis with the X-Y translation stage axis. In the interferometer side, a tilt stage and a rotation stage for each interferometer are also used to ensure the superposition of the measurement axis with the mirror axis (see fig.3.4).

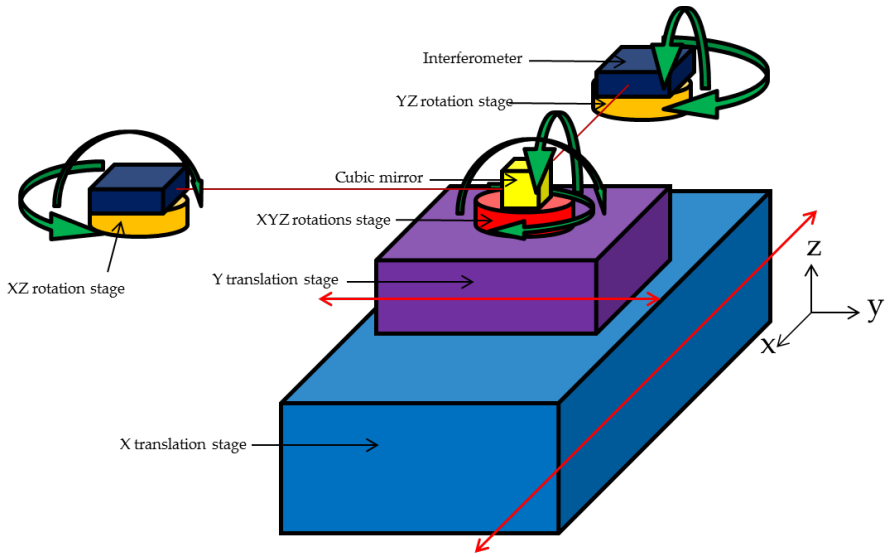

Figure 3.4 The double axis system experiment setup

The aim is to realize X-Y positioning system[132]. One of the main concern is to ensure the orthogonality and the superposition of the measurement axis, the mirror axis and the translation axis, to be able to consider during the experiment a X-Y cartesian coordinate system, and work on a X-Y plane.

3.3.1 The cosine error

The most common misalignment error in interferometry is the cosine error. It is the result of a tilt misalignment angle between the mirror axis and the optical axis (interferometer axis), or the translation axis and the optical axis. For simplicity, we will consider in what follow a perfect alignment between the translation axis and the mirror axis, and a θ misalignment tilt angle between the mirror axis and the optical axis (see fig.3.5). This misalignment angle induces the well known cosine error, and the measured displacement by the interferometer can be expressed:

$$D = \frac{D_r}{cos(\theta)} \tag{3.20}$$

Where D_r is the real realized displacement.

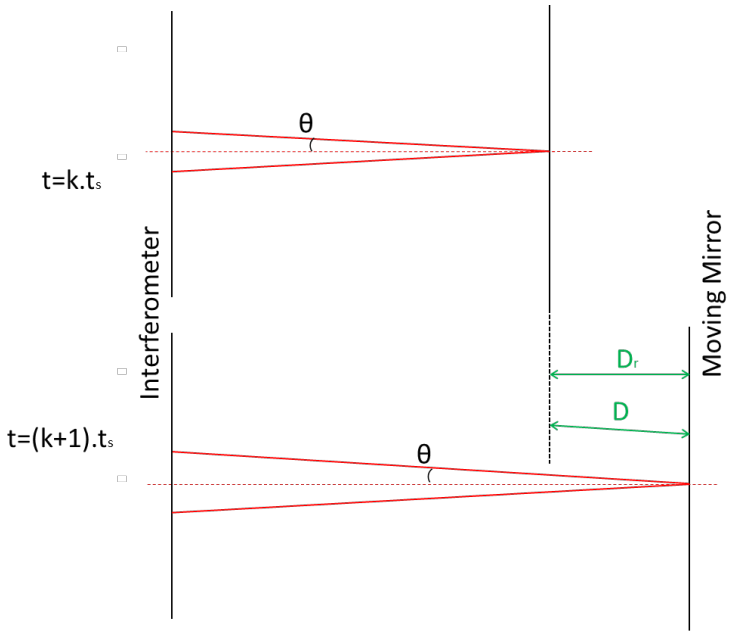

Figure 3.5 Demonstration of the cosine error between two consecutive acquisition

In our system the cosine error is minimized by the maximization of the retro-injected signal Ref_2.

The cosine error estimation

From eq.3.20 the cosine error can be estimated as:

$$\xi = \frac{D - D_r}{D} = 1 - cos(\theta) = \frac{\theta^2}{2} \tag{3.21}$$

The used ISP NLSx series translation stage [133] has a $4\,mm$ stroke ($\pm 2\,mm$), so to ensure a $1\,nm$ maximum error, for instance, a $2.5 \cdot 10^{-7}$ relative error must be reached. And then, the θ angle must be corrected to be at most at $0.7\,mrad$.

3.3.2 The positioning of the cubic mirror

The first step for tuning the double axis system goes by the high accuracy positioning of the mobile mirror. The most common technique to ensure the alignment of the mirror axis with the translation axis is the minimization of the measured displacement on the Y and Z axis while a displacement is imposed on the X axis. Of course, to maximize the tuning resolution the whole displacement range is used in this approach, because the higher the realized displacement is, the higher the measured displacement on the other axis is, which maximize the tuning resolution (the slightest misalignment angle can be measured).

In theory, for a perfect translation stage and cubic mirror the good positioning of the cubic mirror induces null displacement measured on the Y and Z axis. The used translation stage is a Voice Coil Motor with flexure structures guidance based system. It has the advantage to reach high speed for long stroke high resolution positioning by minimizing the frictions (the table is free and is only in touch with the system guidance in four points), but in return, the stage is highly sensitive to the environment and is mainly in constant vibration. This make it very troublesome when positioning the cubic mirror by minimizing the displacement in the Y-Z plan, because, to distinguish the displacement due to the misalignment from the one due to the system vibration it is a challenge.

Nevertheless, the positioning of the cubic mirror is not the only concern. A good alignment between the mirror axis (X_m,Y_m) and the translation axis (X_p,Y_p) is wished, but a slight misalignment can be tolerated. Once the experiment is launched the working axis are the optical axis (X_s,Y_s) (interferometers axis) and the origins of the working cartesian coordinate system are the initial positions of the mobile mirror. If a (x_c ,y_c) position is aimed, and a displacement on X is necessary to reach this position, the parasite displacement on Y can still be corrected by dual lock-in systems on both axis (X,Y). In someway, as far as the alignment between the mobile mirror and the sensors is ensured, one can consider that the measured positions in the X-Y plan remain correct, what ever mechanical or alignment errors may affect the translation stage.

3.3.3 Abbe error

The Abbe error was described for the first time by Abbe in 1890. The classical definition of Abbe principle[67] is:

- In a displacement measurement the reference should be in line with the displacement to be measured or on its extension.

- In the case when the reference is not in line with the displacement to be measured but parallel to it the distance between these parallel lines is called Abbe offset r.

- In the case of complying with the Abbe principle the angular motion error of the measuring device will cause only a second order error in measurements, which is usually negligible small. On the opposite, when it does not comply with the Abbe principle, in which the Abbe offset $r \neq 0$, a first order error $\delta = r \cdot \Delta\varphi$ will be caused. This error is called Abbe error.

In our experiment, one can assume that we can be free from the first order Abbe error, if we put each mirror face at the center of the translation axis, then the optical axis at this same point. In theory, this should insure a superposition of the X-Y axis of the translation stage, the cubic mirror and the optical axis, such that no Abbe offset exist on the X-Y plan, and only remains the Abbe offset on the Z axis. So the first order Abbe error will only exist for parasite rotations around X or Y.

Several techniques to compensate the Abbe error exist, like the geometry of the system developed by Ducourtieux and Poyet[66]. However, the most classical technique is to use two parallel interferometers on the same mirror face (X face) separated by a known distance d (with respect to the Y axis) to measure a rotation around X (see fig.3.6) with:

$$tan(\varphi) = \frac{D_2 - D_1}{d} \tag{3.22}$$

With D_i the measured displacement by the interferometer i, in eq.3.22 the interferometer 2 is considered at the right of the interferometer 1, in the case where we use the X face to measure a rotation around Z, with respects to the trigonometric rotation sign.

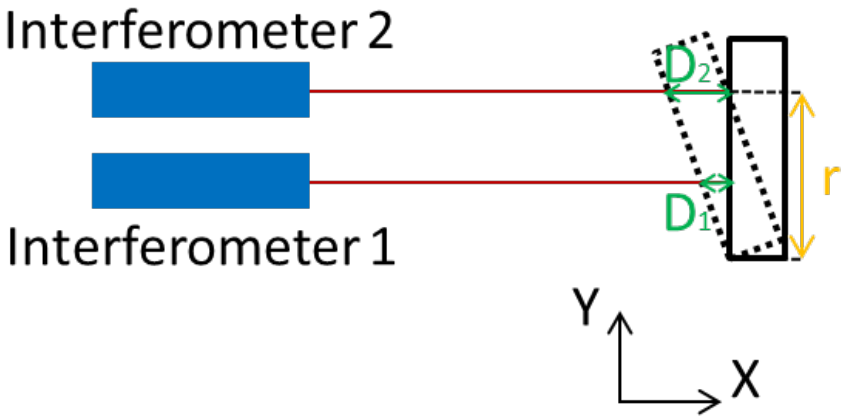

Figure 3.6 Demonstration of the Abbe error.

If the purpose is to measure the position of the center of the cubic mirror, the user need to position the two interferometer at a symmetric distance from the center $\frac{d}{2}$, and the displacement of the center of the cubic mirror on the X axis (for example) become the mean measured displacement:

$$D_x = \frac{D_1 + D_2}{2} \tag{3.23}$$

3.4 The sensitivity to the refractive index

The main drawback to the use of interferometers in high accuracy positioning measurements is their sensitivity to the environmental conditions. Indeed, the inferometry is based on the variation of the measurement arm path length relatively to the reference arm path length. Given that the wavelength is directly dependent of the wave propagation environment and more particularly of the ambient refractivity, one can tell that interferometry measurements are highly sensitive to the refractive index variations.

Fig.3.7 represents two successive states of the optical wave propagation with two successive refractive indexes and so wavelengths, in static configuration. The purpose of this figure is to demonstrate the change in wavelength induced by the variation of the refractive index. Considering the two represented consecutive states over one sampling period, the measured displacement by the interferometer based on eq.2.17 (see chapter 2), would be:

$$\Delta x = \frac{\Delta\alpha^1 \cdot \lambda_2}{4 \cdot \pi} = (\frac{L}{\lambda_2} - \frac{L}{\lambda_1}) \cdot \lambda_2 = L \cdot \frac{n_2 - n_1}{n_2} \tag{3.24}$$

With L the free optical path length.

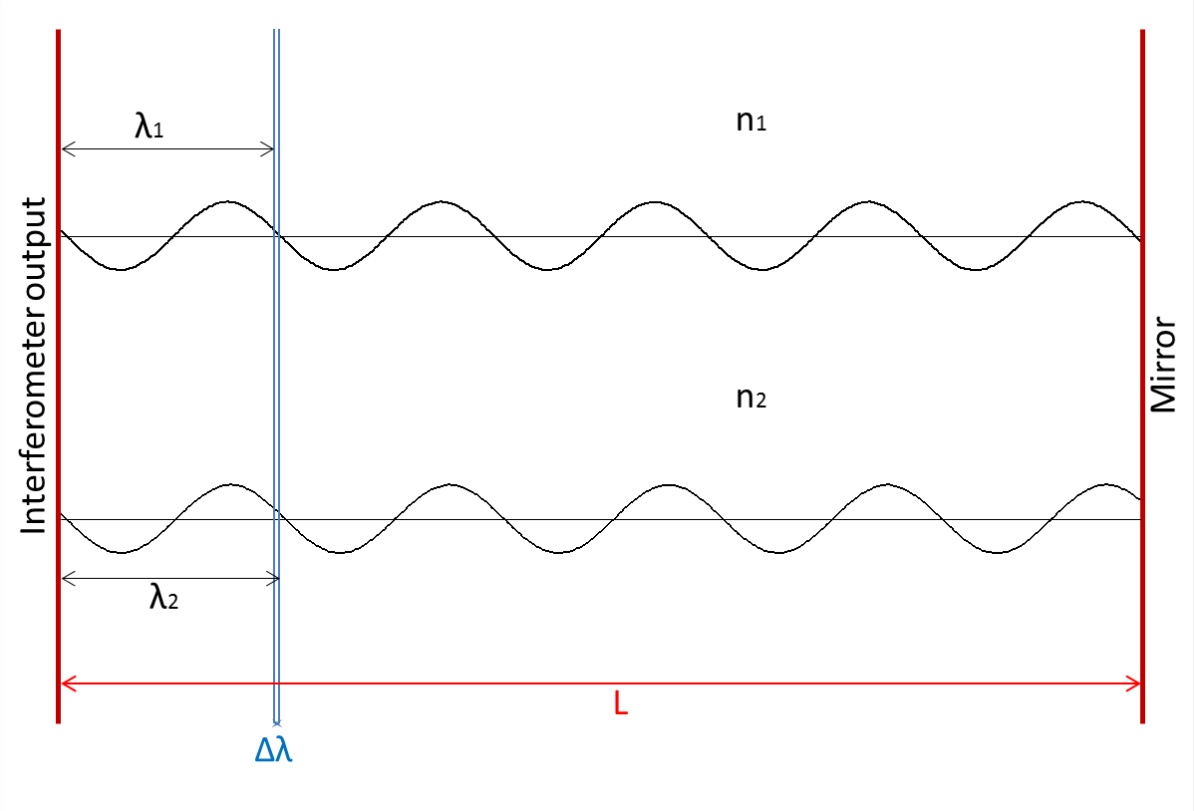

Figure 3.7 Schematic of an optical laser beam, goes from the interferometer to the mobile mirror in a static configuration at two successive instants with two different refractive indexes

But because we are in static mode, Δx must be equal to zero, which make us come to the compensation of eq.2.17 as follow:

$$\Delta x = \frac{\Delta\alpha^1 \cdot \lambda_0}{4 \cdot \pi \cdot n_2} - L \cdot \frac{n_2 - n_1}{n_2} \tag{3.25}$$

λ_0 is the wavelength in vacuum.

3.4.1 The refractive index

The refractive index is a linear function of the ambient temperature, pressure, relative humidity and CO_2 concentration over moderate variations from the initial conditions. In our experiments we used a weather card developed at our laboratory to calculate the refractive index using Edlén formula [70]. The weather card is composed of a temperature sensor $PT1000$, a pressure sensor $SSCDANN030PAAA5$ and a humidity sensor $HIH-4010$, the CO_2 concentration is not measured because it's influence on the refractive index is negligible compared to the other parameters[70]. The influence of the temperature, pressure and humidity on the refractive index was simulated thanks

to the modified Edlén formula for a middle infra-red wavelength of $1.55\,\mu m$ [134], and are presented in tab.3.1.

Table 3.1 Influence of the temperature, pressure and humidity on the refractive index

Parameter	Influence on the refractive index
Temperature	$9.46 \cdot 10^{-7}/°K$
Pressure	$2.65 \cdot 10^{-9}/Pa$
Humidity	$8.68 \cdot 10^{-9}/1\,\%$

The temperature is measured with a maximal standard deviation of $0.3\,°C$, for the pressure sensor the standard deviation is $200\,Pa$, and $3.5\,\%$ for the humidity sensor. Finally, the refractive index is calculated with an uncertainty of 10^{-6}. This uncertainty on the refractive index is not enough when the objective is to achieve nanometer positioning measures. However, we used this card in our experiments to have the information on the refractive index.

3.4.2 The sensitivity to the temperature

Figure 3.8 The LISV thermal enclosure.

To determine the sensitivity of the interferometer toward the temperature, an experiment under controlled environment was done (see fig.3.9). A mirror was fixed in

front of an interferometer, and inside a thermal enclosure capable to realize variation of temperature in the range $[-45, 180]\,°C$, and of humidity in the range $10 - 98\,\%$ (the pressure, humidity, temperature and refractive index are measured with the weather card, that is fixed inside the enclosure, see fig.3.8). The laser source remains outside of the enclosure.

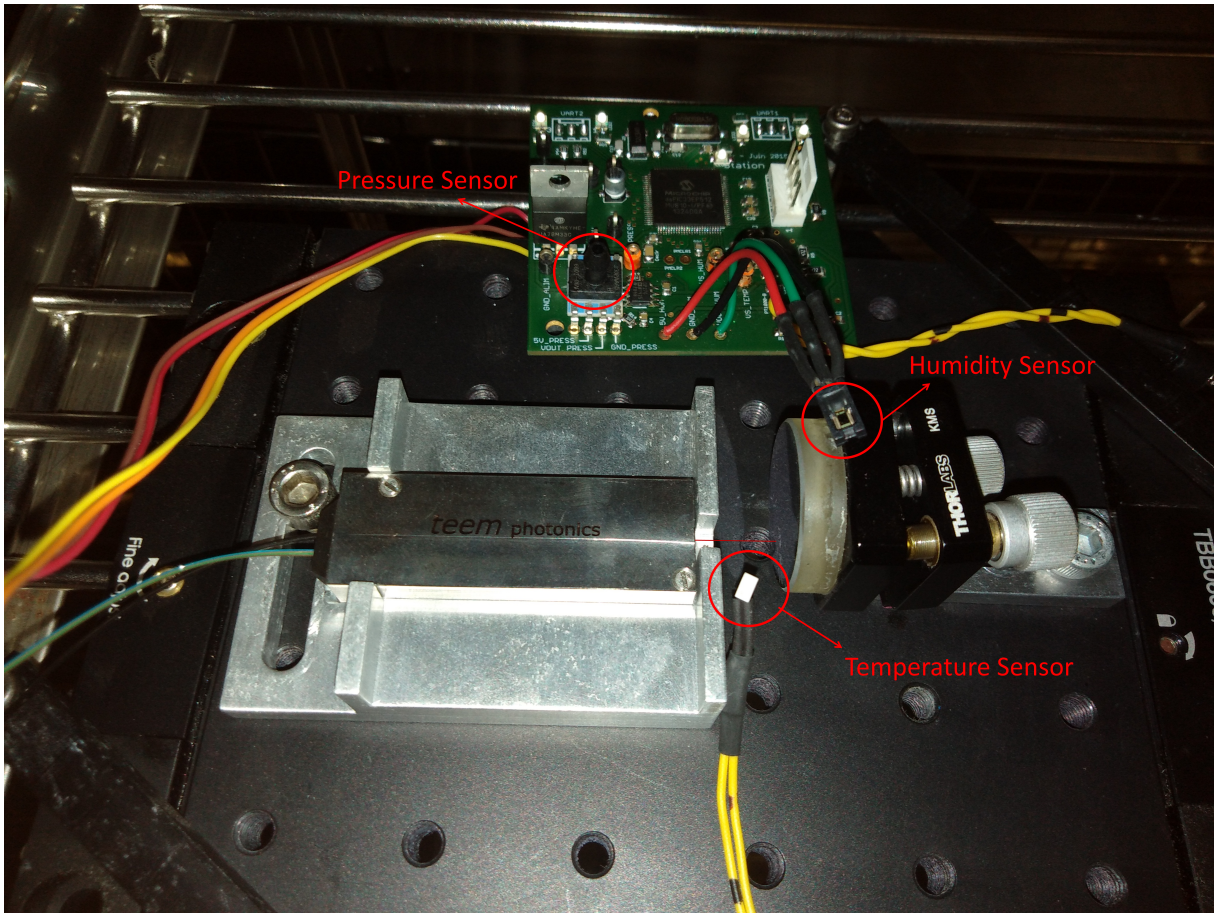

Figure 3.9 Picture of the experiment setup.

The interferometer is calibrated under different humidity and temperature conditions (temperature in the range $[15, 35]\,°C$ and humidity in $30 - 70\,\%$) to demonstrate its robustness to environmental conditions. Fig.3.10 demonstrates that the interferometer Ks input/output parameters variation under different temperature and humidity conditions remains less than $1\,\%$.

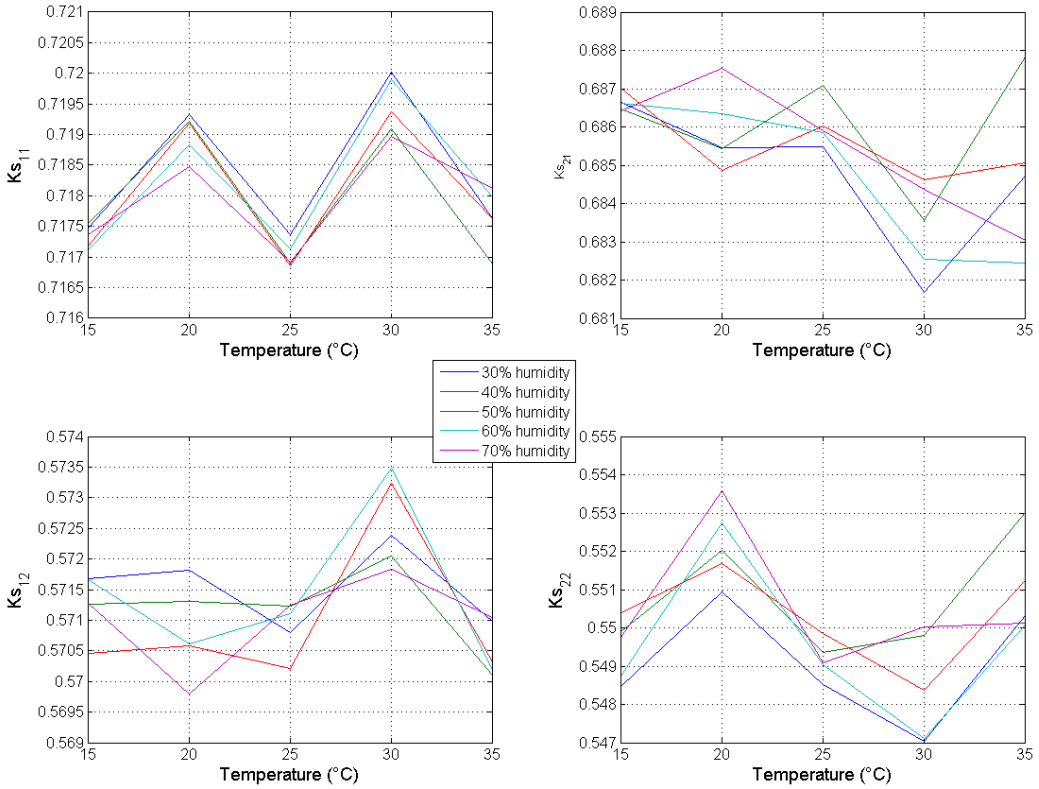

Figure 3.10 The computed interferometer Ks input/output parameters through calibration and under different temperature and humidity conditions.

Tab.3.2 lists the computed mean values and maximum deviations on the obtained interferometer Ks input/output parameters.

Table 3.2 The computed mean values and maximum deviations on the obtained interferometer Ks input/output parameters.

Input/Output parameter	Mean value	Maximum deviation
Ks_{11}	0.7181	0.0019
Ks_{12}	0.5712	0.0022
Ks_{21}	0.6853	0.0036
Ks_{22}	0.5500	0.0035

The influence of those parameters on the position can be estimated using eq.3.10 and eq.3.11. Fig.3.11 demonstrate the uncertainty on the measured displacement which depend on the uncertainty on Ks parameters and also on the phase (modulo $2 \cdot \pi$).

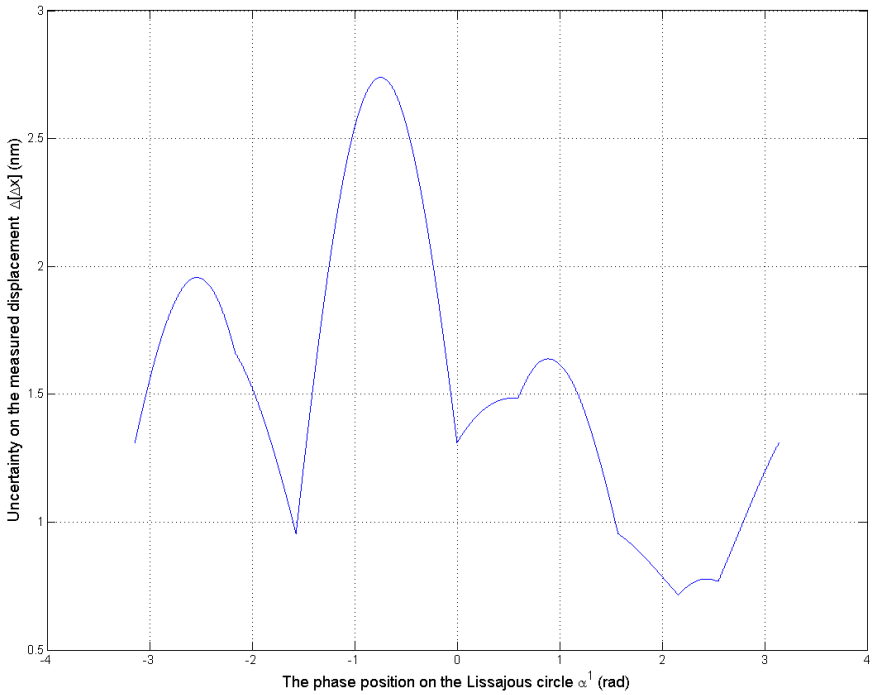

Figure 3.11 Uncertainty on the measured displacement with respect to the phase position on the Lissajous circle.

The maximum uncertainty on the measured displacement ($2.74\,nm$) occurs for a phase of $-0.744\,rad$.

Nevertheless, the environmental thermal and humidity condition variations are very slow, and the presented fluctuations of the Ks parameters only occur for mid or long term measurements. Moreover, as explained on sub-section 3.2.6, the uncertainty on the Ks parameters is compensated using real time estimation of the Lissajous ellipse parameters. Unless a high fluctuation of the retro-injected power (Ref_2) occurs (high parasite rotation), the interferometer displacement measurement is not highly impacted by the Ks_{ij} parameters fluctuation.

The mirror relative position was measured over a linear temperature variation ($1\,°C/min$ from $40\,°C$ to $10\,°C$), with different position of the mirror from the chip ($4\,mm$, $7\,mm$, $10\,mm$ and $13\,mm$). Unfortunately the thermal enclosure generate a $200\,Hz$ vibrations of more than $400\,nm$ amplitude. Fig.3.12 shows the measured position drift for the different position of the mirror from the interferometer, filtered with $2\,Hz$ second order low-pass filter.

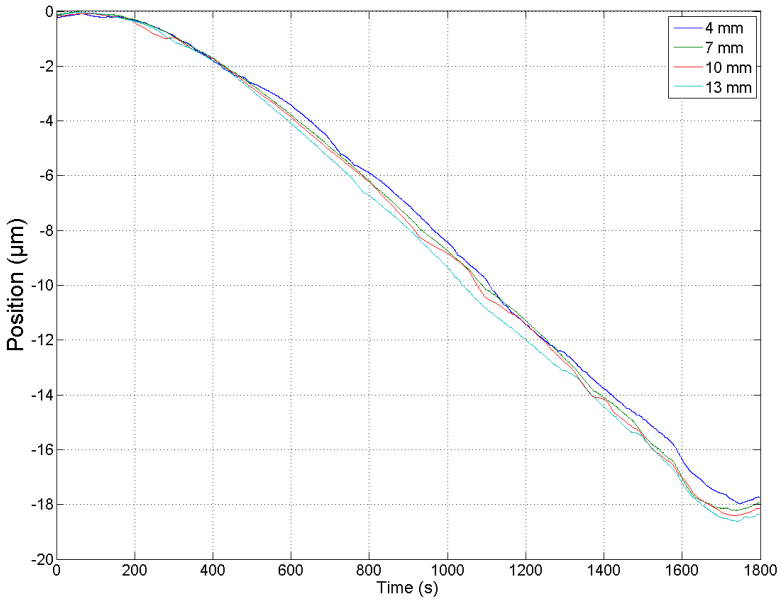

Figure 3.12 The filtered measured mirror position drift under $-1\,°C/min$ temperature variation.

Tab.3.3 presents the measured position drift of the mirror with respects to temperature.

Table 3.3 The measured position drifts with respect to temperature variations at the different positions of the mirror from the interferometer chip.

Position of the mirror from the interferometer chip	Measured position drift with respect to temperature
$4\,mm$	$579.94\,nm/°K$
$7\,mm$	$586.73\,nm/°K$
$10\,mm$	$593.42\,nm/°K$
$13\,mm$	$600.13\,nm/°K$

Most of the measured position drift with respect to temperature is likely due to thermal dilatation of the mirror, supports and the different mechanical parts of the system. To overcome the dilatation effects and to be able to measure the temperature influence on the interferometry measurement, a system composed of only zerodur-like components should be required.

Neverthless, taking into account the fact that the mechanical parts of the system are the same for the different mirror positions measurement, an alternative technique is to assume that the dilatation effects are similar for all the measurements, and then attribute the position drift difference between the measurements to the wavelength variation on the interferometer optical path length difference.

The different measurements couples and the difference in path length between each (note that for a mirror position difference of $3\,mm$, the interferometer optical path length difference is $6\,mm$, because the interferometer laser beam goes to the mirror, is reflected and come-back to be retro-injected into the interferometer input/output lens) are used to compute the wavelength relative variation with respect to temperature. The computed mean wavelength relative variation with respect to temperature using the different couple combination of the measurements is $1.12 \cdot 10^{-6}/°K$. This value is higher than the theoretical one which is $9.46 \cdot 10^{-7}/°K$ (tab.3.1). This is likely due to the uncertainty of the mirror position from the interferometer. Indeed, the mirror is positioned using a simple ruler, and an uncertainty of $250\,\mu m$ on its position have to be considered.

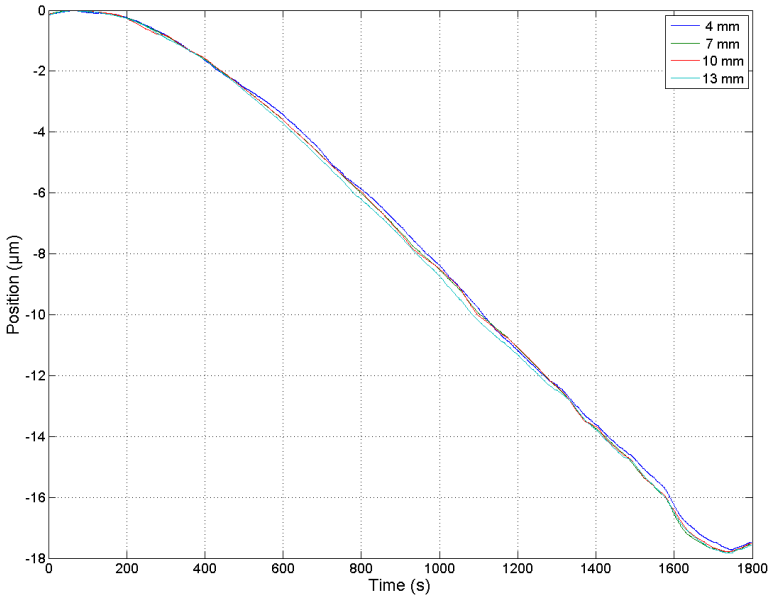

Figure 3.13 The corrected position measured by the interferometer at different positions from the mobile mirror when a thermal drift is imposed.

Fig.3.13 represents the measured position after correction of the wavelength. The remaining drift is due to the dilatation effects in both the sensor, mirror-stage and support sides.

3.4.3 The sensitivity to the humidity

To determine the sensitivity of the interferometer toward the humidity, the same experiment under controlled environment was realized. The mirror relative position was computed over a linear humidity variation ($1\,\%/min$ from $65\,\%$ to $35\,\%$), with different

position of the mirror from the interferometer ($4\,mm$, $7\,mm$, $10\,mm$ and $13\,mm$). The thermal enclosure still generates a $200\,Hz$ vibrations of more than $400\,nm$ transversal amplitude. Fig.3.14 shows the measured position drift for the different position of the mirror from the interferometer, filtered with $2\,Hz$ second order low-pass filter.

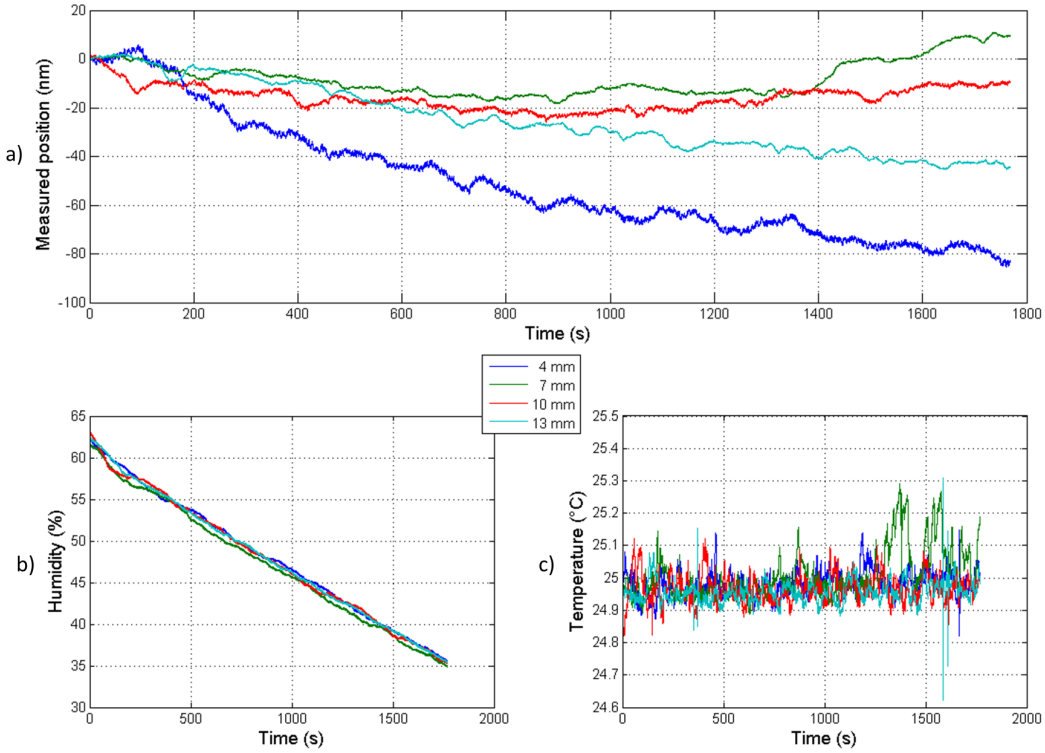

Figure 3.14 a) The position measured by the interferometer at different positions from the mobile mirror when a humidity drift is imposed, and b) the measured humidity and c) temperature (with the weather card) all over the experiment.

Unlike the temperature drift measurement, the obtained curves does not fit to the theoretical sensitivity of the wavelength toward the humidity. Moreover, the measured positions behavior for the different mirror positions does not seem to follow the humidity drift (see fig.3.14 c). This results can be explained, because of temperature fluctuations all over the experiments. It happens that the temperature fluctuates also of $\pm 0.2\,°K$. Indeed, the influence of a $0.1\,°C$ temperature variation is equivalent to $10\,\%$ humidity variation (see tab.3.1). The thermal enclosure temperature stabilization performances does not allow the measurement of the position drift resulting from humidity variation.

3.4.4 The laser source stability

The noise isolation and the refractive index fluctuation are not the only issue for environmental conditions. The fluctuation of the wavelength of the source is also a parameter which influences the long term measurements. For the *RIO* source that we are using [135], the Allan standard deviation of the wavelength is limited to 10^{-8} over thousands of seconds ($\Delta\lambda = 15,5\, fm \,@\, 1,55\,\mu m$). Moreover, the source is also affected by the temperature and it limits the actual displacement range. For example, with an uncertainty of $1\,°C$, the relative uncertainty of the wavelength is $\Delta\lambda(1\,°C) = 465\, fm$.

The displacement range is then affected such that:

$$L \leqslant \frac{p \cdot \Delta\lambda}{\lambda} \tag{3.26}$$

with p the targeted measurement accuracy, for example, with the uncertainty of $1\,°C$ the maximum range is $3\,mm$ if $1\,nm$ of accuracy is required. This may be problematic for applications like multiscale scanning when the displacement range is a concern.

Also, this uncertainty in the wavelength has an impact on the measured displacement such that if we apply the standard uncertainty formula on eq.2.17, in regulated environment (no change in the refractive index $\Delta n = 0$) then:

$$\Delta[\Delta x] = \left|\frac{\delta[\Delta x]}{\delta\lambda_0}\right| \cdot \Delta\lambda = \left|\frac{\Delta\alpha^1(k \cdot T_s)}{4 \cdot \pi \cdot n}\right| \cdot \Delta\lambda \tag{3.27}$$

3.5 Conclusion

This chapter deals with the metrological interferometric measurement specificities and sources of errors, applied to the studied interferometer. The system maximum displacement velocity is demonstrated and its compensation using a parallel coarse position sensing system is highlighted. The sensor robustness to temperature and humidity variations, under controlled environment is shown and discussed.

Chapter 4

Characterization of the conducting interpenetrated polymer

Contents

4.1 Introduction

The fast development and integration of micro/nanostructures in industries and research laboratory systems, led to an increasing need for new materials which are suitable for easy integration with embedded functionalities. Since a few decades, various types of actuators and sensors, such as shape memory alloy (SMA), silicon, MEMs/NEMs structure, piezo- electric, ionic polymer metal composite (IPMC) and electroactive polymer (EAP) were proposed to fulfill these requirements.

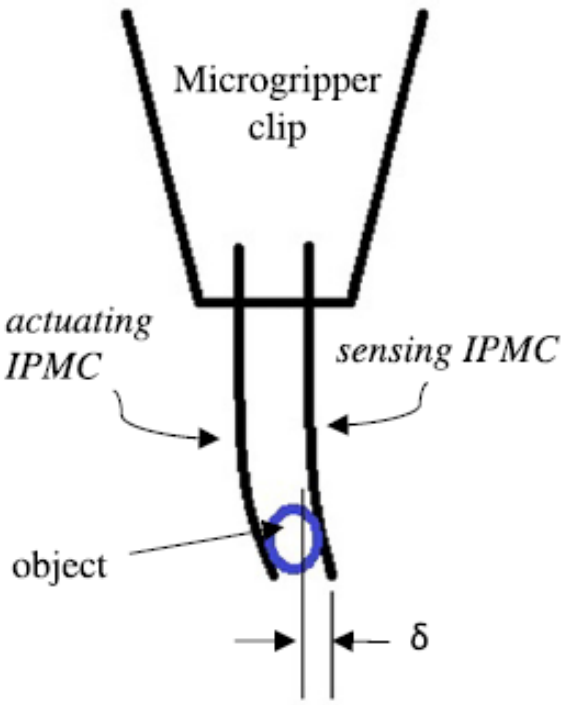

Figure 4.1 The actuator and sensor IPMC based microgripper of the University of New Mexico [136].

For example, the studies of EAP for integration in micro-grippers was prompted by the limit encountered with solutions based on piezoelectric material. Although piezoelectric is a good solution due to its high resolution, compactness and efficiency, it still exhibits relatively low deformation for very high voltage actuation when compared to EAPs. EAP offers flexibility, high bending capabilities, compactness and high power to mass ratio. Moreover, EAPs are actuated with low voltage ($< 2.5V$) and exhibits high deformation capabilities, making them a serious candidate for artificial muscle emulation and micro grippers conception [137]. Several EAP based micro gripper can be found in the literature [138, 139, 140, 141].

The EAP provided by the LPPI laboratory (University of Cergy Pontois) exhibits both linear actuation and sensing functions. These particularities make it very interest-

ing for the conception of innovative tools at micro-scale. EAP is indeed able to realize deformation while providing with feedback information. At macroscale, another student of our lab was already able to demonstrate the use of this EAP to design a gripper with one active finger (for actuation) and a passive one (for sensing purposes). The next step is to develop a microgripper for both micro scale objects manipulation and positioning, in the image of what was done by Gonzalez *et al.* (cf fig.4.1), in their actuator/sensor IPMC based micro gripper controlled by PID. Hereafter, our objective is to investigate the micro-meter capabilities for future use at micro-scale, and characterize the sensor function to provide feedback information on the sample position. This has been realized with the help of the interferometer presented in chapter 2.

In order to integrate the polymer in micromanipulator applications, as a microgripper, that consist on an actuator polymer finger and a sensor polymer finger, the polymer response to an applied voltage in actuator mode, as well as its response to an applied deformation must be characterized. In this work, we investigate the sensor mode response of the polymer, its actuator mode function being widely studied in the literature [142, 143, 87, 144, 93], before demonstrating its micrometer capabilities in both actuator and sensor mode.

In this chapter, the studied IEAP (ionic electroactive polymer) is assimilated to a cantilevered beam with a fixed and a free end. It is used to evaluate the stiffness of the material and the relationship between the force and the displacement. The parameters were obtained while analyzing the step response of the IEAP. An electro-mechanical model is then studied to characterize the sensor mode. Its frequency response is analyzed to define the sensor bandwidth and resolution. Moreover, the sensor transfer function is identified to analyze the gain and phase shift of the IEAP. The frequency response must be indeed identified to use the IEAP as a banding strain sensor. The micrometric capabilities of the IEAP are demonstrated in both actuating and sensing modes, using experimental setups based on the previously presented interferometer. At the same time, the robustness of this interferometer to power fluctuation is highlighted and exploited in the micrometer actuation demonstration.

4.2 Background on ionic electro-active polymers

The material which has been used in this chapter is called "conducting trilayer interpenetrated polymers". It belongs to the Ionic Electro-Active Polymers (IEAP) class and consist of three layers. Two actively contracting conducting polymers layers, and a polymer electrolyte support inflated by a ionic liquid third layer between those

two conducting polymers. Conducting polymers (CP) are electronically and ionically conductive materials that can be assimilated to strain transducer. Regarding the studied IEAP in flexion configuration, an applied voltage between the two CP electrodes results in the flexion of the IEAP. On the other hand, a mechanical deformation applied to the IEAP generates a voltage between the CP electrodes. The flexion leads to the migration of ions from a CP to the other one through the electrolyte support. This produces a compression and an expansion of the respective CPs. The studied IEAP demonstrates very interesting actuating properties. It combines low voltage actuation (around 2V for large deflections) and large banding capabilities, which makes it suitable for integration in several micromachining and micro-robotics systems. IEAP are indeed often called artificial muscles. In the literature, studies about active IEAP based catheter were realized over several years and resulted in a fully optimized active IEAP based catheter [145, 146]. Several IEAP were used in demonstrators that integrate grippers [140, 141]. Their capabilities like lightness, flexibility and robustness make them a good candidate for applications at microscale. Moreover, the fabrication process of IEAPs allows low cost production and ease of integration. Finally, the studied IEAP is able of both actuation and sensing. This specificity allows for a feedback signal while actuating. This particularity may be of great interest for obstacle or contact detection while actuating, or even active sensing mode as tapping probe mode in atomic force microscopy.

4.3 Mechanical characterization of the IEAP

This section provides the reader with background on cantilevers beam. Here, one extremity of the polymer is clamped between two printed circuit to realize acquisition/actuation. The other extremity is free. In this work, the polymer was characterized and studied in the same manner as a cantilever beam. The aim of this section is to establish a link between the transverse displacement of the polymer and the applied force at its extremity. The configuration that corresponds to the deflection is first presented to derive the expression of the stiffness with respect to its Young modulus. The free oscillation mode of the cantilever is thus presented to express the Young modulus with respects to the beam fundamental frequencies. Finally, the Young modulus is computed using the beam fundamental frequency measurement.

4.3.1 Model of the polymer deflection

Let us consider a horizontal cantilever with a length L, a width w and a thickness h. It is subject to a vertical force F as illustrated in fig.4.2, such that the beam is deflected.

The amplitude of the deflection is noted x (x on fig.4.2).

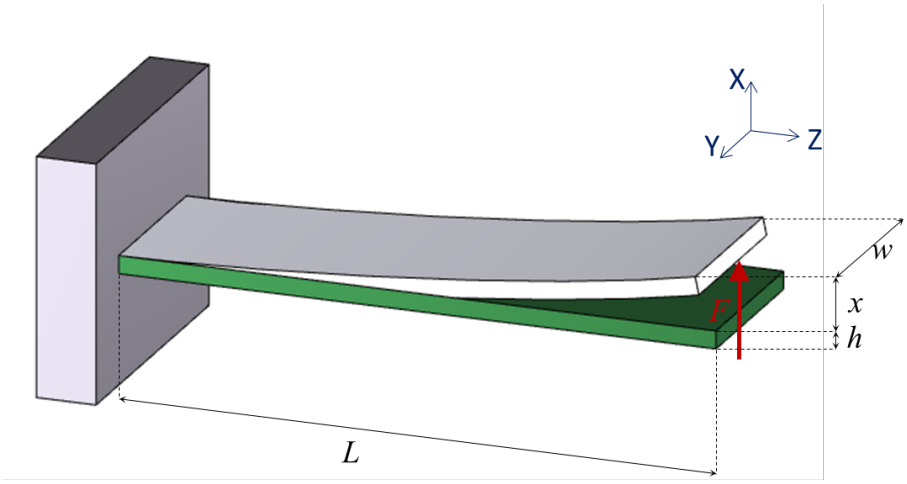

Figure 4.2 Cantilevered beam with a fixed end and a free end.

The stiffness of the system can be derived from the expression of the displacement $x(z)$ where z is the point where the force is applied. z is in the range of $[0,\ L]$ [147]:

$$x(z) = \frac{F \cdot L}{E \cdot I} \cdot (\frac{z^2}{2} - \frac{z^3}{6 \cdot L}) \tag{4.1}$$

Where E is the Young modulus of the beam, $I = \frac{(w \cdot h^3)}{12}$ its moment of inertia and $x(L) \ll L$ (slight deformations assumption).

According to eq.4.1, the displacement at the free end of the beam is:

$$x(L) = \frac{F \cdot L^3}{3 \cdot E \cdot I} \tag{4.2}$$

With $\frac{(3 \cdot E \cdot I)}{L^3}$ the system stiffness.

The stiffness depends on the beam dimensions and on the Young modulus. The knowledge of the Young modulus is thus necessary to connect the deformation to the applied force. In beam theory, the Young modulus is connected to the fundamental frequencies. Therefore, in the next section, theoretical results about free oscillation are recalled.

4.3.2 Free oscillation of the beam

Hereafter, we will assume that the mechanical constraint induced by the force F is released. Consequently, the beam will oscillate with a free mode described in [148].

Eq.4.3 describes the oscillation with respect to the time t and position on the beam z:

$$E \cdot I \cdot \frac{\delta^4 x(z,t)}{\delta z^4} = -\rho \cdot A \cdot \frac{\delta^2 x(z,t)}{\delta t^2} \tag{4.3}$$

where ρ and A are respectively the density and the section of the beam.

It is usually assumed, that the displacement can be expressed as the product of two no-correlated parts (separation of variables [149]). The first one depends on the position from the fixed end and the second one on time. It leads to $x(z,t) = X(z) \times f(t)$ the beam transverse displacement at the time t and position z from the beam fixed end. This assumption results in the differential equations eq.4.4 and eq.4.5 [148]:

$$\frac{\delta^4 X}{\delta z^4} - (\frac{\beta_i}{L})^4 \cdot X = 0 \tag{4.4}$$

$$\frac{\delta^2 f}{\delta t^2} + 2 \cdot \alpha \cdot \frac{\delta f}{\delta t} + \omega_i^2 \cdot f = 0 \tag{4.5}$$

where ω_i is the i^{th} fundamental frequency of the beam and α is the introduced damping coefficient. The term β_i is defined as:

$$\beta_i^4 = \frac{\omega_i^2 \cdot m \cdot L^3}{E \cdot I} \tag{4.6}$$

where m is the mass of the beam.

The general solution of eq.4.4 is a linear combination of trigonometric equations:

$$\begin{aligned} X(z) = c_1 \cdot (cos(\beta_i \cdot \tfrac{z}{L}) + cosh(\beta_i \cdot \tfrac{z}{L})) + c_2 \cdot (cos(\beta_i \cdot \tfrac{z}{L}) - cosh(\beta_i \cdot \tfrac{z}{L})) \\ + c_3 \cdot (sin(\beta_i \cdot \tfrac{z}{L}) + sinh(\beta_i \cdot \tfrac{z}{L})) + c_4 \cdot (sin(\beta_i \cdot \tfrac{z}{L}) - sinh(\beta_i \cdot \tfrac{z}{L})) \end{aligned} \tag{4.7}$$

The c_1 , c_2 , c_3 and c_4 parameters can be identified using the boundary conditions. The fixed end must have zero displacement and zero slope due to the clamp, $X(0) = 0$ and $\frac{\delta X(0)}{\delta z} = 0$ at $z = 0$ lead to $c_1 = c_3 = 0$. Moreover, the bending moment at the free-end of the beam is null and therefore $\frac{\delta^2 X(L)}{\delta z^2} = 0$. At the same extremity, the shearing force is null and $\frac{\delta^3 X(L)}{\delta z^3} = 0$. According to these conditions:

$$\begin{cases} c_2 \cdot (-cos(\beta_i) - cosh(\beta_i)) + c_4 \cdot (-sin(\beta_i) - sinh(\beta_i)) = 0 \\ c_2 \cdot (sin(\beta_i) - sinh(\beta_i)) + c_4 \cdot (-cos(\beta_i) - cosh(\beta_i)) = 0 \end{cases} \tag{4.8}$$

The solution of eq.4.8 is the frequency equation for a cantilever beam:

$$cos(\beta_i) \cdot cosh(\beta_i) = -1 \tag{4.9}$$

According to the literature, eq.4.9 can be solved with the constants β_i (see tab.4.1), which define the fundamental frequencies of the beam using eq.4.6.

Table 4.1 Six first constants for a cantilevered beam vibration.

Order	β_i
1	1.875...
2	4.694...
3	7.855...
4	10.996...
5	14.137...
6	17.279...

Moreover, eq.4.8 provides a link between the two remaining parameters. Therefore, eq.4.7 is reduced to only one unknown parameter. It is computed using the boundary condition $X(L) = 1$.

The general solution of eq.4.5 is in the form:

$$f_i(t) = e^{-\alpha \cdot t} \cdot (A_i \cdot cos(\omega_i \cdot t) + B_i \cdot sin(\omega_i \cdot t))$$

where A_i and B_i are parameters that depend on the initial conditions. However, at $t = 0$, the applied force is released and the beam velocity is null. It leads to $B_i = 0$ and the Ai parameters depend on the initial deflection (see eq.4.1).

4.3.3 Fundamental frequency and damping coefficient measurement

Experimental setup

In this experiment, a polymer of 0.25x4 mm^2 section with a free length of 27 mm is used. It is clamped into a printed circuit while the other extremity is free. The output voltage of the polymer is measured and recorded through a NI $PCI - 4472$ acquisition card. The experiment was realized five times with different initial spread position. As explained in the previous section, a force applied to the polymer is released and the polymer freely oscillates before relaxing and reaching its initial state. The measured voltage is a damped sinusoidal curve which is used to identify both the fundamental frequency and the damping coefficient.

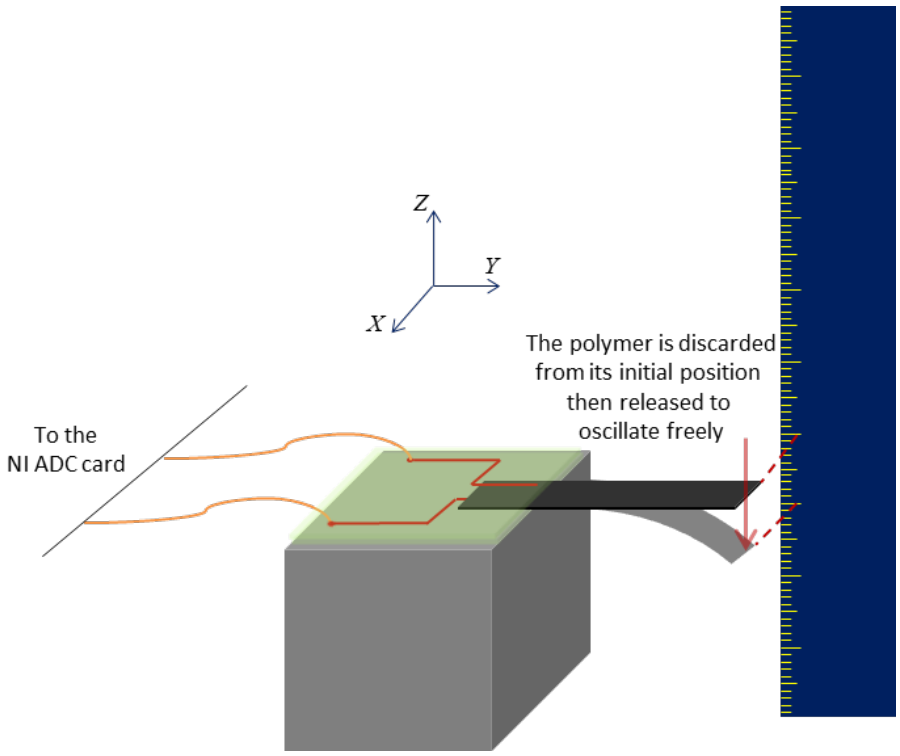

Figure 4.3 The polymer fundamental proper frequency measurement experiment

Results and discussion

The results obtained with this sample are in tab.4.2.

Fig.4.4 represents the measurements obtained for different initial deformations in the range $[5,\ 15]\,mm$. This experiment was repeated five times to demonstrate that the results is repeatable with a maximum deviation of $0.85\,Hz$ concerning the fundamental frequency measurement, and $16.45\,MPa$ for the Young modulus.

Table 4.2 The initial displacement imposed to the polymer free extremity and its measured first fundamental frequency.

Initial displacement (mm)	First fundamental frequency (Hz)
7	17.13
10	17.20
11	16.40
12	16.84
14	17.96

Fig.4.5 represents the computed FFT applied to previous data. The FFT shows that the polymer oscillates at the pseudo-frequency of $16.75\,Hz$ and the pseudo-pulsation

$\omega_d = 105.24\, rad.s^{-1}$. Moreover, with the damped sine wave in fig.4.4, the logarithmic decrement δ can be computed with:

$$\delta = \frac{1}{n} \cdot ln(\frac{A_0}{A_n})$$

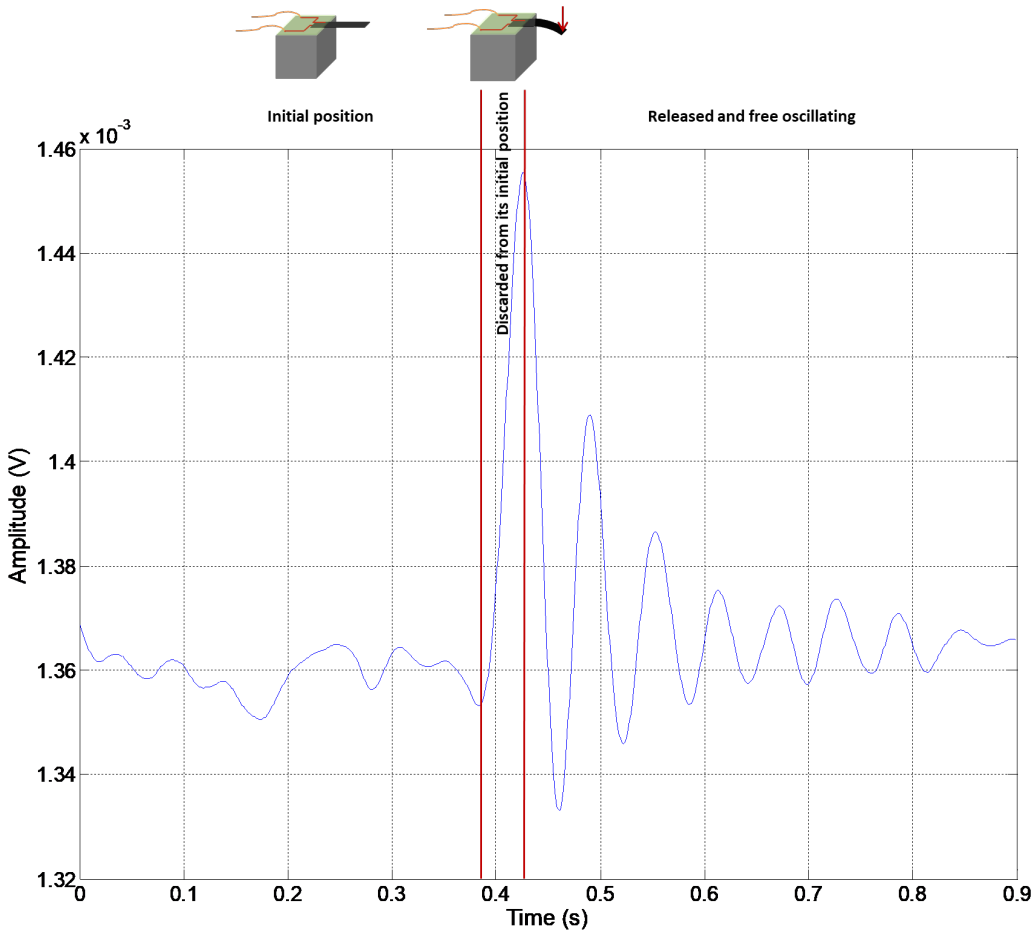

Figure 4.4 The free answer of the polymer beam under initial deformation effect.

where n is the number of cycles used to measure the logarithmic decrement. A_0 and A_n are the amplitudes at times $t = t_0$ and $t = t_0 + n \cdot T_d$, with T_d the pseudo-period of the damped sine wave.

Furthermore, a bandpass-like filter is observed on the FFT for low frequencies (fig.4.5). This range of low frequencies will be highlighted and discussed in the next section. The free oscillation of the polymer under initial deformation effect may be approximated to an impulse response.

In this work, the logarithmic decrement was computed using only three cycles because of the low signal to noise ratio observed after the third cycle (the peak to peak

noise is around $20\,\mu V$). The logarithmic decrement is $\delta = 0.59$, and the damping ratio is then extracted $\zeta = 0.93$, with:

$$\delta = \frac{2 \cdot \pi \cdot \zeta}{\sqrt{1 - \zeta^2}}$$

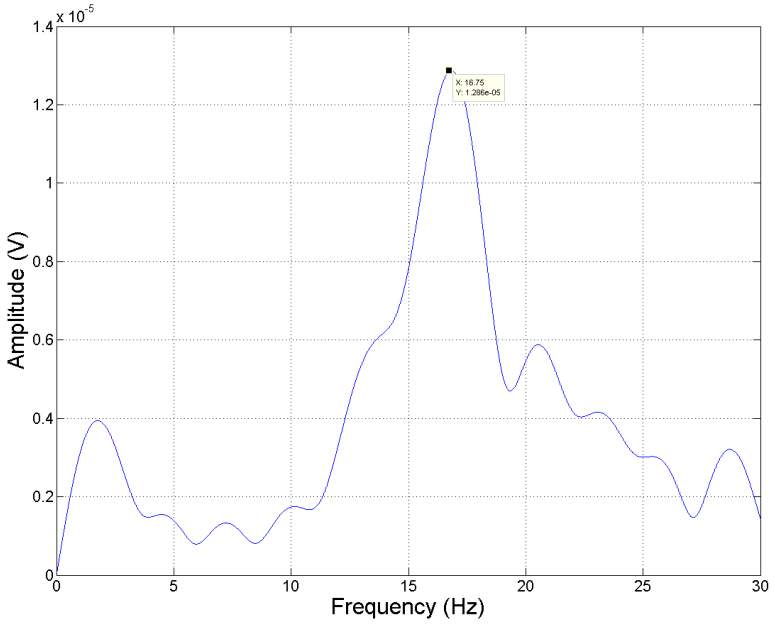

Figure 4.5 The computed FFT on the fundamental frequency measurement for a $0.25x4\,mm^2$ section and $27\,mm$ free length polymer.

The polymer mechanical fundamental frequency $\omega_1 = 105.8\,rad.s^{-1}$ is then computed with:

$$\omega_1 = \frac{\omega_d}{\sqrt{1 - \zeta^2}}$$

A comparison with the results obtained in the literature is presented on the next subsection.

4.3.4 Young modulus and stiffness measurements

To measure the Young modulus using eq.4.6, we first measure its mass using a scale ($1\,mg$ of uncertainty). A sample with the dimensions 0.25x4x27 mm^3 is then used. Its volume is then computed to calculate the young modulus $E = 162.27 \pm 16.45\,MPa$ using $\beta_1 = 1.875$. This result is in perfect harmony with the Young modulus obtained in A. Fannir PhD work ($157 \pm 15\,MPa$), with a tensile test measurement of the polymer Young modulus (measurement of the required strain to achieve linear polymer deformation in traction condition) [92, 143].

Table 4.3 First fundamental frequency and Young modulus measurements.

First fundamental frequency (Hz)	Young modulus (MPa)
17.13	162.58
17.20	163.91
16.40	149.02
16.84	157.12
17.96	178.72

Finally, the stiffness can be derived from the polymer Young modulus and dimensions. For example, the system stiffness is of $0.125\,N/m$ for the sample considered in these experiments.

The stiffness of every polymer dimensions can be calculated using the determined Young modulus. The stiffness bind the transverse realized displacement to the applied force. The polymer is a strain transducer. It converts a sensed/applied voltage into an applied/generated strain. In the next section, the polymer is electromechanically characterized in sensor mode. The aim is to link the measured voltage between the polymer bounds, to the imposed transverse displacement at the polymer ends. Note that the polymers used in this work are all from the same synthesized large sample.

4.4 Sensor mode: electromechanical characterization

In order to integrate the polymer in a micromanipulator setup, the response of the polymer to an input voltage and its response to an applied deformation must be identified. Based on these results, it is possible to propose innovative systems like microgrippers. One polymer could be used as an actuated finger while another one could be set as a sensing part.

In this section the polymer sensor function is studied. The system noise is first identified to define the measurement resolution. The transducer capabilities are studied in a cantilever beam like configuration. The imposed transverse displacement at the polymer free end is linked to the measured voltage between its bounds. The polymer voltage/deformation transduction gain, its sensing bandwidth and frequency response are determined through the identification of the transfer function of the system. The identified system input is the polymer deformation realized through a perpendicular displacement at its extremity, and its output is the measured voltage between the polymer bounds. The characterized polymer of $250\,\mu m$ thickness and $4\,mm$ width was studied in flexion in a $30\,mm$ free length configuration.

4.4.1 Noise and resolution

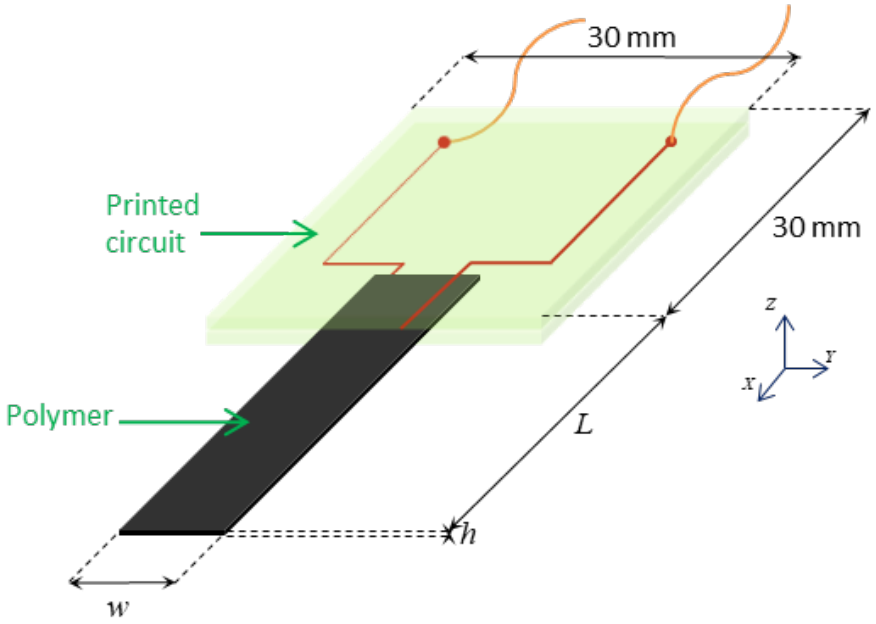

Figure 4.6 Illustration of the polymer/support system. The polymer is represented in black and is gripped between two printed circuits, which subtract is represented in green and the copper track in red, and wires in orange are welded to the circuits end.

The polymer is gripped between two symmetrical printed circuits. Each electrode is in contact with a copper track wired to the board in charge of input/output. In sensor mode, the electrodes are directly plugged to a $24 - bits$ acquisition card from NI. The measured voltage in sensor mode is in the range $[-300,\ 300\,\mu V]$. Therefore, the acquisition of the signal must be done with a high resolution card. In actuator mode, the system is in series with a $50\,\Omega$ resistance to prevent high current through the polymer. The actuating voltage is in the range $[-2,\ 2\,V]$ and is applied between the electrodes.

To estimate the noise level, the polymer is plugged to the NI acquisition card. The sampling frequency is set to $1\,kHz$ and measurements are made with ambient environmental conditions. The measured signal is centered around $28.5\,\mu V$ due to the polymer imperfections. The electrodes are not perfectly parallel and the electrolyte support is not a perfect parallelepiped neither. Moreover, the gravity field is acting on the polymer and it is already slightly deformed at the beginning [72]. The static measurement shows a noise amplitude around $15\,\mu V$ which is primarily composed of a $50\,Hz$ harmonic.

However, the histogram demonstrates that the measured noise is Gaussian (see fig.4.7). The standard deviation of this Gaussian noise is of $10\,\mu V$. The noise is probably

mainly due to the very small gap between the two copper tracks. It results in an antenna phenomena and adds a capacitor effect between the polymer electrodes. Different length and width were considered for the polymer but the same noise was observed. It suggests that the polymer geometry does not affect the noise level as well as its nature.

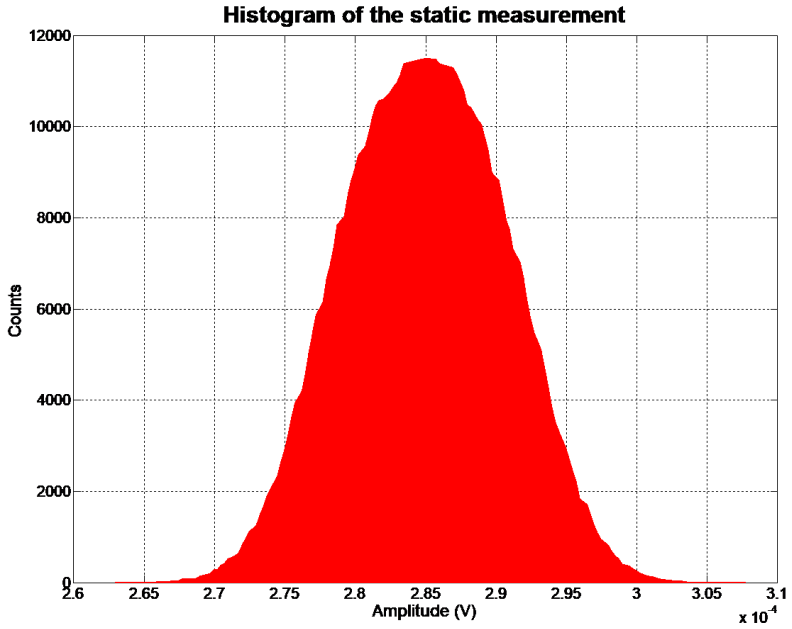

Figure 4.7 The histogram of the static measure.

Hereafter, a $40\,Hz$ low-pass second order Butterworth filter is applied to the output signal to reduce the impact of this noise on the measurement. The standard deviation of the Gaussian noise is then reduced to $2.25\,\mu V$. An analog second order filter is also added to the final embedded system to detect the slightest deformation of the polymer.

Finally, based on the measured Gaussian noise standard deviation, the 6σ-resolution of this sensor can be defined as $13.5\,\mu V$. An example of the response of 0.25x4x30 mm^3 polymer to a $10\,mm$ amplitude sinusoidal excitation at extremity is represented in fig.4.8.

In this sub-section, the system noise was studied and its resolution was defined. Next, the polymer frequency response to a transversal displacement of its free extremity will be studied and characterized. The aim is to identify the system transfer function to link the measured voltage to the applied deformation.

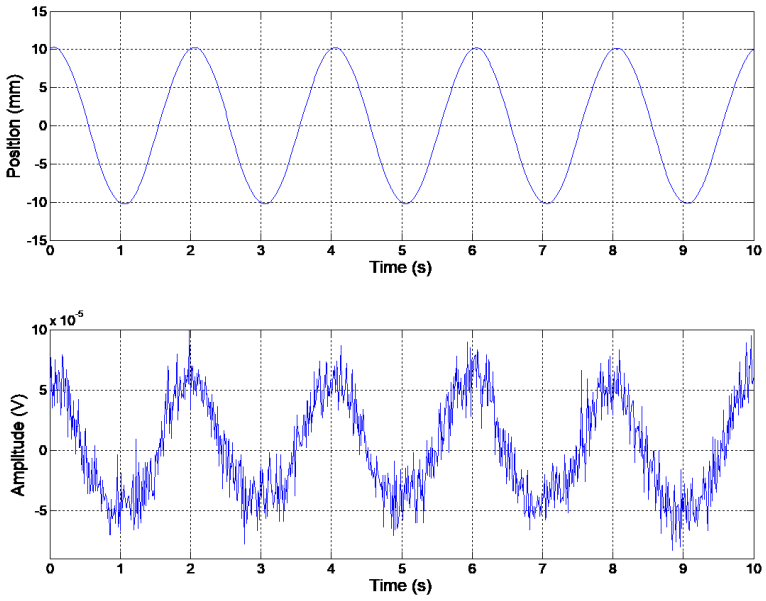

Figure 4.8 Response to a 10 mm amplitude sinusoidal excitation applied to the tip of the polymer (0.25x4x30 mm^3).

4.4.2 Experimental setup

To realize this experiment, the ElectroPuls $E3000$ dynamic testing machine from Instron was used. The setup is suited for static and dynamic measurement of materials and components. It is based on two vertically positioned grips, that fixes the sample. The lower grip is static, while the upper grip is joined to a voice coil motor. The upper grip performs high speed displacement, that reaches 100 Hz frequency in a 60 mm full stroke.

The setup includes a load cell for force sensing and an optical encoder for position measurement. The load cell resolution is of a few hundred of mN which is not enough to characterize the polymer. A threshold value of a few mN is necessary to bend the sample. The optical encoder, on the other hand, allows for micrometric resolution (the manufacturer claims a measurement with an uncertainty of 10 μm). This value is quite enough for next experiments.

To characterize the polymer, a support made of two mechanical parts was built as illustrated in figure fig.4.10.

A sinusoidal translation of 5 mm amplitude is imposed to the moving arm of the ElectroPuls $E3000$. The output voltage is measured with the NI board and we aim to identify the transfer function with a Bode diagram. The imposed frequencies are the decimals of the logarithmic frequency scale of the four decades in the range [0.001,

10] Hz. A 10 periods time window is realized at each testing frequency. A 10 s break is performed between each two testing frequencies, to insure non-correlation between the consecutive measurements.

Figure 4.9 ElectroPuls $E3000$

The choice of this frequency range was made according to the previous results and the studies of the sensor mode function [88, 72]. The highest frequency used for measurement is of 30 Hz [94]. For our experiments, the frequency was limited to 10 Hz in order to protect the polymer from potential delamination or breaking.

The displacement of the moving arm is measured with both an integrated optical encoder and the interferometer fixed to the lower grip of the ElectroPuls $E3000$. The displacement of the moving mirror is measured (see fig.4.10) when the laser beam is retro-injected into the interferometer. The position is recorded and the output voltage of the polymer is measured with a $24 - bits$ NI $PCI - 4472$ acquisition board. The sampling frequency is set to 1 kHz. However, the interferometer performs acquisition at a frequency of 50 kHz but a mean value is computed every 50 samples (with low-pass filter like).

This experiment still faces a problem since the measurement with the optical encoder is realized with the Instron embedded system while a NI board (DAC card + Labview Code) is used for other measurements. As a consequence, measurements are

not synchronized natively. To compensate for the delay, the measured position was first synchronized with the inter-correlation technique. The measured position with the embedded optical encoder system is then synchronized with the measured voltage between the polymer bounds.

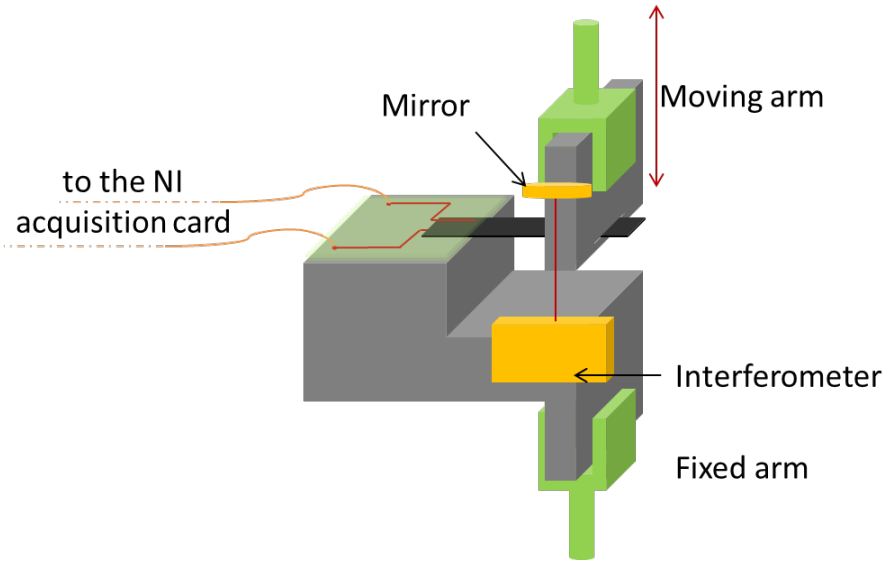

Figure 4.10 Experimental setup for frequency identification in sensor mode. The built mechanical parts are represented in gray.

The optical encoder is used to correct the measurements provided by the interferometer. The measured position with the interferometer is used to characterize the polymer. The very high resolution interferometer system is used in parallel to a higher velocity but common resolution position measurement system (optical encoder), to compensate from the interferometer velocity limitation. This compensation of the interferometer displacement speed limitation using a high velocity but low resolution position sensor is presented in the previous chapter.

4.4.3 Data post-processing and results

A complex Fast Fourier Transform of both the input (the polymer deformation) and output (the measured voltage at the polymer bounds) is applied to the data. This is made for each input frequency. The magnitude of the transfer function is computed with the gain in amplitude from the FFT of the output and input for a given frequency. The phase shift is computed with the difference between the FFT angles. The resulting Bode diagram is presented in fig.4.11.

The error bars on this Bode diagram correspond to the maximum deviation computed with the different measurements. This experiment was repeated ten times so

that a set of mean values was computed for each frequency (complex mean value). The maximum deviation of magnitude and phase for the different measurements have been set as the experimental uncertainty in fig.4.12.

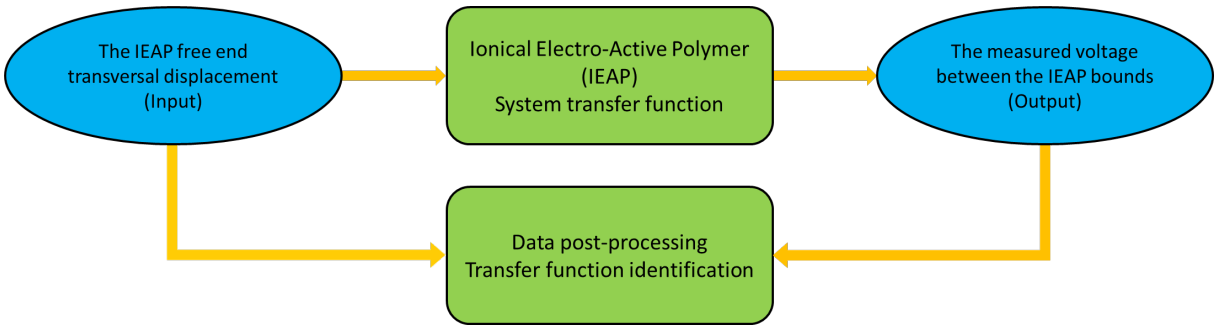

Figure 4.11 The system transfer function identification concept.

The Bode diagram suggests a bandpass behavior with a $10\,db/dec$ slope at very low frequencies and a $-10\,db/dec$ slope for higher frequencies. Part of the phase at both slopes varies in the opposite direction to the gain. This suggests a non-minimal phase system with the presence of at least one unstable zero and one unstable pole.

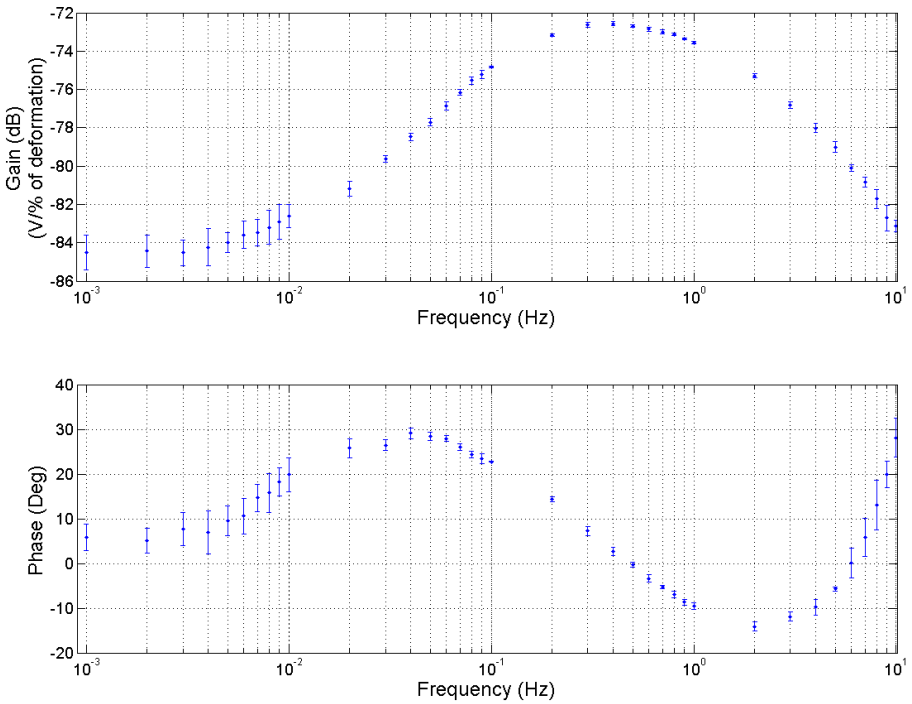

Figure 4.12 Bode diagram with amplitude and phase of the identified transfer function. with the mirror displacement as input, and the measured voltage as output.

4.4.4 Identification of the transfer function

We are interested in the best fitted transfer function according to the Bode diagram. The Matlab ident function is used to estimate the transfer function. The best fit is obtained with a 2 poles and a 2 zeros system with a 69.87 % of confidence.

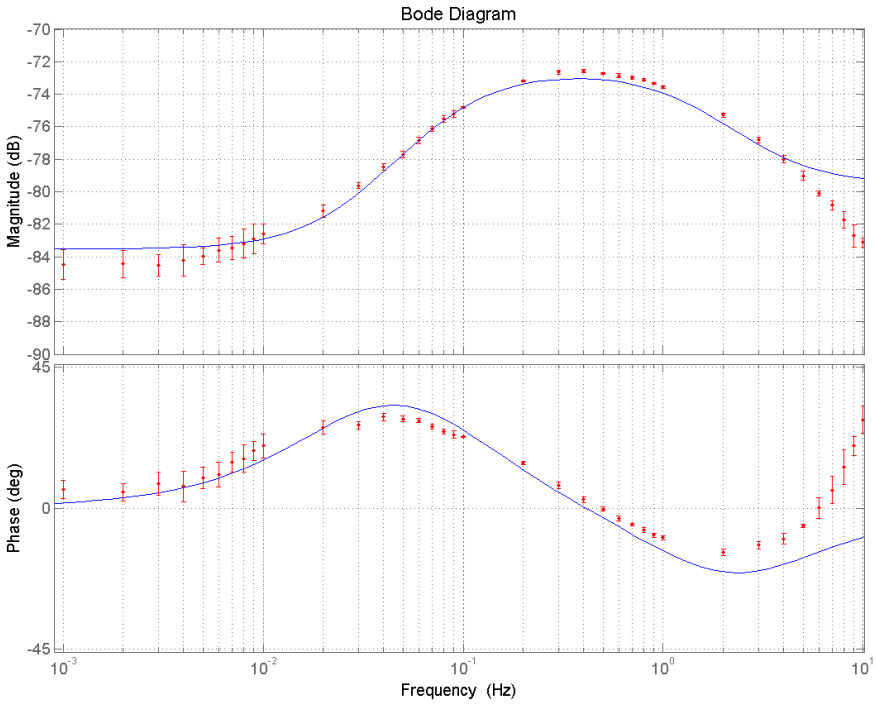

Figure 4.13 Bode diagram: identified model is in blue and experimental results in red.

Fig.4.13 represents the identified transfer function using the Matlab toolbox. One can see that the identification exhibits a good fitting for frequencies lower than $2\,Hz$. This approximated transfer function seems suitable to compute the deformation, using the output voltage of the polymer in the low frequency range ($< 2\,Hz$). Finally, the transfer function is a second order system written as:

$$H(S) = \left(\frac{1.71 \cdot 10^{-4} \cdot (s + 0.155) \cdot (s + 20.354))}{(s + 0.544) \cdot (s + 9.177)}\right.$$

In fig.4.14, the transfer function is evaluated with an input signal of $0.4\,Hz$. As shown in the bode diagram (fig.4.13), a deviation of less than $1\,dB$ in gain and 10° in phase should be observed at this frequency.

Fig.4.14 shows experimental and simulated results for the sine wave with a frequency of $0.4\,Hz$. According to this figure, the maximum error is below the 6σ-resolution defined previously ($13.5\,\mu V$). Moreover, this model shows similar results for all input frequencies under $5\,Hz$ so that it seems suitable within this frequency range.

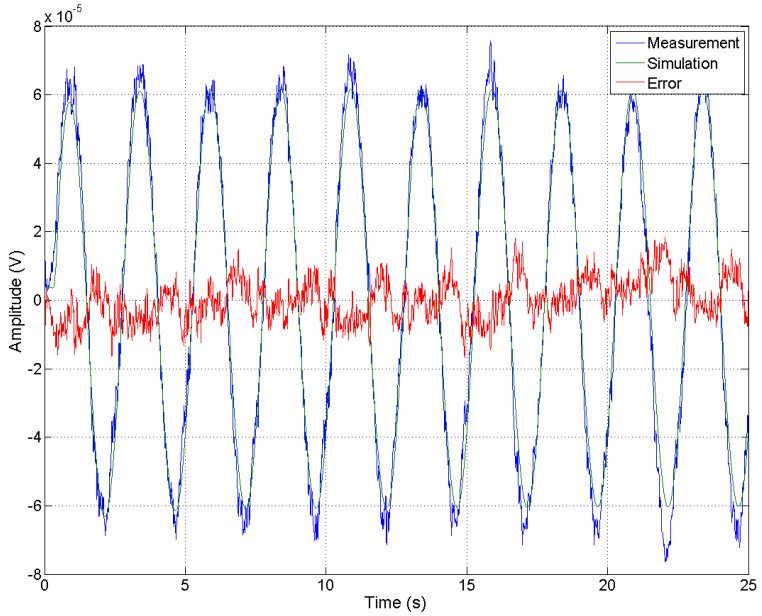

Figure 4.14 Simulation and measurement of the output voltage of a polymer of $30\,mm$ length and $0.25x4\,mm^2$ section submitted to a $5\,mm$ amplitude sinusoidal deformation at $0.4\,Hz$ at its end.

In figure Fig.4.15, the same experiment is conducted with an input frequency of $8\,Hz$. As predicted in the Bode diagram (see fig.4.13), the gain of the identified transfer function is higher and there is a phase shift between the model and experimental data.

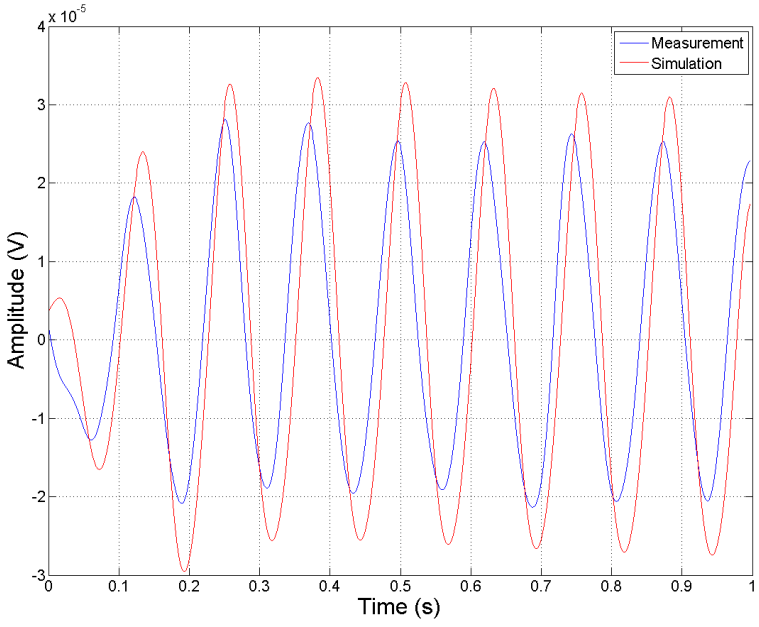

Figure 4.15 Model simulation and measurement of the output voltage of a polymer of $30\,mm$ length and $0.25x4\,mm^2$ section submitted to a $5\,mm$ amplitude sinusoidal deformation at $8\,Hz$ its end.

It is thus necessary to better model the transfer function for frequencies higher than $5\,Hz$.

4.4.5 Fractional order approximation

We chose to the treat the system as fractional order system to better fit the experimental data on the whole frequency range. This choice was also made because of the half slopes observed on the Bode diagram, that suggests a half fractional order system. The flexibility of fractional order modelization might be of interest to reach our goal. Moreover, fractional order systems seem to be suitable for infinite networks of impedances [89]. In the sequel, a model will be proposed for this approach.

Equivalent electrical circuit

Farajollahi *et al.* [86] have proposed an equivalent electrical circuit (see fig.4.16) based on a $2D$ infinity of RC cells transmissions lines to model the PEDOT electrodes. A resistor is used to model the ionically conductive separator. In [86], this model was simplified and used to compute a state space model in actuator mode.

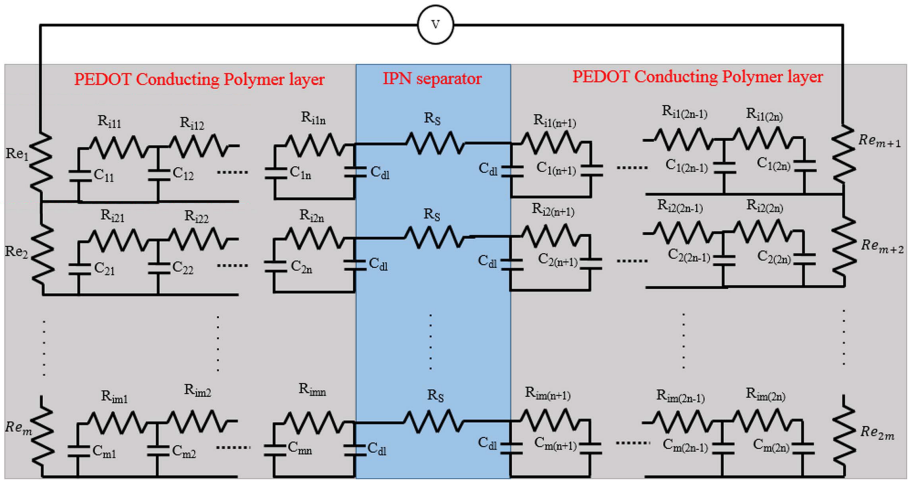

Figure 4.16 Equivalent electrical circuit.

This model first appeared in [85] as an analytical model to describe the electrochemical impedance of conducting polymers. In this work, the impedance of a PEDOT electrode is combined to a ionically conductive separator. The model is then validated with simulation and measurement. Shoa *et al.* have modeled and studied both a $1D$ RC transmission line and a $2D$ RC transmissions lines (defined by the R_{em}, $(R_{im(1..n)}C_{m(1..n)})$ transmission line).

According to this model, the impedance of the $1D$ transmission line is:

$$Z_1(s) = \frac{R_i}{\sqrt{(R_i \cdot C \cdot s} \cdot tanh(\sqrt{R_i \cdot C \cdot s \cdot h})}$$

where R_i and C are respectively the resistance and the capacitance of the polymer per thickness [85].

In addition, one of the first studies about fractional order systems (Suhashi *et al.* [89]) has demonstrated that a fractional operator system can be approximated to an infinite RC transmission line. In this work, the RC transmission line is realized using a bilayer thin-film composed of a resistive layer and a dielectric layer.

Suhashi *et al.* have demonstrated the approximation of a RC transmission line to a half fractional order impedance ($s^{-0.5}$). Moreover, in this work, it has been shown that the standard equivalent circuit of a fractional order system is a two impedances transmission line (an impedance in series and the other one in parallel).

In fact, when applied to the studied polymer, with $s = j\omega$:

$$Z_1(s) = \sqrt{R_i/C} \cdot s^{-0.5} \qquad were\ s = j\omega\ and\ R_i \cdot C \cdot h^2 \cdot \omega > 10 \tag{4.10}$$

Farajollahi *et al.* have measured the PEDOT linear conductivity ($\sigma_{i,PEDOT} = 25{\cdot}10^{-3}\, S{\cdot}m^{-1}$) and volumetric capacitance ($Cv = 10^8\, F \cdot m^{-3}$) of this polymer. Based on the obtained values and the PEDOT polymer model, a 30x4x0.05 mm^3 PEDOT polymer time constant for instance is $\tau = R_i \cdot C \cdot h^2 = 10\, s$[86]. This leads to a fractional approximation valid for $\omega > 1\, rad \cdot s^{-1}$ (see eq.4.10) [89].

According to the modelization work of Suhashi *et al.*, the approximation realized in eq.4.10 converges with a 1° maximal deviation of the phase for frequencies higher than 0.16 Hz. It increases to 5° deviation and less than 0.6 dB gain deviation for frequencies in the range]0.05, 0.16[Hz [89].

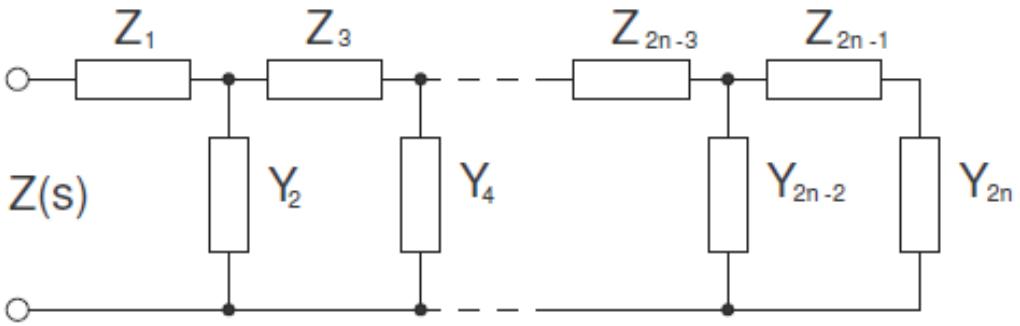

Figure 4.17 Electrical circuit for fractional operator approximation.

The expression of a trilayer polymer $1D$ transmission line impedance is then (adding

the second electrode and the PES):

$$Z_{1D}(s) = \frac{R_s \cdot C_{dl} \cdot \sqrt{R_i/C} \cdot s + R_s \cdot s^{0.5} + 2 \cdot \sqrt{R_i/C}}{C_{dl} \cdot \sqrt{R_i/C} \cdot s + s^{0.5}}$$

And the $2D$ RC transmission line equivalent impedance of the trilayer polymer is:

$$Z_{2D}(s) = \frac{2.R_e.L}{\sqrt{\frac{2 \cdot R_e \cdot L}{Z_{1D}(s)}} \cdot tanh(\sqrt{\frac{2 \cdot R_e}{Z_{1D}(s)}} \cdot L)}$$

The same approximation as in $Z_1(s)$ can be used to derive:

$$Z_{2D}(s) = \frac{\sqrt{2 \cdot R_e \cdot L} \cdot (C_{dl} \cdot \sqrt{R_i/C} \cdot s + s^{0.5})^{0.5}}{(R_s \cdot C_{dl} \cdot \sqrt{R_i/C} \cdot s + R_s \cdot s^{0.5} + 2 \cdot \sqrt{R_i/C})^{0.5}}$$

which is valid for $\omega > 3 \cdot 10^{-11}\, rad \cdot s^{-1}$. The electrolyte support resistance R_s, the PEDOT resistance per length unit R_e and the double layer capacitance interface of electrolyte support/conducting polymer C_{dl}, used for this calculation are based on the conductivity ($\sigma_{i,IPN} = 0.3\, S \cdot m^{-1}$) and capacitance measured by Farajollahi [86], applied to a 30x4x0.25 mm^3 polymer dimensions composed of two 30x4x0.05 mm^3 PEDOT polymer and an IPN PES.

In sensor mode, the deformation of the polymer leads to ions migration from a PEDOT electrode to another one. It results in a current between the two electrodes. The deformation is then proportional to the charge that migrate between the PEDOT electrodes through the electrolyte support with $q(s) = \frac{I(s)}{s}$. The transfer function between the measured voltage to the deformation can be written as:

$$H(s) = A \cdot s \cdot Z_{2D}(s)$$

Nevertheless, this transfer function is calculated assuming perfect conditions. We consider a perfect parallelepiped layers and a uniform repartition of capacitance and ionic conductivity all over the layers. However, besides conception and dimensional defaults, other parameters affect the system. The printed circuit used for the support applies an initial deformation to the trilayer polymer, and it introduces capacitive and resistive effects.

Fractional order identification

The fractional order identification system was realized using a variation of Levy's identification method. The identification model form is:

$$\hat{H}(S) = \frac{b_m \cdot s^{m \cdot q} + b_{m-1} \cdot s^{(m-1) \cdot q} + ... + b_1 \cdot s^q + b_0}{a_n \cdot s^{n \cdot q} + a_{n-1} \cdot s^{(n-1) \cdot q} + ... + a_1 \cdot s^q + a_0}$$

It is derived by minimizing the square norm E for all frequencies of interest:

$$\begin{aligned} E(\omega) = H(j\omega) \cdot (a_n \cdot (j\omega)^{n \cdot q} + a_{n-1} \cdot (j\omega)^{(n-1) \cdot q} + ... + a_1 \cdot (j\omega)^q + a_0) \\ -(b_m \cdot (j\omega)^{m \cdot q} + b_{m-1} \cdot (j\omega)^{(m-1) \cdot q} + ... + b_1 \cdot (j\omega)^q + b_0) \end{aligned}$$

where a_i and b_j are the coefficients of the transfer function model. ω is the input frequency . $H(j\omega)$ is the measured gain. n is the number of poles and m is the number of zeros of the model. Finally, q is the maximum common multiple of powers of s the Laplace parameter.

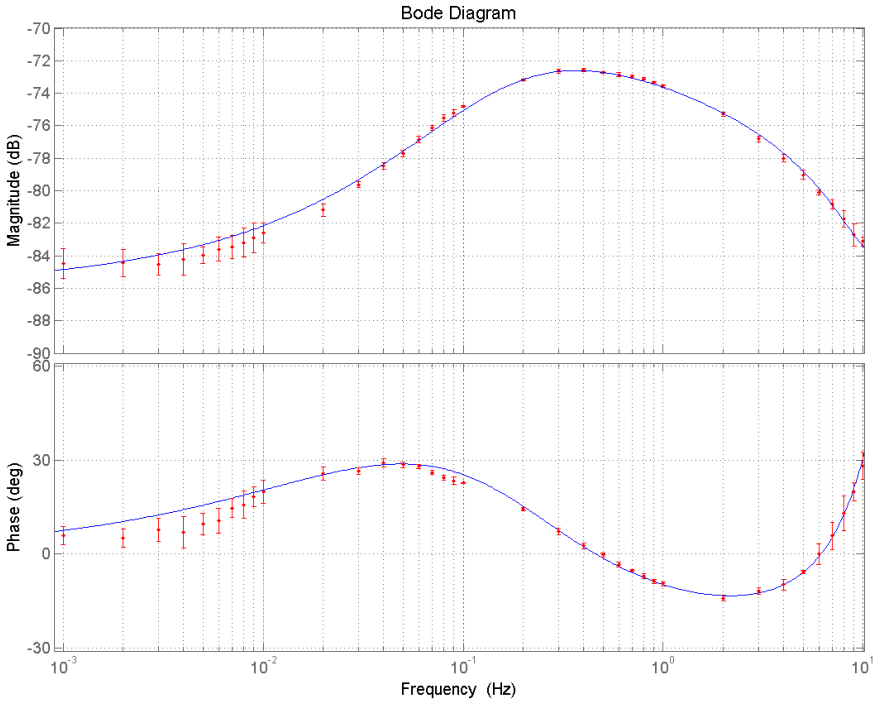

Figure 4.18 Bode diagram of the identified fractional transfer function. The identified model is in blue and the measurement data in red.

This identification technique is similar to the matlab ident toolbox. The fractional order model has a very high flexibility compared to the conventional common order models. This flexibility helps the model to converge for several combinations of poles

and zeros and maximum common multiples (mcm) of powers. However, keeping in mind that we want to determine the simplest model, we chose to fix the mcm of powers to $q = 0.5$ (we suppose a $1D$ transmission line impedance with $H(s) = A \cdot s \cdot Z_{1D}(s)$). This choice was prompted by the half slopes observed on the Bode diagram. Several numbers of poles and zeros were tested while looking for the minimum of poles and zeros that satisfy the imposed condition on the output model $J \geq 90\,\%$ ($J = 1 - \sum_{\omega} E(\omega)$ is the percent of confidence).

Finally, with $92.53\,\%$ of confidence an output model of 4 poles and 4 zeros was determined with the transfer function of the form:

$$H(S) = \frac{3.753 \cdot 10^{-6} \cdot s^2 - 3.297 \cdot 10^{-5} \cdot s^{1.5} + 2.817 \cdot 10^{-4} \cdot s + 2.124 \cdot 10^{-4} \cdot s^{0.5} + 8.084 \cdot 10^{-5}}{-9.197 \cdot 10^{-3} \cdot s^2 + 5.472 \cdot 10^{-2} \cdot s^{1.5} + 7.324 \cdot 10^{-1} \cdot s + 1.868 \cdot 10^{-1} \cdot s^{0.5} + 1}$$

Approximation to a high order system

The fractional order simulation can be realized in different manner. However, it is necessary to pass through a mathematical approximation of the identified fractional order system. It is indeed not possible to simulate this class of system with the same kind of algorithm we use for common order systems.

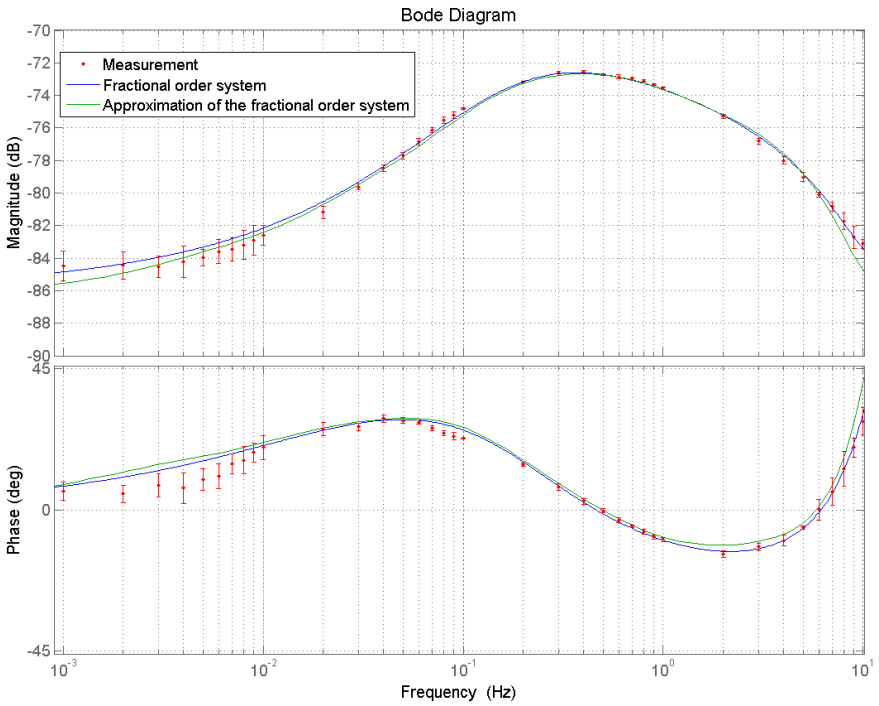

Figure 4.19 The fractional order approximation to a high common order system, and its assimilation to the estimated fractional order and the measurement data.

It is demonstrated that the fractional derivatives and integrals can be approximated by [150]:

$$C(s) = k \cdot s^v \approx k' \cdot \prod_{n=1}^{N} \frac{1 + \frac{s}{\omega_{zn}}}{1 + \frac{s}{\omega_{pn}}} \tag{4.11}$$

where k' is an adjusted coefficient based on k, v is the fractional real element in the range $[-1, 1]$, and ω_{nz} and ω_{np} are respectively the zeros and poles of the common order approximation of the fractional order system.

The Crone approximation (Crone is the French acronym for robust fractional order control) uses a recursive distribution of N poles and N zeros to approximate a fractional order system to a common order one. Based on this elementary approximation, one can approximate any fractional order system to a common order system by choosing the elementary number of pole and zero used in the crone approximation (approximation order). The approximation algorithm can be found on [150].

Several numbers of poles and zeros were tested for the approximation of the fractional order system. Finally, the best and simplest approximation (see fig.4.19) is a 9 poles and zeros common order system obtained by choosing 2 poles and zeros for the elementary decomposition of the fractional derivative $s^{0.5}$ (second order CRONE approximation). Of course, when it comes to integration on embedded systems, it is more suitable to use the state space representation of this model. In fact, the conversion of fractional order transfer function system into state space representation is identical to common order conversions. The matrix are extracted from the transfer function but the state space output is not the derivative of the input but its q order derivative with:

$$\begin{cases} D^q(x) = A \cdot x + B \cdot u \\ y = C \cdot x + D \cdot u \end{cases}$$

where x is the state vector, y the output parameter, u the input parameter, A the system matrix, B the input vector, C the output vector and D the feedthrough gain.

The fractional order integrator can be performed using the second order Crone approximation, or the Riemann-Liouville definition of non-integer integrator [151]:

$I^{\alpha}_{t_0} f(t) = \frac{1}{\Gamma(\alpha)} \cdot \int_{t_0}^{t} \frac{f(\tau)}{(t-\tau)^{1-\alpha}} \cdot d\tau$ [152] With $\Gamma(\alpha) = \int_0^{\infty} e^{-x} \cdot x^{\alpha-1} \cdot dx$

Simulation and results

As demonstrated in fig.4.19, the approximated model showed less than $1\,dB$ gain and $10°$ phase deviation from the measurement data. It can be considered a pretty good result for the model simulation.

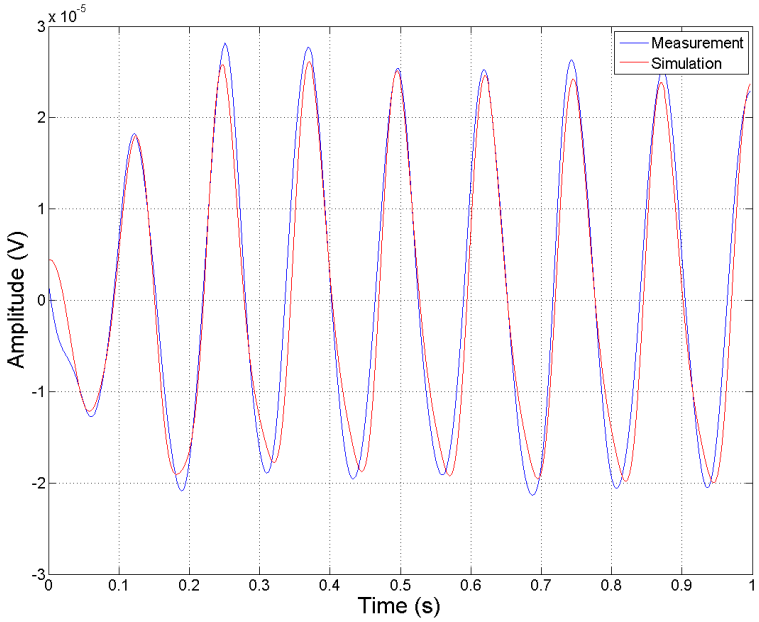

Figure 4.20 Fractional order simulation and measurement of the output voltage of the polymer submitted to a $5\,mm$ amplitude sinusoidal deformation at $8\,Hz$.

This model shows better results than the previous one. Moreover, the simulation for high frequency inputs provides pretty good results (see fig.4.20 for the $8\,Hz$ simulation). The simulation error using this model is lower than the system resolution in the identification frequency range. Moreover, the error in phase shift was highly reduced while using this new approach.

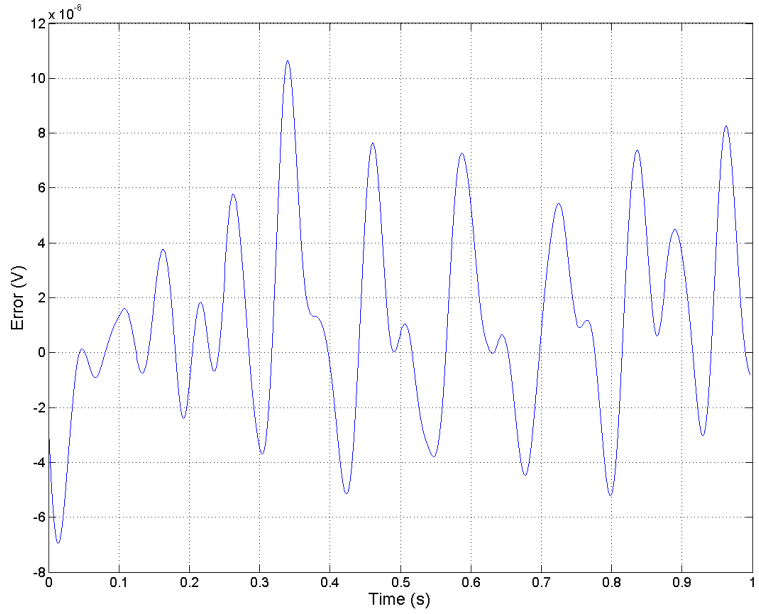

Figure 4.21 Error between the fractional order simulation and the measurement of the output voltage of the polymer submitted to a $8\,Hz$ frequency and a $5\,mm$ amplitude sinusoidal deformation at it's end.

4.5 Micrometer capabilities of the polymer

In this section, the studied interferometer in the previous chapters is used to highlight the micrometer capabilities of the interpenetrated trilayer polymer. The high sensitivity and resolution of the interferometer, associated to the high resolution of the ISP stage, are combined to perform the polymer deformation at microscale. Deviation angles of the polymer up to 1 $mrad$ are measured with the interferometer. By micrometer capabilities of the polymer, we mean the ability of the polymer to sense/actuate at micrometer scale.

4.5.1 Sensing part

System configuration

In this experiment, we want to characterize the polymer when it is excited at the micrometer scale. The translation stage used in this sub-section is the ISP-System voice coil motor translation stage. The interferometer of TeemPhotonics is used as a position sensor. The polymer extremity is driven by a mirror fixed on the translation stage. It is in a perpendicular position to the system main axis. The free end of the polymer passes through the slit of a mechanical part fixed on the mirror. The translation stage drives both the mirror and the piece, and thereby apply a micrometric scale deformation on the polymer (see fig.4.22).

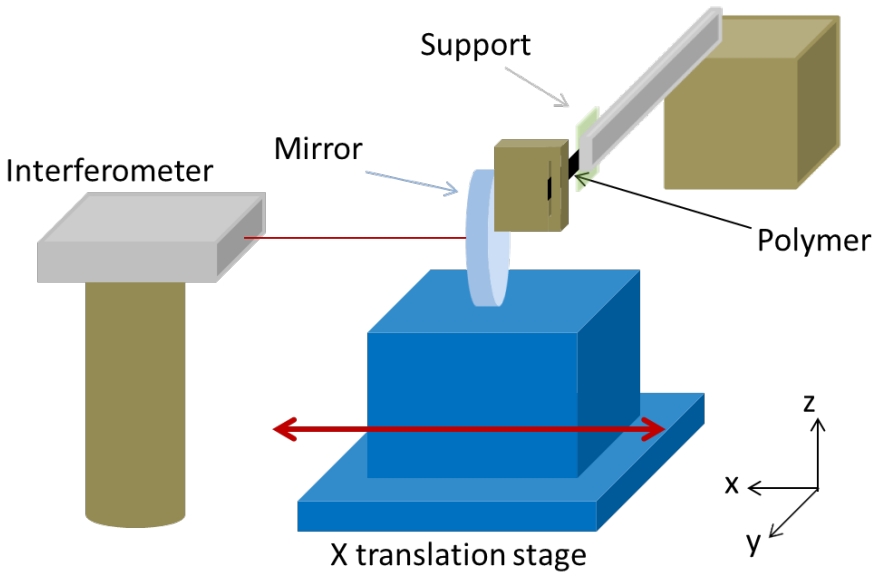

Figure 4.22 Experimental setup to evaluate the sensor capabilities at microscale.

In this experiment, a sine wave of a 0.5 Hz with a 10 μm amplitude is applied. The sample has a section of 0.25x4 mm^2. The length is set to 25 mm. The frequency is

chosen because of the maximum gain that appears on the Bode diagram around $0.5\,Hz$. The amplitude of $10\,\mu m$ may be seen as a limit because, under this value, the signal to noise ratio becomes very small.

Analysis and results

Fig.4.23 represents the signal measured between the 2 electrodes. A $40\,Hz$ low pass filter is applied to it. It is obvious that the signal to noise ratio is very small when a slight deformation is applied to the tip of the polymer. In this experiment, the deformation is only of $0.0008\,\%$ and makes the signal level too low to be observed. However, the experiment was realized several times with the same configuration. A FFT of a $10\,min$ window is computed for each measurement to measure the $0.5\,Hz$ main component.

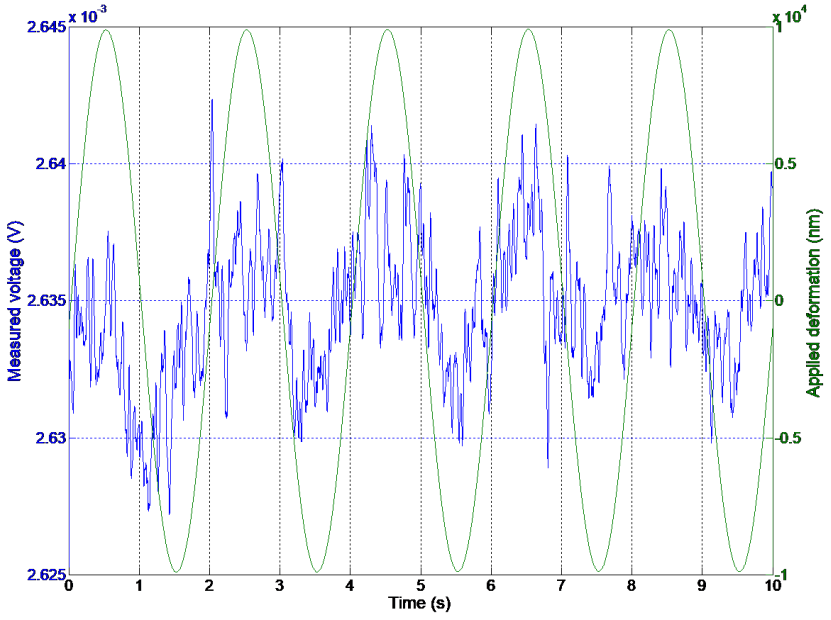

Figure 4.23 Sensor output under a sine wave deformation (frequency of $0.5\,Hz$ and amplitude of $5\,\mu m$).

Five similar measurements are realized. The means of the obtained FFTs is computed and plotted, and the awaited amplitude peak at $0.5Hz$ was clearly highlighted. As demonstrated in fig.4.24, the output is of $1.203\,\mu V$. This experiment demonstrates the micrometer capabilities of the polymer since an output voltage is measured after a micrometric displacement was made ($10\,\mu m$). However, it is very unlikely that we can measure an output when the displacement is lower than $10\,\mu m$. A first solution to increase the system sensitivity, could be to modify the support since it acts like an antenna. Another solution would be to change the polymer dimensions.

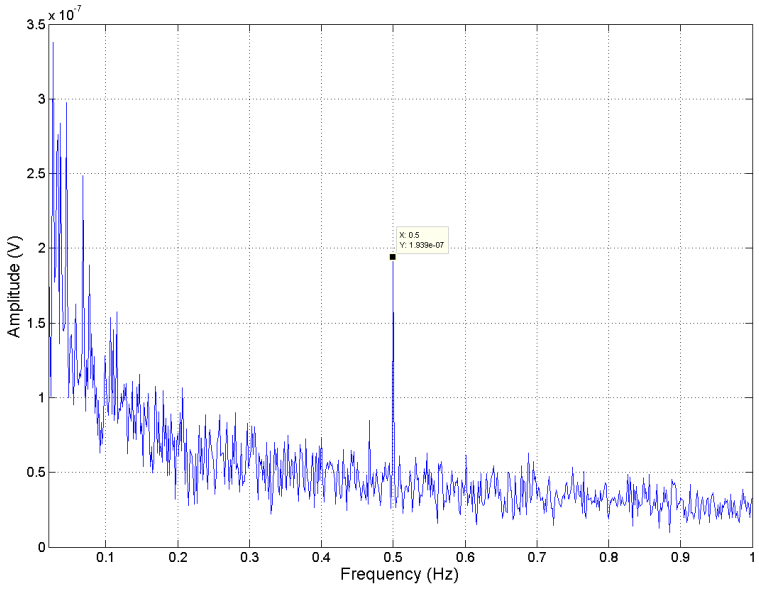

Figure 4.24 FFT when a sine wave deformation is applied (frequency of $0.5\,Hz$ and amplitude of $10\,\mu m$). A $10\,min$ window is selected.

4.5.2 Actuating part

Experimental setup

For this experiment, a mirror of $145\,mg$ with a diameter of $5\,mm$ is glued at the extremity of a polymer. which section is $0.25\text{x}5\,mm^2$ and length is $10\,mm$. The system {polymer/mirror} is then fixed in a vertical position to minimize the gravity effect. We choose to reduce the length to minimize the system free oscillation amplitude. The interferometer is used to measure the displacements of the mirror while a very low voltage is applied between the polymer electrodes to realize very slight deformations. Therefore, the reflected beam is still retro or partly retro-injected into the interferometer output lens (see fig.4.25).

The polymer is actuated using a $24-bits$ digital to analog card NI $PXI-4461$ plugged to a $PXIe-1071$ rack including a $PXIe-8133$ controller from National Instruments. The controller is programmed to generate a very low frequency square signal of $1\,mHz$ and a 1 to $10\,mV$ amplitude. The low frequency is made because of the low time response of the system. The system (applied voltage/measured displacement) acts like a RC line with a $92\,s$ time constant (cf fig.4.26). The amplitude range is selected with respect to the system noise ($100\,\mu V$ peak to peak) and to guarantee that the beam is still retro-injected. For example, an input of $15\,mV$ leads to a high deformation and the loss of the retro-injected signal.

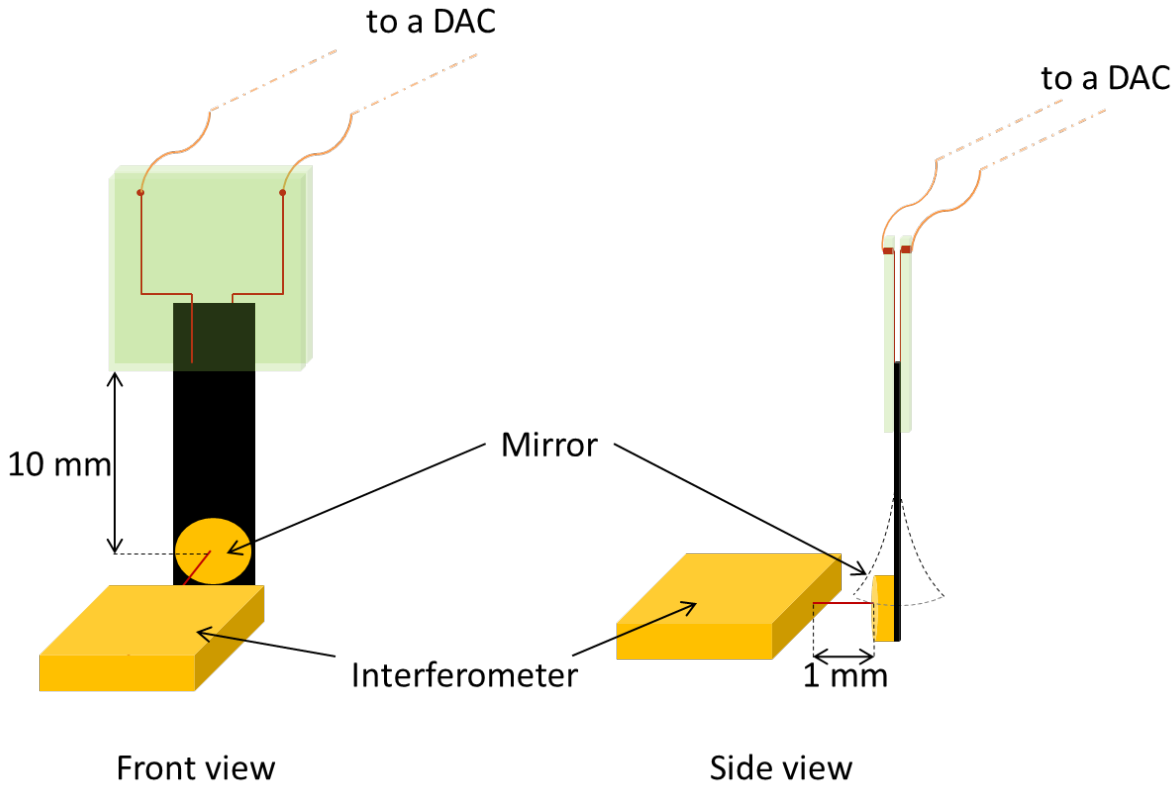

Figure 4.25 Experimental setup for micrometer capabilities with the actuator mode.

The generated signal is used to actuate the polymer. The polymer is serially connected to a $47\,\Omega$ resistor (R) to protect it from high current. The generated square signal can be time decomposed into several step signals which is very useful to identify a linear system transfer function. A NI $PXI-4471$ acquisition board is also used to measure the output voltage of the DAC board and between the resistor and the interferometer bounds electrodes. The main purpose is to measure the current circulating through the polymer and the actual voltage between the two electrodes of the polymer. All signals are recorded for post-processing.

Nevertheless, Fig.4.26 demonstrates the square signal generated by the DAC card (E), and the measured voltage between the polymer electrodes (Ep). Based on this measurement, one can see that the voltage at the polymer bounds response to the applied square signal is a first order (one pole, one zero) step answer. Moreover, the system configuration is a voltage divider bridge configuration. This leads to the identified transfer function:

$$\frac{E_p}{E} = \frac{1+96s}{1+100.91s} = \frac{Z(s)}{Z(s)+R}$$

where s is the Laplace variable, R the serial $47\,\Omega$ resistor and $Z(s)$ the polymer impedance.

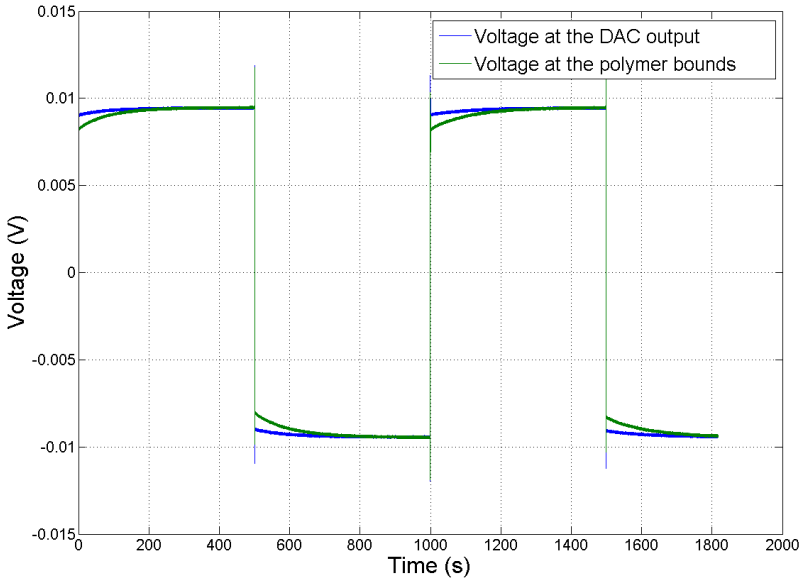

Figure 4.26 Output voltages at the DAC output (blue) and at the polymer electrodes (green).

The polymer/mirror impedance can be deduced from the computed transfer function, the obtained impedance is a RC line equivalent impedance:

$$Z(s) = 908.83 + \frac{1}{0.106s}$$

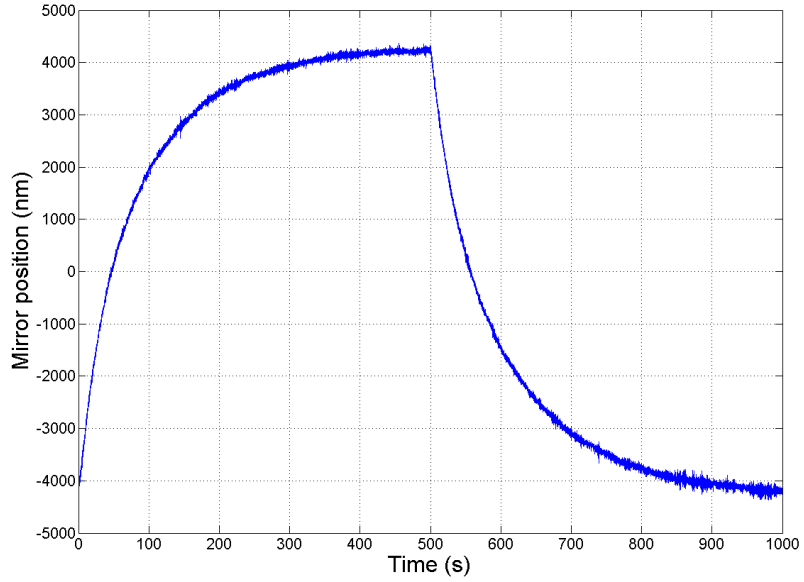

Figure 4.27 Measured mirror position over one actuating period.

Fig.4.27 demonstrates the computed mirror position over one actuating period. The obtained curve is similar to a charge/discharge of a capacitor with respect to the previous electrical data analysis. Indeed, if the polymer is a ionic conductor, if the polymer

resistive effect is assimilated to the ions migration throw the polymer electrolyte support, than the capacitive effect is due to the insertion/expulsion of solvated ions in the Electronically Conductive Polymers electrodes. This ions insertion/expulsion leads to the expansion/compression of the polymer electrodes and then produce the bending. The time constant of the exponential behavior of the measured mirror position is 66.7 s.

The time response of the polymer/mirror system to a step signal is several times higher when compared to the polymer free response without a mirror. The mass of the mirror is similar to the mass of polymer and there is a price to pay in terms of time response when high masses are dragged while moving [84].

The optical power fluctuation

Also, once the interferometer measurements signals are acquired, one should be able to extract the information on the mobile mirror position by fitting the curve described by Mes_1 and Mes_2 to an ellipse model, and determining the instantaneous position angles in the ellipse while the mobile mirror is moving. However, in the particular case of this experiment the interference ellipse parameters are not constant due to the retro-injected power fluctuation, resulting from the mirror reflection and the input/output lens transmission coefficients dependency on the laser beam incidence angle. In fact, the mirror at the extremity of the polymer doesn't translate, but rotate in consequence to the polymer bending.

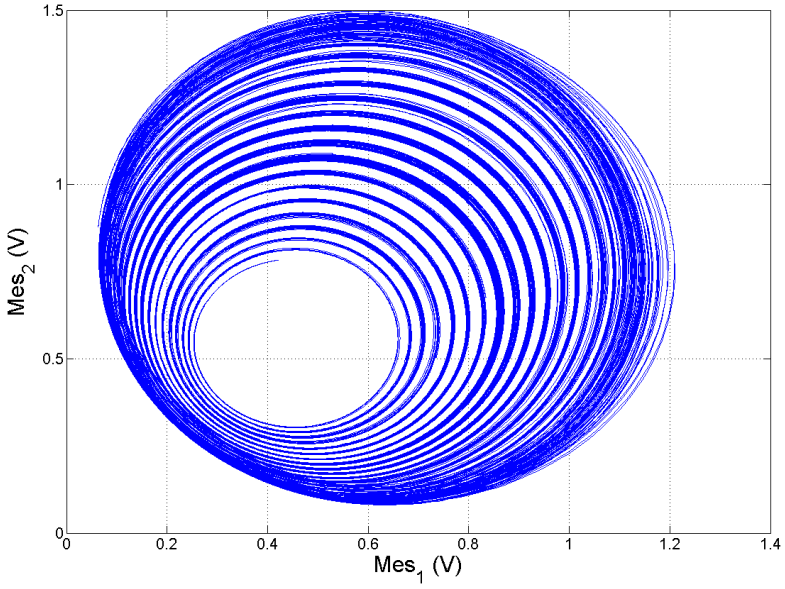

Figure 4.28 Effect of the optical retroinjected power fluctuation on the ellipse described by the interferometric measurement signals.

Fig.4.28 shows the effect of the optical retro-injected power fluctuation on the ellipse described by the interferometric measurement signals, indeed, as expect (see eq.2.7) the ellipse center as well as both radius are affected by the polymer bending and then the mirror rotation. In the case of conventional interferometers the obvious solution is to use a real-time adaptive fitting algorithm to adapt the ellipse parameters all over the acquisition or simply divide the measurements signals into several parts and estimate the ellipse parameters in the different time intervals. However, studies on the interference ellipse real-time fitting showed that the fitting convergence is conditioned by the number of data introduced to the algorithm [128], indeed, at least the quarter of the ellipse must be used to see the algorithm converge properly, but due to the reflected optical path constant change of incidence angle all along the experiment this kind of fitting algorithm is not adapted.

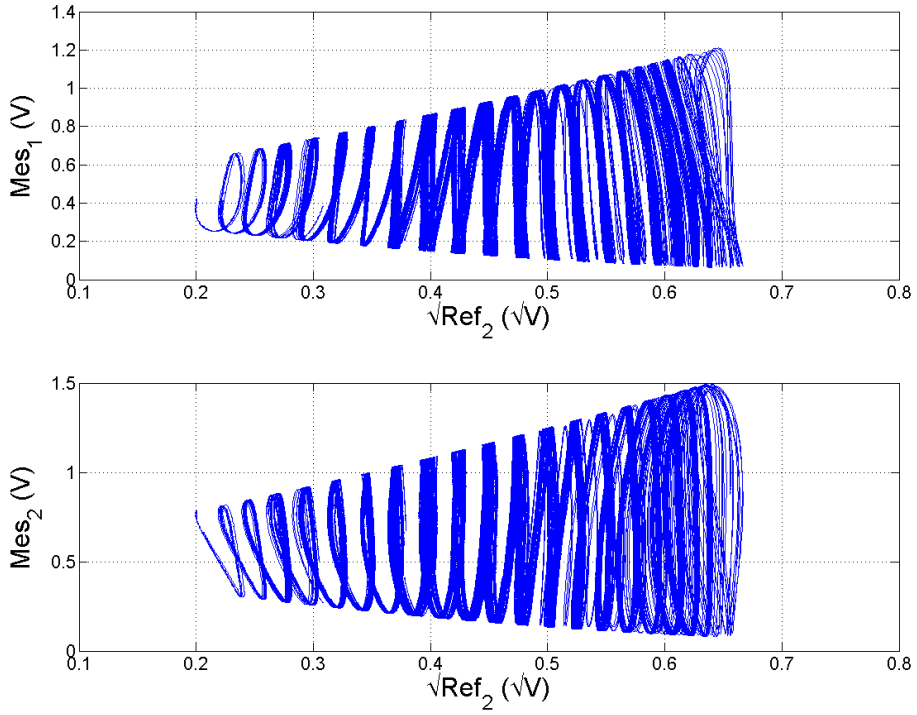

Figure 4.29 Effect of the optical retroinjected power fluctuation on the ellipse described by the interferometric measurement signals.

However, in the case of the picomove interferometer, the specific normalization of the measurements signals toward the output and the retro-injected optical power still converge to a normalized circle, and the optical path length difference can be properly computed, just by knowing the input/output Ks parameters of the optical chip. In fact, conversely to the ellipse parameters those parameters aren't affected by the rotational component of the mobile mirror motions. Finally, this experiment is an ideal example

to demonstrate the robustness of this interferometer toward the retro-injected optical power fluctuation.

Data post-processing and results

Fig.4.29 shows the measurement signals with respect to the square root of the Ref_2 signal, in fact, using eq.2.7 it is possible to fit those curves using the measurement signals maximums or minimums for each ellipse, in this work we did both and computed the mean values of the Ks input/output parameters resulting from both fits using eq.2.9.

Fig.4.30 shows the normalized ellipse to a circle after computation of the Ks parameters and normalization of the measurement signals. The mirror displacement was computed using eq.3.9 and the algorithm alg.3.1.

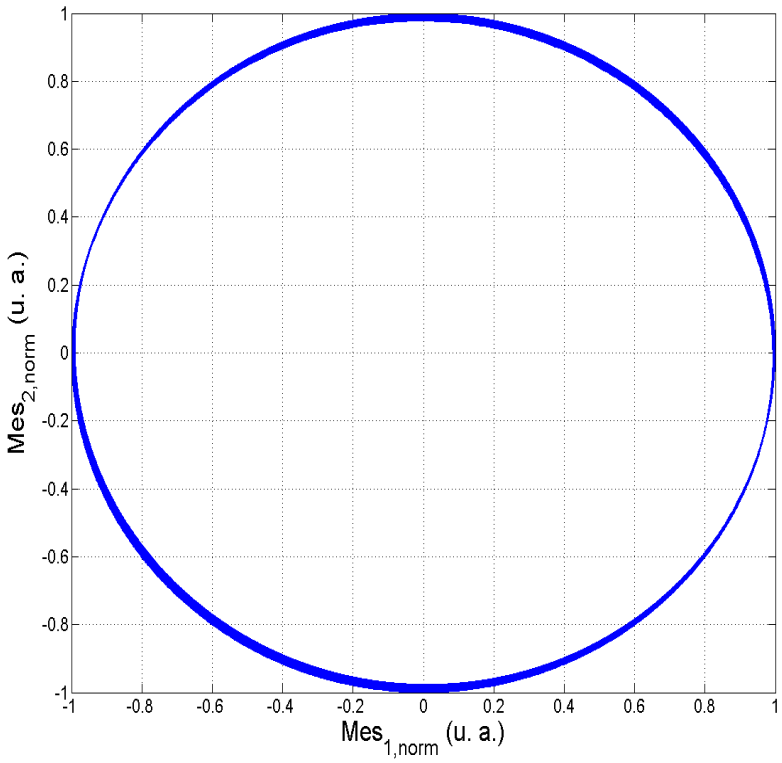

Figure 4.30 Normalized Lissajou ellipse into circle.

The characterizations of this kind of polymer realized by Farajollahi *et al.* demonstrated that the actuated polymer shape can be approximated to a circle arc [86], the mirror at the polymer end motion can then be considered as pure rotation. Of course, the realized rotation angle is very slight in our experiment, due to the laser retro-injection in the input/output interferometer lens restriction.

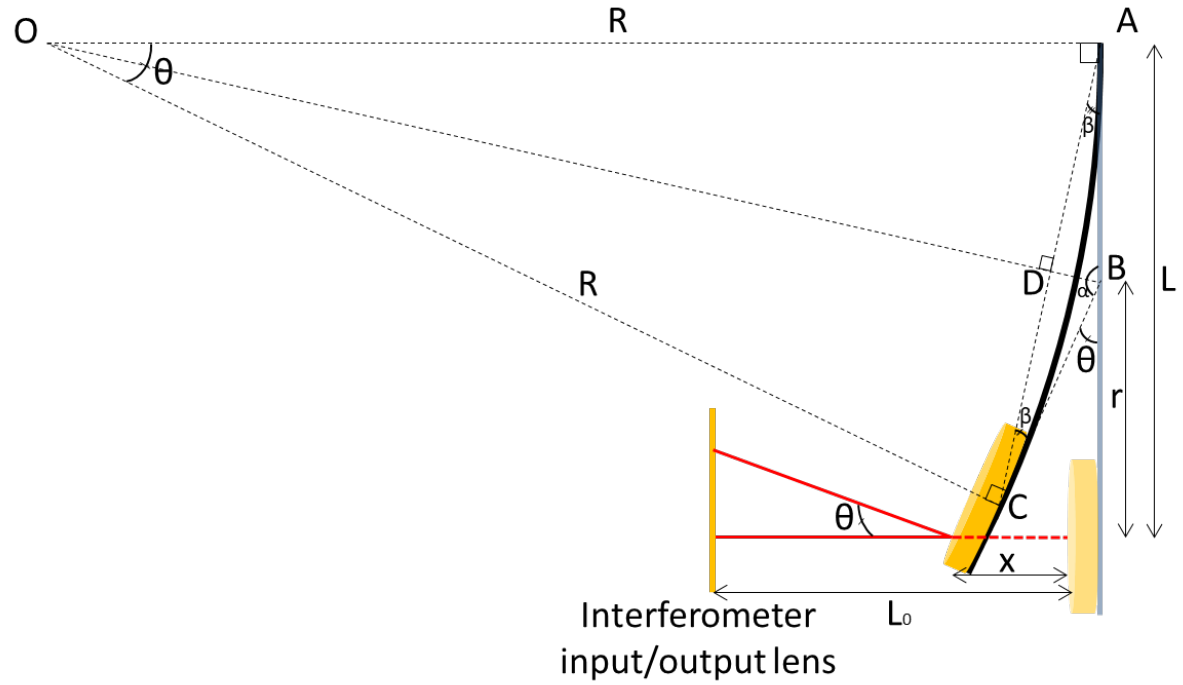

Figure 4.31 Effect of the rotation when the polymer is moving. θ is the rotation angle, R is the distance to the axis of rotation, r is the assimilated Abbe offset, L_0 is the initial optical path length and x the measured mirror displacement.

Nevertheless, the realized measurement can be assimilated to the so called Abbe error. It occurs when a rotation is combined to a shift between the measurement point and the rotation origin (Abbe offset). Let us consider an Abbe offset 'r' and a rotation angle 'θ'. In fig.4.31 the abbe offset can be expressed by $r = L - AB$, with $AB = \frac{AC}{2.cos(\theta/2)}$ ($\beta = \frac{\theta}{2}$), $AC = 2 \cdot R \cdot sin(\frac{\theta}{2})$ and $R = \frac{L}{\theta}$.

The displacement of the mirror along the optical axis x, is:

$$x = r \cdot tan(\theta) = L \cdot (1 - \frac{1}{\theta} \cdot tan(\frac{\theta}{2})) \cdot tan(\theta)$$

The measured displacement x_m is an optical path difference that is:

$$x_m = \frac{1}{2} \cdot (2 \cdot L_0 - (1 + \frac{1}{cos(\theta)}) \cdot (L_0 - x))$$

The first order approximation ($sin(\theta) = \theta$ and $cos(\theta) = 1$) leads to $x_m = x \approx \frac{L \cdot \theta}{2}$.

The second order approximation ($sin(\theta) = \theta$ and $cos(\theta) = 1 - \frac{\theta^2}{2}$) can be used to estimate the measurement error:

$$\xi = |\frac{x - x_m}{x}| = \frac{(L_0 - x) \cdot \theta^2}{2 \cdot x \cdot (2 - \theta^2)}$$

This error is quite small (the reflection coefficient of the mirror is not considered). For an initial optical path length $L_0 = 1\,mm$, a polymer with a length of $10\,mm$ and a maximum measured displacement of $5\,\mu m$, the relative error is only of $1.24 \cdot 10^{-5}$.

This experiment shows the bending capabilities of the polymer at the micrometer scale. Moreover, it demonstrates a linearity of the realized deformations toward the different applied voltage in the range $[1{,}10]\,mV$ with a static gain of $445\,\mu m/V$ while supporting the mirror mass.

4.6 Conclusion

In this chapter, the IEAP was assimilated to a cantilever with a fixed and a free end. The mechanical characterization has been recalled to point out the key parameters of the system, namely the stiffness and the force as well as their relationship. The conducting interpenetrating polymer networks IEAP was electro-mechanically characterized. The sensor mode frequency response of the IEAP was studied to define the sensor bandwidth and resolution. Moreover, a transfer function was identified for the sensor mode. It overcomes the gain and phase shift errors induced by the frequency response of the IEAP which can be assimilated to a passband filter. Finally, the micrometric capabilities of the IEAP were demonstrated in both actuating and sensing modes, using experimental setups based on the previously presented interferometer. The robustness of this interferometer against power fluctuation was highlighted and exploited in the micrometer actuation demonstration.

Conclusion

The investigation of the characteristics, particularities and potential of an interferometer with a fully embedded optical chip is presented in this thesis. The interferometer is used to characterize an innovative transducer in sensing mode. The presented interferometer is compact and highly integrable. It demonstrates that low sensitivity to external disturbances and ease of use can be achieved. It exhibits high stability, robustness to parasite rotations and picometric performances. The electro-active polymer used for the experiment is capable of both sensing and actuating. Its main advantages, compared to piezoelectrics transducer, are its low voltage actuation ($< 2\,V$), its high bending performances, as well as its flexibility.

The studied interferometer has a modified Young/Michelson architecture. Its main originality is the measurement of the injected and retro-injected laser beam power. This reference signals are used to normalize the interferometric measurements in quadrature signals. This specificity makes it robust against environmental disturbances and retro-injected power fluctuations. The robustness was highlighted with micrometer scale rotation motion measurements. The sensor was fully characterized and demonstrated very good static and dynamic performances for both short and long stroke displacements. Finally, its sensitivity to temperature variation was evaluated and it was coupled to a weather station for real time correction of the laser wavelength.

The interferometer was used for the characterization of an electro-active polymer transducer. This polymer was studied assuming a cantilever beam configuration. The polymer transducing sensor mode function was estimated (transversal displacement at its extremity as an input and voltage between its two electrodes as output). Finally, the transducer micrometer scale capabilities were demonstrated, by measuring a $10\,\mu m$ transversal displacement of the tip in sensor mode, and achievement of few micrometer deformation of its extremity on actuator mode. In both cases the displacement measurement was performed with the interferometer.

In next future, to improve the studied interferometer, the development of a chip which may be used with a red source instead of the infrared one would allow the use

of ultra stable sources. It would allow an easier set up. This is particularly true for applications like AFM scanning when the focus of the beam on the cantilever is difficult. In the FUI Multiss project, a new version of this interferometer was developed, which is vacuum compatible allowing the integration in a vacuum chamber (chambers of electronic microscopes, for example). Moreover, multi beams interferometer chip development is also an interesting perspective, because it would allow parasite rotation measurement and mirror orientation estimation.

By the way, this sensor is dedicated to integration in nanopositioning systems. The vacuum compatible version of this interferometer has been integrated to a NLS serie double axis system by our partner ISP System through the project Multiss (Multiscale Interferometric Scanning Stage). However, the developed nanopositioning system suffers from interferometric measurement errors for high velocity displacements. This is likely the results of the embedded acquisition electronics relatively low sampling frequency. Indeed, the integrated positioning system is able to achieve more than $10\,mm \cdot s^{-1}$ displacement speed. Development of higher sample frequency embedded acquisition electronics to compensate from this issue is intended.

Unlike its microscale performances in actuator mode, the integration of this electro-active interpenetrated network polymer at microscale in sensor mode requires a deep adaptation of the system. In the presented work, the capability to sense micrometer scale deformation was demonstrated. However, the realized experiment at this scale showed poor signal to noise ratio. An improvement of the polymer/support measurement contact area is necessary to reduce the noise level. The study and characterization of a new generation of electro-active polymers may open to the development and the integration of new polymer transducers based devices in the micro/nanotechnology world.

This transducer behavior when it has to support different mass values might be identified. The effect of an embedded mass strongly influences its dynamical performances when the polymer is actuated. For example, this could be realized with the interferometer while using a gold deposit on the PEDOT electrodes.

Finally, the characterization of the polymer transducer is dedicated to an integration in micromanipulator grippers. In our team, another PhD student (C.-J. Peng) is working on the design of a micro-gripper based on polymer transducers fingers. For example, an active finger operating on actuator mode; and a passive finger operating on sensor mode.

List of Figures

List of Tables

List of Algorithms

Scientific curriculum vitae

International peer-reviewed journals

- Walid Adel MERZOUK, Barthélemy CAGNEAU, Florent GARDILLOU Khalid HILOUANE and Luc CHASSAGNE. Highly compact and easy-to-use optical chip interferometer with picometric performances. *Review of Scientific Instruments*, 2016, vol. 87, no 10, p. 103103.

- Badreddine RATNI, Walid Adel MERZOUK, André DE LUSTRAC, Serge VILLERS, Gérard-Pascal PIAU and Shah Nawaz BUROKUR. Design of phase-modulated metasurfaces for beam steering in Fabry–Perot cavity antennas. *IEEE Antennas and Wireless Propagation Letters*, 2017, vol. 16, p. 1401-1404.

International peer-reviewed conferences

- Walid Adel MERZOUK, Badreddine RATNI, Shah Nawaz BUROKUR and André DE LUSTRAC. Modeling of beam steering from a phase-gradient metasurface. In : *Advanced Electromagnetic Materials in Microwaves and Optics (METAMATERIALS)*, 2015 9th International Congress on. IEEE, 2015. p. 388-390.

- Walid Adel MERZOUK, Barthélemy CAGNEAU, Khalid HILOUANE, Luc CHASSAGNE and Florent GARDILLOU. An affordable and easy-to-use interferometer with a dedicated acquisition system. In : *SENSORS, 2016 IEEE. IEEE, 2016*. p. 1-3.

Bibliography

[1] R. Feyman, "There is plenty of room at the bottom: an invitation to enter a new field of physics," in *conférence prononcée au congrès annuel of American Physical Society, California Institute of Technology, Pasadena*, vol. 29, 1959, pp. 5–22.

[2] G. Binnig, H. Rohrer, C. Gerber, and E. Weibel, "Surface studies by scanning tunneling microscopy," *Physical review letters*, vol. 49, no. 1, p. 57, 1982.

[3] G. Binnig, C. F. Quate, and C. Gerber, "Atomic force microscope," *Physical review letters*, vol. 56, no. 9, p. 930, 1986.

[4] H. Zheng, S.-Y. Xu, G. Bian, C. Guo, G. Chang, D. S. Sanchez, I. Belopolski, C.-C. Lee, S.-M. Huang, X. Zhang *et al.*, "Atomic-scale visualization of quantum interference on a weyl semimetal surface by scanning tunneling microscopy," *ACS nano*, vol. 10, no. 1, pp. 1378–1385, 2016.

[5] Y. Zhang, S.-Y. Li, H. Huang, W.-T. Li, J.-B. Qiao, W.-X. Wang, L.-J. Yin, K.-K. Bai, W. Duan, and L. He, "Scanning tunneling microscopy of the π magnetism of a single carbon vacancy in graphene," *Physical review letters*, vol. 117, no. 16, p. 166801, 2016.

[6] E. Stolyarova, K. T. Rim, S. Ryu, J. Maultzsch, P. Kim, L. E. Brus, T. F. Heinz, M. S. Hybertsen, and G. W. Flynn, "High-resolution scanning tunneling microscopy imaging of mesoscopic graphene sheets on an insulating surface," *Proceedings of the National Academy of Sciences*, vol. 104, no. 22, pp. 9209–9212, 2007.

[7] B. Schuler, G. Meyer, D. Peña, O. C. Mullins, and L. Gross, "Unraveling the molecular structures of asphaltenes by atomic force microscopy," *Journal of the American Chemical Society*, vol. 137, no. 31, pp. 9870–9876, 2015.

[8] K. Haase and A. E. Pelling, "Investigating cell mechanics with atomic force microscopy," *Journal of The Royal Society Interface*, vol. 12, no. 104, p. 20140970, 2015.

[9] L. Gross, F. Mohn, N. Moll, P. Liljeroth, and G. Meyer, "The chemical structure of a molecule resolved by atomic force microscopy," *Science*, vol. 325, no. 5944, pp. 1110–1114, 2009.

[10] A. Sinno, P. Ruaux, L. Chassagne, S. Topçu, Y. Alayli, G. Lérondel, S. Blaize, A. Bruyant, and P. Royer, "Enlarged atomic force microscopy scanning scope: Novel sample-holder device with millimeter range," *Review of Scientific Instruments*, vol. 78, no. 9, p. 095107, 2007.

[11] B. Bhushan, *Springer handbook of nanotechnology*. Springer, 2017.

[12] R. Bennewitz, "Friction force microscopy," in *Fundamentals of Friction and Wear on the Nanoscale*. Springer, 2015, pp. 3–16.

[13] N. S. Malvankar, S. E. Yalcin, M. T. Tuominen, and D. R. Lovley, "Visualization of charge propagation along individual pili proteins using ambient electrostatic force microscopy," *Nature nanotechnology*, vol. 9, no. 12, p. 1012, 2014.

[14] M. K. Phani, A. Kumar, W. Arnold, and K. Samwer, "Elastic stiffness and damping measurements in titanium alloys using atomic force acoustic microscopy," *Journal of Alloys and Compounds*, vol. 676, pp. 397–406, 2016.

[15] C. Degen, "Scanning magnetic field microscope with a diamond single-spin sensor," *Applied Physics Letters*, vol. 92, no. 24, p. 243111, 2008.

[16] Y. Kawakami, A. Kaneta, A. Hashiya, and M. Funato, "Impact of radiative and nonradiative recombination processes on the efficiency-droop phenomenon in in x ga 1- x n single quantum wells studied by scanning near-field optical microscopy," *Physical Review Applied*, vol. 6, no. 4, p. 044018, 2016.

[17] G. Lérondel, A. Sinno, L. Chassagne, S. Blaize, P. Ruaux, A. Bruyant, S. Topcu, P. Royer, and Y. Alayli, "Enlarged near-field optical imaging," *Journal of applied physics*, vol. 106, no. 4, p. 044913, 2009.

[18] S. Gomès, A. Assy, and P.-O. Chapuis, "Scanning thermal microscopy: A review," *physica status solidi (a)*, vol. 212, no. 3, pp. 477–494, 2015.

[19] T. Sun, Y. Yu, B. J. Zacher, and M. V. Mirkin, "Scanning electrochemical microscopy of individual catalytic nanoparticles," *Angewandte Chemie International Edition*, vol. 53, no. 51, pp. 14 120–14 123, 2014.

[20] C. Maragliano, S. Lilliu, M. Dahlem, M. Chiesa, T. Souier, and M. Stefancich, "Quantifying charge carrier concentration in zno thin films by scanning kelvin probe microscopy," *Scientific reports*, vol. 4, p. 4203, 2014.

[21] C. Williams and H. Wickramasinghe, "Scanning chemical potential microscope: A new technique for atomic scale surface investigation," *Journal of Vacuum Science & Technology B: Microelectronics and Nanometer Structures Processing, Measurement, and Phenomena*, vol. 9, no. 2, pp. 537–540, 1991.

[22] D. Momotenko, K. McKelvey, M. Kang, G. N. Meloni, and P. R. Unwin, "Simultaneous interfacial reactivity and topography mapping with scanning ion conductance microscopy," *Analytical chemistry*, vol. 88, no. 5, pp. 2838–2846, 2016.

[23] S. Aghaei, P. Andrei, and M. Hagmann, "Extracting impurity locations using scanning capacitance microscopy measurements," *Advances in Electrical and Computer Engineering*, vol. 16, no. 3, pp. 3–8, 2016.

[24] "The scanning tunneling microscope," https://www.iap.tuwien.ac.at/www/surface/stm_gallery/stm_schematic, accessed: 2018-10-31.

[25] A. Eberle, S. Mikula, R. Schalek, J. Lichtman, M. K. Tate, and D. Zeidler, "High-resolution, high-throughput imaging with a multibeam scanning electron microscope," *Journal of microscopy*, vol. 259, no. 2, pp. 114–120, 2015.

[26] K. Smith and C. Oatley, "The scanning electron microscope and its fields of application," *British Journal of Applied Physics*, vol. 6, no. 11, p. 391, 1955.

[27] A. V. Crewe, M. Isaacson, and D. Johnson, "A simple scanning electron microscope," *Review of Scientific Instruments*, vol. 40, no. 2, pp. 241–246, 1969.

[28] A. Feist, K. E. Echternkamp, J. Schauss, S. V. Yalunin, S. Schäfer, and C. Ropers, "Quantum coherent optical phase modulation in an ultrafast transmission electron microscope," *Nature*, vol. 521, no. 7551, p. 200, 2015.

[29] A. Crewe, J. Wall, and L. Welter, "A high-resolution scanning transmission electron microscope," *Journal of Applied Physics*, vol. 39, no. 13, pp. 5861–5868, 1968.

[30] M. Haider, H. Rose, S. Uhlemann, B. Kabius, and K. Urban, "Towards 0.1 nm resolution with the first spherically corrected transmission electron microscope," *Microscopy*, vol. 47, no. 5, pp. 395–405, 1998.

[31] B. Inkson, "Scanning electron microscopy (sem) and transmission electron microscopy (tem) for materials characterization," in *Materials characterization using nondestructive evaluation (NDE) methods*. Elsevier, 2016, pp. 17–43.

[32] "Electron microscope," https://en.wikipedia.org/wiki/Electron_microscope, accessed: 2018-10-31.

[33] T. Fukuda, M. Nakajima, P. Liu, and M. R. Ahmad, "Bringing the nanolaboratory inside electron microscopes," *IEEE Nanotechnology Magazine*, vol. 2, no. 2, 2008.

[34] C. Shi, D. K. Luu, Q. Yang, J. Liu, J. Chen, C. Ru, S. Xie, J. Luo, J. Ge, and Y. Sun, "Recent advances in nanorobotic manipulation inside scanning electron microscopes," *Microsystems & Nanoengineering*, vol. 2, p. 16024, 2016.

[35] S. Mazerolle, J.-M. Breguet, A. Steinecker, J. Agnus, R. Pérez, J. Michler *et al.*, "Nanomanipulation in a scanning electron microscope," *Journal of Materials Processing Technology*, vol. 167, no. 2-3, pp. 371–382, 2005.

[36] T. Sulchek, R. Hsieh, J. Adams, G. Yaralioglu, S. Minne, C. Quate, J. Cleveland, A. Atalar, and D. Adderton, "High-speed tapping mode imaging with active q control for atomic force microscopy," *Applied Physics Letters*, vol. 76, no. 11, pp. 1473–1475, 2000.

[37] X. Wang, L. Vincent, M. Yu, Y. Huang, and C. Liu, "A thermally actuated three-probe nanomanipulator for efficient handling of individual nanostructures," in *Micro Electro Mechanical Systems, 2004. 17th IEEE International Conference on.(MEMS)*. IEEE, 2004, pp. 442–445.

[38] N. A. Weir, D. P. Sierra, and J. F. Jones, "A review of research in the field of nanorobotics," *Sandia Report*, 2005.

[39] R. Thalmann, F. Meli, and A. Küng, "State of the art of tactile micro coordinate metrology," *Applied Sciences*, vol. 6, no. 5, p. 150, 2016.

[40] J. A. Kramar, "Nanometre resolution metrology with the molecular measuring machine," *Measurement Science and Technology*, vol. 16, no. 11, p. 2121, 2005.

[41] P. Yang, T. Takamura, S. Takahashi, K. Takamasu, O. Sato, S. Osawa, and T. Takatsuji, "Development of high-precision micro-coordinate measuring machine: Multi-probe measurement system for measuring yaw and straightness motion error of xy linear stage," *Precision Engineering*, vol. 35, no. 3, pp. 424–430, 2011.

[42] A. Lewis, S. Oldfield, and G. Peggs, "The npl small cmm-3-d measurement of small features," *WIT Transactions on Engineering Sciences*, vol. 34, 1970.

[43] Q. Huang, K. Wu, C. Wang, R. Li, K.-C. Fan, and Y. Fei, "Development of an abbe error free micro coordinate measuring machine," *Applied Sciences*, vol. 6, no. 4, p. 97, 2016.

[44] A. Moers, M. C. van Riel, and E. J. Bos, *Design and verification of the Trinano ultra precision CMM.* Universitätsbibliothek Ilmenau, 2011.

[45] A. Küng, F. Meli, and R. Thalmann, "Ultraprecision micro-cmm using a low force 3d touch probe," *Measurement Science and Technology*, vol. 18, no. 2, p. 319, 2007.

[46] G. Jäger, E. Manske, T. Hausotte, H.-J. Büchner, R. Grünwald, and W. Schott, "Nanomeasuring technology–nanomeasuring machine," in *ASPE 2001 Annual Meeting.* Washington, D. C: Nov, 2001, pp. 1–10.

[47] G. Jäger, E. Manske, T. Hausotte, A. Müller, and F. Balzer, "Nanopositioning and nanomeasuring machine npmm-200âa new powerful tool for large-range micro-and nanotechnology," *Surface Topography: Metrology and Properties*, vol. 4, no. 3, p. 034004, 2016.

[48] F. G. Balzer, "Entwicklung und untersuchungen zur 3-d-nanopositioniertechnik in großen bewegungsbereichen," 2015.

[49] A. J. Fleming and K. K. Leang, "Integrated strain and force feedback for high-performance control of piezoelectric actuators," *Sensors and Actuators A: Physical*, vol. 161, no. 1-2, pp. 256–265, 2010.

[50] A. J. Fleming, "A review of nanometer resolution position sensors: Operation and performance," *Sensors and Actuators A: Physical*, vol. 190, pp. 106–126, 2013.

[51] A. A. Barlian, W.-T. Park, J. R. Mallon, A. J. Rastegar, and B. L. Pruitt, "Semiconductor piezoresistance for microsystems," *Proceedings of the IEEE*, vol. 97, no. 3, pp. 513–552, 2009.

[52] R. K. Messenger, Q. T. Aten, T. W. McLain, and L. L. Howell, "Piezoresistive feedback control of a mems thermal actuator," *Journal of Microelectromechanical Systems*, vol. 18, no. 6, pp. 1267–1278, 2009.

[53] Y. K. Yong, B. Ahmed, and S. R. Moheimani, "Atomic force microscopy with a 12-electrode piezoelectric tube scanner," *Review of Scientific Instruments*, vol. 81, no. 3, p. 033701, 2010.

[54] A. J. Fleming, "Nanopositioning system with force feedback for high-performance tracking and vibration control," *IEEE/Asme Transactions on Mechatronics*, vol. 15, no. 3, pp. 433–447, 2010.

[55] M. Kim, W. Moon, E. Yoon, and K.-R. Lee, "A new capacitive displacement sensor with high accuracy and long-range," *Sensors and Actuators A: Physical*, vol. 130, pp. 135–141, 2006.

[56] D. S. Nyce, "Linear position sensors," *Theory and application. Hoboken (NJ): John Wiley and Sons*, 2004.

[57] G. Clayton, S. Tien, A. Fleming, S. Moheimani, and S. Devasia, "Inverse-feedforward of charge-controlled piezopositioners," *Mechatronics*, vol. 18, no. 5-6, pp. 273–281, 2008.

[58] A. Yacoot and N. Cross, "Measurement of picometre non-linearity in an optical grating encoder using x-ray interferometry," *Measurement Science and Technology*, vol. 14, no. 1, p. 148, 2002.

[59] J.-Y. Lee, H.-Y. Chen, C.-C. Hsu, and C.-C. Wu, "Optical heterodyne grating interferometry for displacement measurement with subnanometric resolution," *Sensors and Actuators A: physical*, vol. 137, no. 1, pp. 185–191, 2007.

[60] "Lip 382," https://www.heidenhain.fr/fr_FR/produits/systemes-de-mesure-lineaire/systemes-de-mesure-lineaire-a-regle-nue/selection-guide-for-lip/lip-382/, accessed: 2018-10-31.

[61] A. Khiat, F. Lamarque, C. Prelle, P. Pouille, M. Leester-Schädel, and S. Büttgenbach, "Two-dimension fiber optic sensor for high-resolution and long-range linear measurements," *Sensors and Actuators A: Physical*, vol. 158, no. 1, pp. 43–50, 2010.

[62] W. OâBrien, "Long-range motion with nanometer precision," *Photonics Spectra*, vol. 39, no. 6, pp. 80–81, 2005.

[63] Y. Egashira, K. Kosaka, T. Iwabuchi, T. Kosaka, T. Baba, T. Endo, H. Hashiguchi, T. Harada, K. Nagamoto, M. Watanabe *et al.*, "Sub-nanometer resolution ultrasonic motor for 300 mm wafer lithography precision stage," *Japanese journal of applied physics*, vol. 41, no. 9R, p. 5858, 2002.

[64] R. Merry, M. Uyanik, R. van de Molengraft, R. Koops, M. van Veghel, and M. Steinbuch, "Identification, control and hysteresis compensation of a 3 dof metrological afm," *Asian Journal of Control*, vol. 11, no. 2, pp. 130–143, 2009.

[65] L. Chassagne, S. Blaize, P. Ruaux, S. Topcu, P. Royer, Y. Alayli, and G. Lérondel, "Note: Multiscale scanning probe microscopy," *Review of scientific instruments*, vol. 81, no. 8, p. 086101, 2010.

[66] S. Ducourtieux and B. Poyet, "Development of a metrological atomic force microscope with minimized abbe error and differential interferometer-based real-time position control," *Measurement Science and Technology*, vol. 22, no. 9, p. 094010, 2011.

[67] G. Zhang, "A study on the abbe principle and abbe error," *CIRP Annals-Manufacturing Technology*, vol. 38, no. 1, pp. 525–528, 1989.

[68] N. Bobroff, "Recent advances in displacement measuring interferometry," *Measurement Science and Technology*, vol. 4, no. 9, p. 907, 1993.

[69] J. C. Wyant and K. Creath, "Basic wavefront aberration theory for optical metrology," *Applied optics and optical engineering*, vol. 11, no. s 29, p. 2, 1992.

[70] J. A. Stone Jr and J. H. Zimmerman, "Index of refraction of air," *Index of Refraction of Air*, 2001.

[71] N. Festin, C. Plesse, C. Chevrot, D. Teyssié, L. Josselin, P. Pirim, and F. Vidal, "Actuation and sensing properties of electroactive polymer whiskers," *Procedia Computer Science*, vol. 7, pp. S4–S7, 2011.

[72] N. Festin, "Elaboration dâactionneurs et capteurs polymères et intégration dans des systèmes de perceptions biomimétiques," Ph.D. dissertation, Université de Cergy Pontoise, 2012.

[73] R. Baughman, L. Shacklette, R. Elsenbaumer, E. Plichta, and C. Becht, "Micro electromechanical actuators based on conducting polymers," in *Molecular Electronics*. Springer, 1991, pp. 267–289.

[74] I. W. Hunter and S. Lafontaine, "A comparison of muscle with artificial actuators," in *Solid-State Sensor and Actuator Workshop, 1992. 5th Technical Digest., IEEE*. IEEE, 1992, pp. 178–185.

[75] W. Takashima, T. Uesugi, M. Fukui, M. Kaneko, and K. Kaneto, "Mechanochemoelectrical effect of polyaniline film," *Synthetic metals*, vol. 85, no. 1-3, pp. 1395–1396, 1997.

[76] T. Mirfakhrai, J. D. Madden, and R. H. Baughman, "Polymer artificial muscles," *Materials today*, vol. 10, no. 4, pp. 30–38, 2007.

[77] R. Baughman, "Conducting polymer artificial muscles," *Synthetic metals*, vol. 78, no. 3, pp. 339–353, 1996.

[78] V. Woehling, "Nouveaux développements de matériaux électroactifs à base de polymères conducteurs électroniques: Vers une intégration dans des systèmes biomédicaux," Ph.D. dissertation, Université de Cergy Pontoise, 2016.

[79] K. Kaneto, M. Kaneko, Y. Min, and A. G. MacDiarmid, "âartificial muscleâ: Electromechanical actuators using polyaniline films," *Synthetic Metals*, vol. 71, no. 1-3, pp. 2211–2212, 1995.

[80] J. Sansinena, V. Olazabal, T. Otero, C. P. Da Fonseca, and M.-A. De Paoli, "A solid state artificial muscle based on polypyrrole and a solid polymeric electrolyte working in air," *Chemical Communications*, no. 22, pp. 2217–2218, 1997.

[81] T. Shoa, J. D. Madden, T. Mirfakhrai, G. Alici, G. M. Spinks, and G. G. Wallace, "Electromechanical coupling in polypyrrole sensors and actuators," *Sensors and Actuators A: Physical*, vol. 161, no. 1-2, pp. 127–133, 2010.

[82] N. Festin, A. Maziz, C. Plesse, D. Teyssié, C. Chevrot, and F. Vidal, "Robust solid polymer electrolyte for conducting ipn actuators," *Smart Materials and Structures*, vol. 22, no. 10, p. 104005, 2013.

[83] T. Sugino, K. Kiyohara, I. Takeuchi, K. Mukai, and K. Asaka, "Actuator properties of the complexes composed by carbon nanotube and ionic liquid: The effects of additives," *Sensors and Actuators B: Chemical*, vol. 141, no. 1, pp. 179–186, 2009.

[84] T. A. Nguyen, C.-J. Peng, K. Rohtlaid, C. Plesse, T.-M. G. Nguyen, F. Vidal, S.-J. Chen, L. Chassagne, and B. Cagneau, "Conducting interpenetrating polymer network to sense and actuate: Measurements and modeling," *Sensors and Actuators A: Physical*, vol. 272, pp. 325–333, 2018.

[85] T. Shoa, D. S. Yoo, E. Fok, and J. Madden, "Analytical impedance model for electrochemically driven conducting polymer devices," *ECS Transactions*, vol. 28, no. 18, pp. 49–58, 2010.

[86] M. Farajollahi, F. Sassani, N. Naserifar, A. Fannir, C. Plesse, G. T. Nguyen, F. Vidal, and J. D. Madden, "Characterization and dynamic charge dependent modeling of conducting polymer trilayer bending," *Smart Materials and Structures*, vol. 25, no. 11, p. 115044, 2016.

[87] M. Farajollahi, A. Usgaocar, Y. Dobashi, V. Woehling, C. Plesse, F. Vidal, F. Sassani, and J. D. Madden, "Nonlinear two-dimensional transmission line models for electrochemically driven conducting polymer actuators," *IEEE/ASME Transactions on Mechatronics*, vol. 22, no. 2, pp. 705–716, 2017.

[88] G. Alici, G. M. Spinks, J. D. Madden, Y. Wu, and G. G. Wallace, "Response characterization of electroactive polymers as mechanical sensors," *IEEE/ASME Transactions on Mechatronics*, vol. 13, no. 2, pp. 187–196, 2008.

[89] S. Roy, "On the realization of a constant-argument immittance or fractional operator," *IEEE Transactions on Circuit Theory*, vol. 14, no. 3, pp. 264–274, 1967.

[90] T. Shoa, T. Mirfakhrai, and J. D. Madden, "Electro-stiffening in polypyrrole films: Dependence of young's modulus on oxidation state, load and frequency," *Synthetic Metals*, vol. 160, no. 11-12, pp. 1280–1286, 2010.

[91] A. Maziz, C. Plesse, C. Soyer, C. Chevrot, D. Teyssié, E. Cattan, and F. Vidal, "Demonstrating khz frequency actuation for conducting polymer microactuators," *Advanced Functional Materials*, vol. 24, no. 30, pp. 4851–4859, 2014.

[92] A. Fannir, "Actionneur à base de polymères conducteurs présentant une déformation linéaire à lâair et compatible avec un environnement spatial," Ph.D. dissertation, Université de Cergy Pontoise, 2017.

[93] M. Farajollahi, S. E. Takallo, V. Woehling, A. Fannir, C. Plesse, F. Vidal, F. Sassani, and J. D. Madden, "Stacking trilayers to increase force generation," in *Electroactive Polymer Actuators and Devices (EAPAD) 2015*, vol. 9430. International Society for Optics and Photonics, 2015, p. 94301A.

[94] S. John, G. Alici, G. M. Spinks, J. D. Madden, and G. Wallace, "Towards fully optimized conducting polymer bending sensors: the effect of geometry," *Smart Materials and Structures*, vol. 18, no. 8, p. 085007, 2009.

[95] D. Ponceau, P. Millier, and S. Olivier, "Subnanometric michelson interferometry for seismological applications," in *Photonics Europe*. International Society for Optics and Photonics, 2008, pp. 70 030U–70 030U.

[96] A. Missoffe, S. Olivier, B. Cagneau, P. Millier, H. Guan, and L. Chassagne, "Integrated waveguide interferometer with picometric performances," in *Advanced Intelligent Mechatronics (AIM), 2014 IEEE/ASME International Conference on*. IEEE, 2014, pp. 1134–1138.

[97] W. Merzouk, B. Cagneau, F. Gardillou, K. Hilouane, and L. Chassagne, "Highly compact and easy-to-use optical chip interferometer with picometric performances," *Review of Scientific Instruments*, vol. 87, no. 10, p. 103103, 2016.

[98] S. Olivier, D. Ponceau, P. Millier, and N. Brebion, "Bulk optics for seismological applications," in *SPIE Optical Engineering+ Applications*. International Society for Optics and Photonics, 2009, pp. 74 240P–74 240P.

[99] F. Malbet, P. Kern, I. Schanen-Duport, J.-P. Berger, K. Rousselet-Perraut, and P. Benech, "Integrated optics for astronomical interferometry-i. concept and astronomical applications," *Astronomy and Astrophysics Supplement series*, vol. 138, no. 1, pp. 135–145, 1999.

[100] J. Mariotti *et al.*, "Coherent combined instrumentation for the vlt interferometer," *ESO VLT report*, no. 65, 1992.

[101] M. Born and E. Wolf, *Principles of optics: electromagnetic theory of propagation, interference and diffraction of light*. Elsevier, 1980.

[102] M. A. Zumberge, J. Berger, M. A. Dzieciuch, and R. L. Parker, "Resolving quadrature fringes in real time," *Applied optics*, vol. 43, no. 4, pp. 771–775, 2004.

[103] D. W. Allan, H. Hellwig, and D. J. Glaze, "An accuracy algorithm for an atomic time scale," *Metrologia*, vol. 11, no. 3, p. 133, 1975.

[104] Y. Zhu, A. Bazaei, S. R. Moheimani, and M. R. Yuce, "Design, modeling, and control of a micromachined nanopositioner with integrated electrothermal actuation and sensing," *Journal of Microelectromechanical Systems*, vol. 20, no. 3, pp. 711–719, 2011.

[105] A. J. Fleming and B. S. Routley, "A closed-loop phase-locked interferometer for wide bandwidth position sensing," *Review of Scientific Instruments*, vol. 86, no. 11, p. 115001, 2015.

[106] K. Karrai and P. Braun, "Miniature long-range laser displacement sensor," *Proc. Actuator, Bremen, Germany*, pp. 285–288, 2010.

[107] D. Rugar, H. Mamin, R. Erlandsson, J. Stern, and B. Terris, "Force microscope using a fiber-optic displacement sensor," *Review of Scientific Instruments*, vol. 59, no. 11, pp. 2337–2340, 1988.

[108] B. Hoogenboom, P. Frederix, J. Yang, S. Martin, Y. Pellmont, M. Steinacher, S. Zäch, E. Langenbach, H.-J. Heimbeck, A. Engel *et al.*, "A fabry–perot interferometer for micrometer-sized cantilevers," *Applied Physics Letters*, vol. 86, no. 7, p. 074101, 2005.

[109] H. I. Rasool, P. R. Wilkinson, A. Z. Stieg, and J. K. Gimzewski, "A low noise all-fiber interferometer for high resolution frequency modulated atomic force microscopy imaging in liquids," *Review of Scientific Instruments*, vol. 81, no. 2, p. 023703, 2010.

[110] L. Bellon, S. Ciliberto, H. Boubaker, and L. Guyon, "Differential interferometry with a complex contrast," *Optics Communications*, vol. 207, no. 1, pp. 49–56, 2002.

[111] Y. Martin, C. C. Williams, and H. K. Wickramasinghe, "Atomic force microscope–force mapping and profiling on a sub 100-å scale," *Journal of Applied Physics*, vol. 61, no. 10, pp. 4723–4729, 1987.

[112] A. Den Boef, "Scanning force microscopy using a simple low-noise interferometer," *Applied physics letters*, vol. 55, no. 5, pp. 439–441, 1989.

[113] R. De La Rue, R. Humphryes, I. Mason, and E. Ash, "Acoustic-surface-wave amplitude and phase measurements using laser probes," in *Proceedings of the Institution of Electrical Engineers*, vol. 119, no. 2. IET, 1972, pp. 117–126.

[114] P. Paolino, F. A. Aguilar Sandoval, and L. Bellon, "Quadrature phase interferometer for high resolution force spectroscopy," *Review of Scientific Instruments*, vol. 84, no. 9, p. 095001, 2013.

[115] D. Rugar, H. Mamin, and P. Guethner, "Improved fiber-optic interferometer for atomic force microscopy," *Applied Physics Letters*, vol. 55, no. 25, pp. 2588–2590, 1989.

[116] C. Schönenberger and S. Alvarado, "A differential interferometer for force microscopy," *Review of Scientific Instruments*, vol. 60, no. 10, pp. 3131–3134, 1989.

[117] P. Mulhern, T. Hubbard, C. Arnold, B. Blackford, and M. Jericho, "A scanning force microscope with a fiber-optic-interferometer displacement sensor," *Review of scientific instruments*, vol. 62, no. 5, pp. 1280–1284, 1991.

[118] G. Meyer and N. M. Amer, "Novel optical approach to atomic force microscopy," *Applied physics letters*, vol. 53, no. 12, pp. 1045–1047, 1988.

[119] C. A. Putman, B. G. De Grooth, N. F. Van Hulst, and J. Greve, "A detailed analysis of the optical beam deflection technique for use in atomic force microscopy," *Journal of Applied Physics*, vol. 72, no. 1, pp. 6–12, 1992.

[120] M. Gustafsson and J. Clarke, "Scanning force microscope springs optimized for optical-beam deflection and with tips made by controlled fracture," *Journal of applied physics*, vol. 76, no. 1, pp. 172–181, 1994.

[121] T. Fukuma, M. Kimura, K. Kobayashi, K. Matsushige, and H. Yamada, "Development of low noise cantilever deflection sensor for multienvironment frequency-modulation atomic force microscopy," *Review of Scientific Instruments*, vol. 76, no. 5, p. 053704, 2005.

[122] T. Fukuma and S. P. Jarvis, "Development of liquid-environment frequency modulation atomic force microscope with low noise deflection sensor for cantilevers of various dimensions," *Review of Scientific Instruments*, vol. 77, no. 4, p. 043701, 2006.

[123] T. Fukuma, "Wideband low-noise optical beam deflection sensor with photothermal excitation for liquid-environment atomic force microscopy," *Review of Scientific Instruments*, vol. 80, no. 2, p. 023707, 2009.

[124] R. Enning, D. Ziegler, A. Nievergelt, R. Friedlos, K. Venkataramani, and A. Stemmer, "A high frequency sensor for optical beam deflection atomic force microscopy," *Review of Scientific Instruments*, vol. 82, no. 4, p. 043705, 2011.

[125] G. Shan, Y. Li, L. Zhang, Z. Wang, Y. Zhang, and J. Qian, "Contributed review: Application of voice coil motors in high-precision positioning stages with large travel ranges," *Review of Scientific Instruments*, vol. 86, no. 10, p. 101501, 2015.

[126] K. Birch, "Optical fringe subdivision with nanometric accuracy," *Precision Engineering*, vol. 12, no. 4, pp. 195–198, 1990.

[127] O. Cip and F. Petru, "A scale-linearization method for precise laser interferometry," *Measurement Science and Technology*, vol. 11, no. 2, p. 133, 2000.

[128] T. Požar and J. Možina, "Enhanced ellipse fitting in a two-detector homodyne quadrature laser interferometer," *Measurement Science and Technology*, vol. 22, no. 8, p. 085301, 2011.

[129] M. Harker, P. OâLeary, and P. Zsombor-Murray, "Direct type-specific conic fitting and eigenvalue bias correction," *Image and Vision Computing*, vol. 26, no. 3, pp. 372–381, 2008.

[130] A. Fitzgibbon, M. Pilu, and R. B. Fisher, "Direct least square fitting of ellipses," *IEEE Transactions on pattern analysis and machine intelligence*, vol. 21, no. 5, pp. 476–480, 1999.

[131] P. Gregorčič, T. Požar, and J. Možina, "Quadrature phase-shift error analysis using a homodyne laser interferometer," *Optics express*, vol. 17, no. 18, pp. 16 322–16 331, 2009.

[132] M. Wakim, "Contrôle de la position et de la vitesse d'une masse à l'échelle nanométrique: application à la balance du watt du lne," Ph.D. dissertation, Université de Versailles-Saint Quentin en Yvelines, 2008.

[133] "Tables linèaires de nanopositionnement sèrie nlsx," http://www.isp-system.fr/wp-content/uploads/2012/01/NLSx_Table-lin%C3%A9aire-nanopositionnement_ISP-SYSTEM.pdf, accessed: 2018-10-31.

[134] "Index of refraction of air," https://emtoolbox.nist.gov/Wavelength/Ciddor.asp, accessed: 2018-10-31.

[135] "Rio orion laser module," http://www.rio-lasers.com/pdf/Rio_Orion_Product_Brief_Update_1.24.14.pdf, accessed: 2018-10-31.

[136] C. Gonzalez and R. Lumia, "An ipmc microgripper with integrated actuator and sensing for constant finger-tip displacement," *Smart Materials and Structures*, vol. 24, no. 5, p. 055011, 2015.

[137] M. Shahinpoor and K. J. Kim, "Ionic polymer–metal composites: Iii. modeling and simulation as biomimetic sensors, actuators, transducers, and artificial muscles," *Smart materials and structures*, vol. 13, no. 6, p. 1362, 2004.

[138] S. Ford, G. Macias, and R. Lumia, "Single active finger ipmc microgripper," *Smart Materials and Structures*, vol. 24, no. 2, p. 025015, 2014.

[139] R. Jain, S. Datta, S. Majumder, and A. Dutta, "Two ipmc fingers based micro gripper for handling," *International Journal of Advanced Robotic Systems*, vol. 8, no. 1, p. 13, 2011.

[140] A. Somà, S. Iamoni, R. Voicu, and R. Muller, "Design and building-up of an electro-thermally actuated cell microgripper," *Proc. Recent Advances in Mechanical Engineering and Mechanics*, pp. 125–130, 2014.

[141] B. Solano and D. Wood, "Design and testing of a polymeric microgripper for cell manipulation," *Microelectronic Engineering*, vol. 84, no. 5-8, pp. 1219–1222, 2007.

[142] N. Festin, C. Plesse, C. Chevrot, D. Teyssié, P. Pirim, and F. Vidal, "Conducting ipn actuators for biomimetic vision system," in *Electroactive Polymer Actuators and Devices (EAPAD) 2011*, vol. 7976. International Society for Optics and Photonics, 2011, p. 79760K.

[143] A. Fannir, C. Plesse, G. T. Nguyen, E. Laurent, L. Cadiergues, and F. Vidal, "Behavior of ionic conducting ipn actuators in simulated space conditions," in *Electroactive Polymer Actuators and Devices (EAPAD) 2016*, vol. 9798. International Society for Optics and Photonics, 2016, p. 979826.

[144] M. Farajollahi, V. Woehling, C. Plesse, G. T. Nguyen, F. Vidal, F. Sassani, V. X. Yang, and J. D. Madden, "Self-contained tubular bending actuator driven by conducting polymers," *Sensors and Actuators A: Physical*, vol. 249, pp. 45–56, 2016.

[145] K. K. Lee, N. R. Munce, T. Shoa, L. G. Charron, G. A. Wright, J. D. Madden, and V. X. Yang, "Fabrication and characterization of laser-micromachined polypyrrole-based artificial muscle actuated catheters," *Sensors and Actuators A: Physical*, vol. 153, no. 2, pp. 230–236, 2009.

[146] T. Shoa, J. D. Madden, N. R. Munce, and V. Yang, "Analytical modeling of a conducting polymer-driven catheter," *Polymer International*, vol. 59, no. 3, pp. 343–351, 2010.

[147] J. M. Gere and S. P. Timoshenko, "Mechanics of materials," 1984.

[148] E. Volterra and E. Zachmanoglou, "Dynamics of vibrations (columbus, oh: Charles e. merrill books, inc.)," 1965.

[149] M. P. W. Atkins and M. J. De Paula, *Chimie physique*. De Boeck Supérieur, 2013.

[150] A. Oustaloup, "La commande crone, commande robuste dâordre non entier." *Herms (Trait des Nouvelles Technologies-Srie Automatique), Paris, ISBN 2-86601-289-5*, 1991.

[151] M. Pellet, "Caractérisation non entière de systèmes biologiques: application au muscle squelettique et au poumon," Ph.D. dissertation, Université Sciences et Technologies-Bordeaux I, 2013.

[152] S. Dugowson, "Les différentielles métaphysiques: histoire et philosophie de la généralisation de l'ordre de la dérivation," Ph.D. dissertation, Paris 13, 1994.

université PARIS-SACLAY | ÉCOLE DOCTORALE Sciences et technologies de l'information et de la communication (STIC)

Titre : Étude d'un interféromètre intégré : application à la caractérisation de transducteurs innovants.

Mots clés : métrologie, interférométrie, polymères électroactifs.

Résumé : Ce travail de thèse porte sur l'étude d'un interféromètre compact et intégré et son utilisation pour la caractérisation d'un transducteur en polymère électro-actif capable de fonctionner en capteur et en actionneur. Dans ce document, les caractéristiques de fonctionnement et performances de l'interféromètre sont détaillées. De même, la fonction capteur du polymère électroactif est caractérisée, et ses capacités micrométriques sont démontrées.

L'interféromètre PicoMove est le résultat de l'étroite collaboration entre le LISV et son partenaire industriel TeemPhotonics. Cet interféromètre, qui fonctionne dans le domaine de l'infrarouge moyen (1,55 μm), est fondé sur la technologie des guides d'ondes optiques. Cette particularité lui confère une plus grande robustesse vis-à-vis de l'environnement extérieur. Son architecture repose sur une structure de type Michelson-Young modifiée. Des expériences ont été mises en œuvre pour caractériser ses performances. Il a été démontré qu'une résolution sub-nanométrique et un très faible niveau de bruit sont atteints. Une densité spectrale de puissance $100\, fm/\sqrt{Hz}$ est possible en conditions statiques. En outre, sa robustesse aux conditions environnementales est démontrée et les sources d'erreurs et spécificités métrologiques sont discutées.

Le second point de cette thèse a trait aux polymères électro-actifs. L'interféromètre a permis de caractériser le transducteur configuré pour des déplacements micrométriques, et également d'obtenir un modèle électro-mécanique pour le fonctionnement en mode capteur. Les performances sont détaillées et discutées.

Title: Study of an integrated interferometer: application to the characterization of innovative transducers.

Keywords: metrology, interferometry, electroactive polymers.

Abstract: This work concerns the study of a compact and integrated interferometer and its use for the characterization of an electro-active polymer based transducer that operates as sensor and actuator. In this document, we detail the operating characteristics and performances of the interferometer. Similarly, the sensor function of the electroactive polymer is fully characterized, and its micrometric capabilities are demonstrated.

The PicoMove interferometer results in the joint work of the LISV and its industrial partner TeemPhotonics. This interferometer operates in the mid-range infrared (1.55 µm). It is based on an optical guide technology that provides a high degree of robustness with respect to the external environment. Its architecture is based on a modified Michelson-Young structure. Experiments have been conducted to characterize its performances. It has been shown that a nanometric resolution and a very low noise level are reached. A spectral power density of $100\, fm/\sqrt{Hz}$ is possible under static conditions. In addition, its robustness with respect to the environmental conditions is demonstrated. Moreover, the metrological specificities are detailed concerning specific error sources.

The second point of this PhD concerns electroactive polymers. The interferometer allows the characterization of the transducer configured for micrometric displacements, and obtains an electromechanical model for operation in sensor mode. The performances are detailed and discussed.

Université Paris-Saclay
Espace Technologique / Immeuble Discovery
Route de l'Orme aux Merisiers RD 128 / 91190 Saint-Aubin, France